Microfluidic Devices for Analysis of Red Blood Cell Mechanical Properties

by Hansen Chang Bow

B.S. Electrical Engineering and Computer Sciences, 2004
University of California, Berkeley

M.S. Electrical Engineering and Computer Science, 2006
Massachusetts Institute of Technology

Submitted to the Department of Electrical Engineering and Computer Science in partial fulfillment of the requirements for the degree of Doctor of Philosophy in Electrical Engineering and Computer Science at the MASSACHUSETTS INSTITUTE OF TECHNOLOGY

June 2010

Signature of Author: _____
Department of Electrical Engineering and Computer Science
May 21, 2010

Certified by: _____
Jongyoon Han
Associate Professor of Electrical Engineering and Computer Science
Associate Professor of Biological Engineering
Thesis Supervisor

Accepted by: _____
Terry P. Orlando
Professor of Electrical Engineering and Computer Science
Chairman, Department Committee on Graduate Students

Microfluidic Devices for Analysis of Red Blood Cell Mechanical Properties

by Hansen Chang Bow

Submitted to the Department of Electrical Engineering and Computer Science

on May 21, 2010, in Partial Fulfillment of the

Requirements for the Degree of Doctor of Philosophy

in Electrical Engineering and Computer Science

Abstract

Decreased deformability of human red blood cells (RBCs) is both a cause of disease and biomarker for disease (1). To traverse blood capillaries, the biconcave disk-shaped RBC must deform dramatically, since the diameter of the unconstrained RBC is larger than that of the capillaries. If the RBC becomes immobilized in a capillary, hypoxia and tissue injury may result, potentially leading to death. Changes in RBC deformability may be attributable to genetics (e.g. sickle cell anemia (2) and spherocytosis (3)), drug exposure (e.g. pentoxifylline (4)), and disease (e.g. diabetes (5) and malaria (6)).

Within the past 15 years, microfabrication techniques have enabled the creation of pores comparable in size and shape to the smallest human capillaries (7) and slits in the spleen (8). We use this microfabrication ability to create devices that analyze and separate RBCs of different deformability.

The first device we create is an automated 'deformability cytometer' that measures dynamic mechanical responses of 10^3~10^4 individual cells in a cell population. Fluorescence measurements of each cell are simultaneously acquired, resulting in a population-based correlation between biochemical properties (e.g. cell surface markers) and dynamic mechanical deformability. This device is especially applicable to heterogeneous cell populations, and we demonstrate its ability to mechanically characterize a small number of ring-stage malaria-infected RBCs in a large population of healthy RBCs.

Next we present a device whose design is based on the architecture of the human spleen. This device is able to continuously separate more deformable from less deformable RBCs. We demonstrate the ability of this device to separate schizont-stage malaria-infected RBCs from healthy RBCs. Together, these devices enable the analysis and separation of single-RBCs based on deformability.

Thesis Supervisor: Jongyoon Han
Title: Associate Professor of Electrical Engineering and Computer Science and Biological Engineering

Acknowledgments

Professor Jongyoon Han has been my research advisor since shortly after my arrival at MIT. He is a person that I greatly admire and respect, and it was an honor to work with him these past few years. I sincerely appreciate his enthusiasm and confidence in my research ideas and his willingness to let me explore what interested me. I could not have wished for a better advisor.

In addition to Professor Han's strengths as a scientist is his ability to attract and develop excellent people. From current and former members of the lab, I have learned how to organize my ideas and carry out a research project. I greatly appreciate the help that Drs. Jianping Fu, Pan Mao, Sung-Jae Kim, Patrick Abgrall, and graduate student Huang Sha provided me with on my research. The other members of the group were also wonderful people to work with and be around and include Lih-Feng Cheow, Leon Li, Ying-Chih Wang, Aniruddh Sarkar, Masumi Yamada, and Yong-Ak Song.

I thank Professor Subra Suresh for the interest he took in my project. I greatly valued talking with him about possible research avenues to explore and creating plans to accomplish them. From his research group, Drs. Monica Diez-Silva, Igor Pivkin, Ming Dao, and graduate student David Quinn were a pleasure to work with.

Professor Jacquin Niles provided me with substantial help on the topic of malaria. His knowledge and his ability to refine research ideas are qualities that I admire. His graduate student Steve Goldfless taught me a lot about malaria provided me with excellent cell samples.

At the National University of Singapore, Professor Chwee Teck Lim and his graduate student Hanwei Hou played a large role in the continuous-flow deformability-based separation project. I appreciate their hospitality during my time in Singapore.

Alan Benson helped me substantially in statistical analysis. In addition to being an excellent economist, he is also a great friend.

I thank Professors Sangeeta Bhatia and Roger Kamm for serving on my thesis committee. Their knowledge and insight were immensely helpful.

The Health Sciences and Technology (HST) Graduate Education in Medical Sciences (GEMS) program provided me with the background in human pathophysiology needed for this project. Through this program, I met Dr. Robert Sackstein, who served as an excellent mentor and preceptor.

The Peake Prize Research Assistantship, Course 6 Teaching Assistant Appointments, Singapore-MIT Alliance II Computational Engineering (CE) programme (FRP-1), and Singapore-MIT Alliance for Research and Technology (SMART) provided necessary financial support for my thesis work.

Lastly, I thank my family, relatives, and friends whose encouragement and support were essential in my time as a graduate student at MIT.

Contents

Chapter 1

Motivation and Scope: Blood Diseases

Change in cell stiffness is a characteristic of several hematological diseases. Examples of such diseases may involve red blood cells (e.g. malaria (9) and sickle cell anemia (10)), white blood cells (WBCs) (e.g. leukemia (11) and leukostasis (12)), and metastatic solid-organ tumor cells (e.g. circulating tumor cells (13) and the more extreme carcinocythemia). Often, increases in blood cell stiffness lead to loss of the cells' ability to squeeze through capillaries, resulting in clogging, blood clotting due to stasis, hypoxia, organ failure, coma, and ultimately death (14, 15). Capillaries typically have diameters around 2-3 μm, and the resting shapes of cells in blood must deform substantially to enter. Additionally, more rigid cells may be sequestered in the splenic cords, resulting in splenomegaly and predisposing the spleen to rupture (14).

In normal individuals, the spleen is the organ that filters out these less deformable cells through micron-sized slits in the sinusoidal basement membrane. This architecture of the basement membrane has been compared to "tall wooden barrels with both ends open, with the endothelial cells represented by the wooden staves" (16). Blood cells must pass through these slits before they can travel to the splenetic vein and reenter the circulation. Less deformable cells may not be able to squeeze through these slits, and macrophages then engulf and remove these trapped cells. It has been hypothesized that some diseases involving less deformable cells circulating in the blood may be caused by the absence or defective function of the spleen (17, 18).

Study of blood cells' mechanical properties would then be highly meaningful, both in terms of deciphering the biological mechanisms of these various diseases, as well as developing effective diagnostic or clinical strategies toward addressing these diseases. These observations provide strong motivation for developing tools to study and manipulate cells based on their mechanical properties. In this chapter, we provide examples of hematological diseases in which cell deformability can serve as an important biomarker.

Composition of Blood

Blood is composed of a variety of cells suspended in fluid, called plasma. In men, the proportion of blood consisting of cells ranges from 39-49%, while for women it ranges from 33-43% (19). There are three major groups of cells in blood: RBCs, WBCs, and platelets. Although RBCs and platelets are classified as cells, they lack a nucleus. All of these cells are essentially formed in the bone marrow. For every 1000 RBCs, there are approximately 100 platelets and 1 WBC. In 1 mL of blood, there are approximately 6×10^9 RBCs.

RBCs contain large amounts of hemoglobin and are primarily involved in the transport of oxygen and carbon dioxide. WBCs protect the body from foreign substances and exist both in the circulation and in the tissues. Although RBCs and platelets are homogeneous in terms of size, composition, and function, many types of WBCs exist. The two most common types of WBCs in the circulation are the neutrophil and the eosinophil. The neutrophiil can be identified by its 5-lobed nucleus, and its primary function is acute inflammatory response to tissue injury. The eosinophil can be identified by its 2-lobed nucleus, and its primary function is combating infection and mounting a response to allergy. Platelets control bleeding by obstructing leakages in blood vessel walls and activating the coagulation cascade.

Diseases of Non-Blood Cells in Blood

Occasionally cells other than RBCs, WBCs, and platelets are found in blood. For example, the proliferation of solid organ cancer cells, such as breast, skin, and intestinal cancer cells, can result in these cells shed into blood. These cells, which are commonly epithelial in origin, have frequencies in blood of on the order of 10 cells/ml of blood or 1 cell in approximately 10^9 blood cells. Increased numbers of these cells in blood correlates with decreased probability of cancer survival (20, 21). Therefore, quantifying these rare, circulating tumor cells (CTCs) has been proposed as an effective diagnostic / prognostic strategy recently. Methods to detect these cells have relied on FACS (22), magnetic cell sorting (MACS) and then FACS (23), and antibody-coated microfluidic channels (24). However all of these methods require expensive reagents and equipment, skilled technical personnel, and long analysis times. The main challenge of detecting CTCs from blood is in the extreme rarity of these cells, compared with other blood cells.

When large numbers of non-blood cancer cells are shed into the blood, the result is termed carcinocythemia (25). Carcinocythemia is extremely rare (18) and signals imminent death, often within

weeks (17, 26). It is hypothesized that carcinocythemia is associated with spleen dysfunction, under the assumption that the splenetic macrophages should filter cancer cells out of the blood (18) in part due to their larger size and lower deformability compared with other blood cells.

Diseases of White Blood Cells

Leukemia is a cancer of bone marrow cells, which produce the cells that are normally found in blood. One of the results of this cancer is abnormal numbers of cells that are normally found in blood (hematocrit that is too high or an elevated proportion of WBCs to RBCs). Additionally, these cells in the blood may be immature and unable to function. When leukemia cells accumulate in the blood vessels of vital organs during acute leukemia, respiratory failure and intracranial hemorrhage may result. This condition is termed leukostasis. A side-effect of chemotherapy treatment may also be leukostasis. Lam *et al.* found that the leukemia cells stiffened up to two orders of magnitude during chemotherapy-induced cell death (12).

Diseases of Red Blood Cells

Approximately 99.9% of the cells in blood are RBCs. RBCs assume a biconcave-disk shape at rest, and have dimensions of approximately 7.8 μm ± 0.6 μm wide and 2.6 μm ± 0.3 μm thick (27), Figure 1.1. During terminal differentiation, it loses its nucleus and its ability to synthesize new proteins. These cells are able to deform into capillaries that are 2-3 μm in diameter. RBC deformability can be decomposed into three components: internal viscosity, surface area-to-volume ratio, and viscoelastic properties of the membrane (28). The surface area-to-volume ratio is important for RBCs in particular, as the RBC membrane cannot stretch very much before it breaks (27).

The lifetime of the red blood cell is around 120 days. It is believed that at the end of its lifetime, the RBC becomes stiffer, among other changes, and is taken out of the circulation by macrophages in the spleen. These other changes include decreased cell volume, cell size, and deformability, as well as increased osmotic fragility (29).

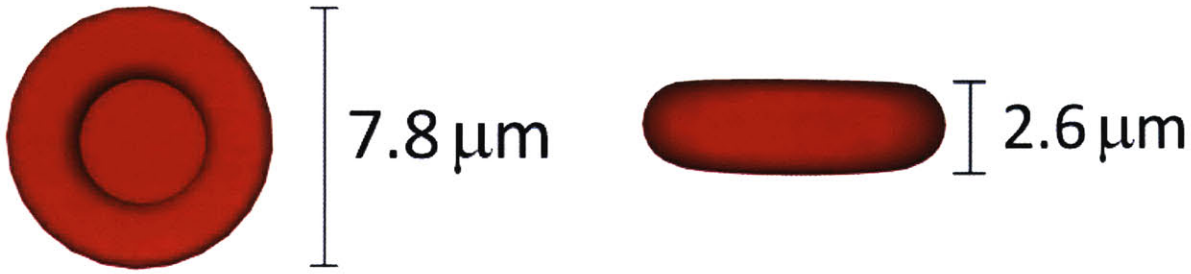

Figure 1.1. Red blood cell dimensions. At rest, RBCs assume a biconcave-disk shape and have dimensions of approximately 7.8 μm ± 0.6 μm wide and 2.6 μm ± 0.3 μm thick (27).

Sickle Cell Anemia

Several diseases of RBCs involve changes in their mechanical properties. Perhaps the most well-known of these diseases is sickle cell anemia. In sickle cell anemia, a point mutation at the β-globin chain of hemoglobin results in the hemoglobin molecules aggregating and polymerizing when deoxygenated. The RBC cytosol converts from a freely flowing liquid to a viscous gel when this polymerization occurs. When deoxygenation continues, the defective hemoglobin molecules form long fibers, resulting in a sickle-shaped RBC, Figure 1.2. In this disease, the primary cause of the RBCs' increased rigidity is increased viscosity of the cytosol.

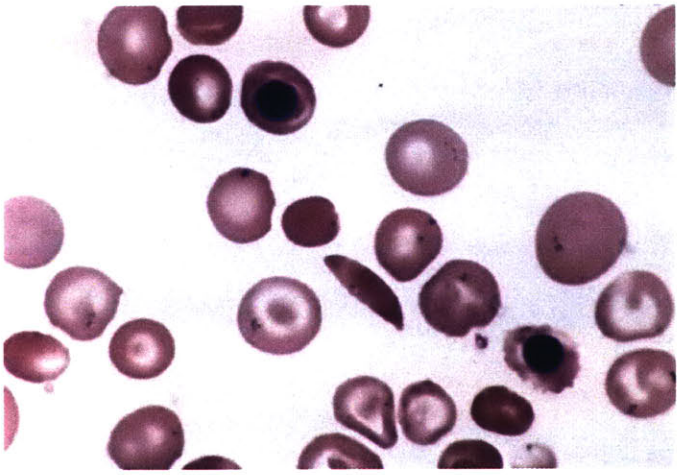

Figure 1.2. Sickled RBC and normal RBCs. Decreased oxygen tension in blood causes hemoglobin S to polymerize. When deoxygenation continues, the polymers form long fibers, resulting in a sickle-shaped RBC. The person who provided this sample lacked a spleen. The two large purple single inclusions are Howell-Jolly bodies, which are unextruded nuclear remnants that the spleen normally removes. The little clusters of iron molecules are Pappenheimer bodies. From (30). Permission for reuse granted by Kristine Krafts, M.D., University of Minnesota School of Medicine.

HEREDITARY ELLIPTOCYTOSIS

Another disease that primarily affects the mechanical properties of RBCs is hereditary spherocytosis and elliptocytosis. In this disease, mutations involving proteins that tether the spectrin-actin skeleton to the RBC membrane result in loss of membrane fragments during exposure to shear stresses in the circulation (19). In this disease, the surface area of the cells is decreased, resulting in a decreased surface area-to-volume ratio, Figure 1.3. This decreased deformability limits the ability of these cells to squeeze through the splenic cords and reenter the circulation.

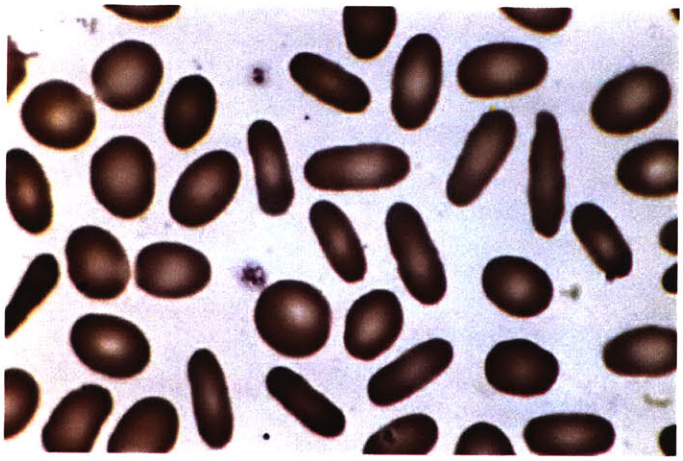

Figure 1.3. Elliptocytes. Decreased surface area-to-volume ratio is caused by mutations involving proteins that tether the spectrin-actin skeleton to the RBC membrane. This altered ratio results in cells that no longer assume the biconcave-disk shape. From (30). Permission for reuse granted by Kristine Krafts, M.D., University of Minnesota School of Medicine.

MALARIA

Globally, malaria threatens around 2.2 billion people, causes hundreds of millions of clinical attacks, and results in 1-2 million deaths (31). Malaria is believed to be the oldest and deadliest of the human infectious diseases (32), and it is a disease that has caused dramatic changes in human genetic evolution. Several genetic diseases have become prevalent as a result of malaria, including sickle cell anemia, glucose-6-phosphate dehydrogenase deficiency, thalassemia, and spherocytosis. In some African communities today, up to 30 percent of the population are carriers of the sickle cell gene. In addition to these diseases, which result in deleterious effects on a subset of the population, 97% of contemporary West and Central African populations carry the mutation for Duffy negativity and thus are protected from vivax malaria (32).

In 1880, Alphonse Laveran noticed motile, spherical bodies in the blood of patients suffering from malaria. He identified these bodies as protozoan parasites, and deduced that they were the cause of malaria. Malaria refers to the disease consequences of four different parasites: *P. falciparum*, *P. vivax*, *P. ovale*, and *P. malariae*, which are all transmitted by the female Anopheles mosquito. These parasites are eukaryotic and possess 14 chromosomes. Of these four parasites, *Plasmodium falciparum* and *Plasmodium vivax* cause the vast majority of infections.

When a person is first infected with *P. falciparum*, the parasite infects cells in the liver and incubates and replicates in these liver cells for around 12 days. After this incubation period, the parasite is released into the circulation and infects RBCs. After infection, the parasite replicates in the RBC. After 48 hours, the RBC bursts to release 16-32 new merozoites (33), Figure 1.4. The infected person responds to this cycle of infection and replication by achieving febrile temperatures every 48 hours. Untreated, *P. falciparum* infection can produce cerebral malaria, which may lead to epilepsy, blindness, cognitive impairments, behavioral disturbances, and ultimately coma and death.

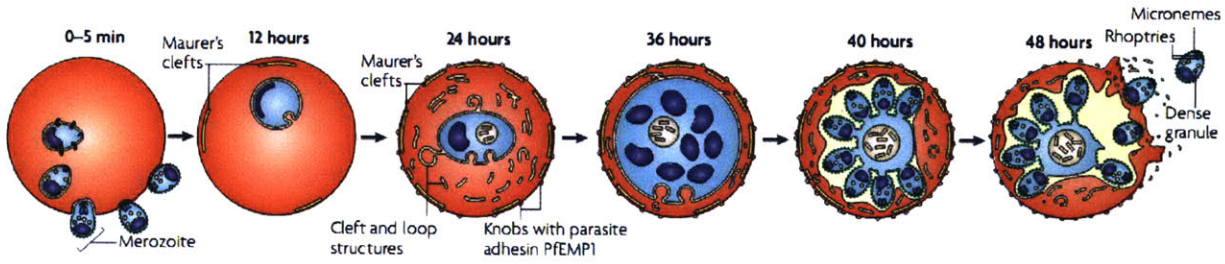

Figure 1.4. *P. falciparum* invasion of and development in a RBC. At the end of the invasion cycle, 16-32 new merozoites burst from the RBC. From (33). Permission for reuse granted by Nature Publishing Group.

In contrast to disease consequences for those with *P. falciparum* infection, consequences for those with *P. vivax* infections are relatively minor and include only temporary debilitation. Notable differences for the *P. vivax* parasite include the ability to live in the liver of an infected person for years without producing signs of infection, in contrast to weeks for *P. falciparum*. Also, in contrast to *P. falciparum*, which can infect all RBCs, *P. vivax* only infects young RBCs, reticulocytes.

Only the ring-stage infected RBCs are observed in the peripheral circulation of infected patients; mature-stage infected RBCs (trophozoite and schizont) do not circulate and are sequestered in different organs (33). Cells up to 24 hours post-infection are classified as rings, Figure 1.5. As the malaria parasite matures and replicates within a RBC during a 48 hour cycle (34), it makes the RBC progressively stiffer (6). In the ring-stage, increased stiffness is caused primarily by two proteins: Ring-infected Erythrocyte Surface Antigen (RESA) and Knob-Associated His-Rich Protien (KHARP).

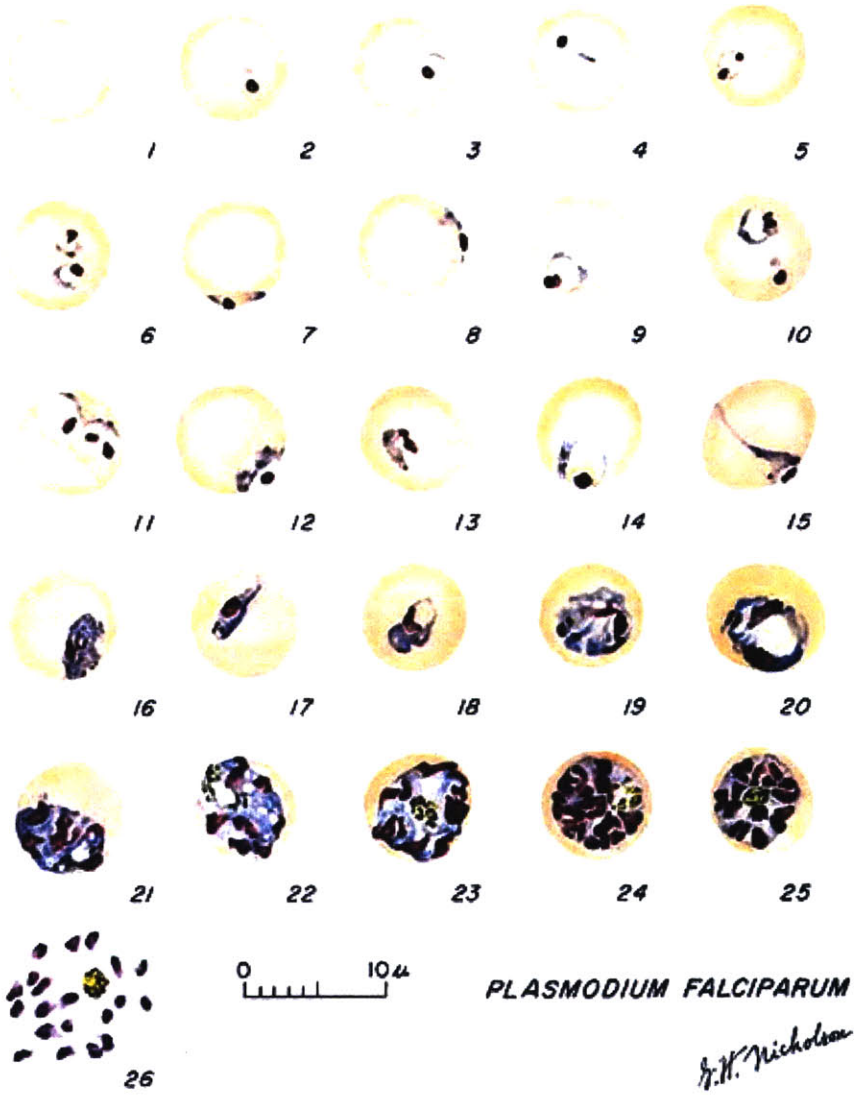

Figure 1.5. Drawing 1. Normal RBC. Drawing 2-18. Trophozoites (among these, Drawings 2-10 correspond to ring-stage trophozoites). Drawings 19-26. Schizonts. Illustration adapted from Coatney GR, Collins WE, Warren M, Contacos PG. The Primate Malarias. U.S. Department of Health, Education, and Welfare, Bethesda, 1971.

Immediately after invasion of the RBC, RESA is secreted and exported to the RBC membrane skeleton. RESA stabilizes spectrin against thermally-induced denaturation and dissociation (33), Figure

1.6 A. RBCs infected with parasites lacking RESA are more susceptible to heat-induced vesiculation, and RESA may stabilize the RBC membrane against febrile shock.

Another protein that increases infected RBC stiffness during the ring-stage is the KHARP, which appears around 16 hours post-invasion (33). This protein is located just beneath the RBC membrane and results in 100 nm-diameter knob-like protrusions, Figure 1.6 B. These knobs are the anchoring point for the membrane-embedded cytoadherence protein, *P. falciparum* Erythrocyte Membrane Protein 1 (PfEMP1). PfEMP1 is responsible for adhesion to to endothelial cells (33), which is one of the mechanisms by which late-stage malaria-infected red blood cells evade clearance by the spleen.

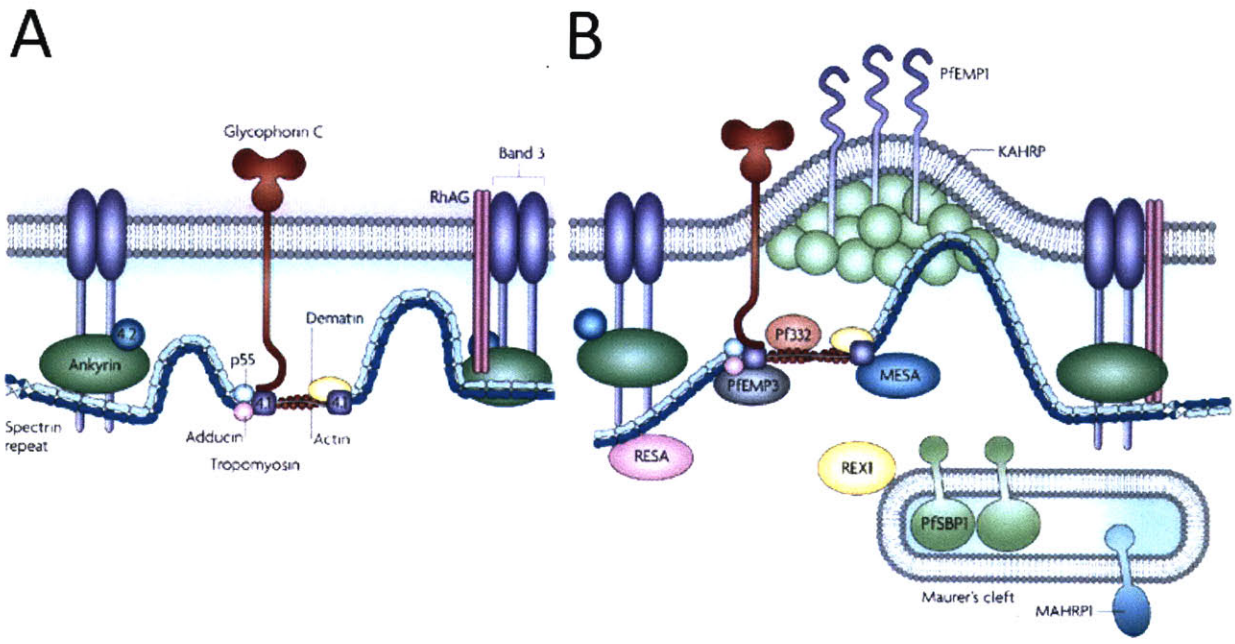

Figure 1.6. Normal and infected RBC membrane architecture. **A.** Uninfected RBC membrane. **B.** Ring-stage-infected RBC membrane. The RESA protein anchors the spectrin network to the cell membrane, resulting in protection against thermal shock. KAHRP produces knobs just beneath the surface of the membrane, anchoring the PfEMP1 protein. From (33). Permission for reuse granted by Nature Publishing Group.

PITTING

In a person with a normal spleen infected with malaria, often RBCs lacking parasites but positive for RESA protein can be seen in that person's peripheral blood. This observation implies that the malaria parasite is removed from the RBC without the destruction of that RBC. In contrast, in a person who has had his spleen removed and who is infected with malaria, dead parasites in RBCs are still in the circulation, but RBCs lacking parasites but positive for RESA are not seen (35). Furthermore, RESA-positive parasite-negative RBCs are not seen in parasite cultures in vitro (36). From these observations, one may conclude that the spleen is responsible for the removal of the parasite from an infected cell and then returning the previously-infected RBC back to the circulation. This phenomenon is referred to as "pitting", and it is believed that anemia is reduced by this process in infected individuals.

In the spleen, phagocytosis of infected cells occurs most frequently, followed by pitting and hemolysis (37). In the spleen, the pitting process is believed to be a combination of the mechanical restrictions of squeezing through the endothelial slits and phagocytosis by macrophages, Figure 1.7. The pitted RBCs become spherocytic and more susceptible to removal in repeated passages through the spleen (37). Pitted RBCs circulate for an average of 8 days compared to uninfected RBCs, which circulate for an average of 40 days (38) in infected individuals.

It has been demonstrated *in vitro* that the presence of stimulated macrophages is sufficient to pit trophozoites (39). However, it has not yet been shown whether mechanical constraints are similarly sufficient to induce pitting. It has also not been demonstrated that the presence of macrophages is necessary for the pitting process.

After a malaria-infected person has been treated with artesunate, the number of pitted RBCs rises much faster than after treatment with quinine(38). After artesunate treatment, the deformability of the infected RBCs does not change from that of infected cells absent artesunate treatment, as

measured by the optical rotational cell analyzer (35). However, this method measures the bulk deformability of RBCs, and more sensitive single-cell measurements may be more appropriate.

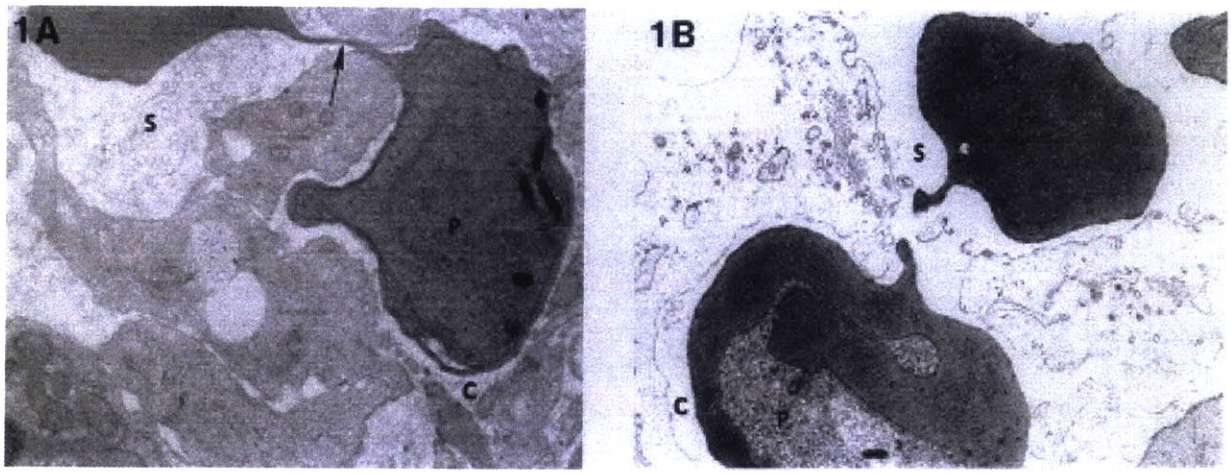

Figure 1.7. Scanning electron microscopy of the pitting process. In 1A, the two sections of the RBC are held together by a tenuous strand of RBC membrane. The portion on the left of the endothelial slit no longer harbors a parasite. Figure 1B. RBC split apart. From (40). Permission for reuse granted by AAAS.

As is apparent from our discussion, the deformability of blood cells plays a critical role in their physiological function, allowing them to transit through various filtration mechanisms in the human body such the spleen and capillaries. Disease, chemicals, or genetics may cause the deformability of blood cells to be outside normal ranges, causing significant disruption to the normal functioning of our bodies. However, the mechanical properties of cells are often neglected compared to biochemical properties for assay development. Our study here is motivated by this relative lack of attention to cellular mechanical properties in the context of laboratory and clinical equipment.

The goal of this project is to create microfluidic devices that can serve as *in vitro* models of the biofiltration phenomena that naturally occur in the human body. In one approach, we incorporate aspects of capillary geometry to create a device that measures the deformability of single RBCs. The

possible uses of this device include a low-cost field diagnostic device for malaria and a high throughput drug-screening device. In another approach, we mimic the architecture of the human spleen to continuously separate cells based on deformability. This device can be used in sample enrichment for downstream processing and analysis. These same approaches may be applicable to the study of WBCs and cells more generally.

This thesis consists of the following sections. First, in Chapter 2 we review methods for analyzing cells and give an overview of cell sorting techniques. Based on these precedents, we develop the technical requirements for the microfluidic device to be made. In Chapter 3, we summarize the materials and methods used in our experiments in the next chapters. We then present our deformability-based flow cytometer in Chapter 4 and our continuous-flow deformability-based separation device in Chapter 5. We then conclude by outlining the contributions of this thesis, discussing ongoing work, and giving our outlook of the field in Chapter 6.

Chapter 2

METHODS FOR CELL ANALYSIS AND SEPARATION

In this chapter, we survey various methods used for analyzing and separating cells, and compare them with the mechanical cell sorting methods we are developing in this thesis. Methods of cell analysis and separation are fundamentally based on differences in properties between different populations of cells. These differences can be classified into three major categories: biochemical, electromagnetic, and mechanical. Biochemical properties include differences in protein presentation on the outside surface of a cell and concentration of ions, molecules, or proteins inside a cell. Electromagnetic properties may include differences in ability of the cell membrane to polarize and inherent magnetic properties of the cell. Lastly, mechanical differences include differences in density, size, and deformability of a subset of

---

A substantial portion of this chapter was published in the following journal article:
Bhagat AA, Bow H, Hou HW, Tan SJ, Han J, Lim, CT (2010) Microfluidics for cell separation. *Medical and Biological Engineering and Computing* (in press)

cells from that of other cells in the population.

Biochemical Methods

Analysis and separation of cells based on biochemical differences is dependent on the existence of a molecule that is able to recognize a specific biochemical property of a subset of cells. Commonly used molecules include antibodies, proteins, or chemicals. Currently, there exist three main methods to analyze cells based on the existence of that molecule: attaching a fluorescent tag to that molecule and mixing the solution with a suspension of cells; coating a bead with that molecule and mixing that bead solution with a suspension of cells; and coating a large surface with that molecule and flowing a cell mixture past that surface.

Fluorescence-Activated Cell Sorting

In fluorescence-activated cell sorting (FACS), fluorescence tags are first selectively bound to a subset of cells in a population. The population is then flowed one-by-one past a detector, Figure 3.1. Parameters, such as cell size (forward scatter) and granularity (side scatter) can be acquired in addition to fluorescence intensity.

Separation of the initial mixture into multiple populations is possible. Traditionally, FACS involves ejecting single cells in liquid droplets around 70 μm, similar to how an inkjet printer ejects ink on paper (41). Each liquid droplet is first analyzed by the detector and then deflected using charged electrical plates to different buckets for collection. Drawbacks to this method include the equipment expense, clogging, contamination, serial nature of the sorting, and cell viability after ejection, deflection, and impact (42). The maximum sort rate is on the order of 100,000 cells/s, based on physical principles

(43), although a fiber-optic array scanning technology has been reported to analyze cells attached to an adhesive slide at a speed of 300,000 cells/s (44). For the small affordable instruments, typically low cell yields are obtained (10^3 cells/s) (45).

More recently, the fluorescence-based sorting of cells has been accomplished using methods that are more easy to implement, which obviate the need to eject the cells in liquid droplets. These new methods involve microfluidic devices, which enable the handling of small numbers of cells (from 100-100,000), compared to minimum number of 100,000 cells required for typical FACS machines (46). These methods involve flowing the cells past a T-junction. Optical forces (~100 cells/s) (46), electroosmotic flow (~20 cells/s) (42), and hydrostatic pressure changes(~1 particle/s) (47, 48) can sufficiently influence whether each cell is deflected left or right at the T-junction. Fundamental drawbacks to these methods are the equipment expense and the inherent serial nature of detecting the fluorescence intensity of each cell, which results in long analysis and sorting times. Dielectrophoresis (49) and large-scale optical-driven dielectrophoretic manipulation(50) may be used to separate many cells in parallel, although these methods have not been explored in depth for FACS.

MAGNETIC CELL SORTING

One method to increase sorting speed is to first coat magnetic beads with the recognition molecule and then mix that magnetic bead solution with a solution of cells. Then a magnetic field can be used to pick out the magnetic beads, which in turn picks out the cells. In contrast to FACS, which is serial in nature, cell sorting based on magnetism is parallel, resulting in higher throughput. Up to 10^{11} cells can be processed in 30 minutes (51). It is believed that the magnetic particles do not influence viability or function of the labeled cells and do not affect the results of FACS later (51, 52). There are two main collection methods for this method of cell sorting: continuous-flow and batch processing.

A large-scale method of sorting based on attached magnetic beads involves a quadrupole magnetic placed next to a liquid column (53). A cell solution flows through the column, and cells attached to magnetic beads are deflected in one direction, while cells that do not have beads attached continue to go straight. A miniaturized version of this method involves parallel magnetic lines placed oblique to the direction of liquid flow in a parallel-plate flow chamber (52, 54), Figure 2.1. Cells attached to magnetic beads follow the direction of the parallel magnetic lines, while other cells follow the direction of the liquid. Limitations to this method include cell adhesion, low throughput, and low recovery (perhaps due to the variations in the number of beads attached to the cells) (54). A similar method involves bacterial cells attached to polystyrene beads and oblique parallel electrical lines operated under alternating current conditions (55), Figure 2.2. Cells attached to beads would be deflected into the collection channel, while unlabeled cells would be deflected into the waste channels. Throughput was measured at ~10,000 cells/s.

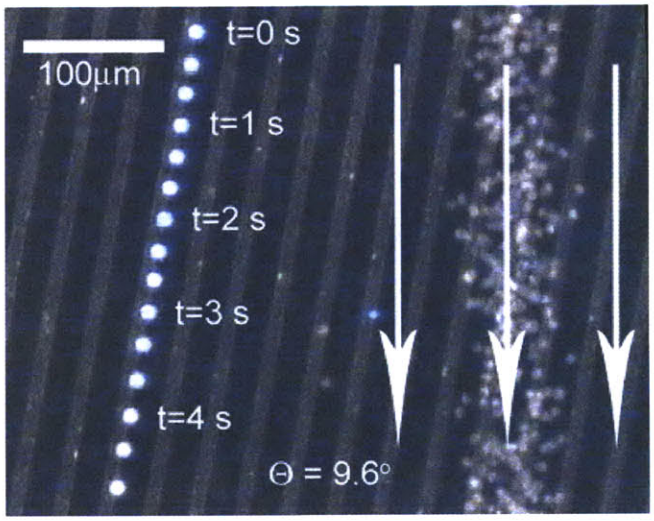

Figure 2.1. Continuous-flow magnetic bead-based cell sorting. A single tagged WBC moves along a magnetic strip at 110 μm/s, while RBCs move the direction of fluid flow. All cells entered the chip at the same point approximately 1.5 mm above the field of view. From (54). Permission for reuse granted by the American Institute of Physics.

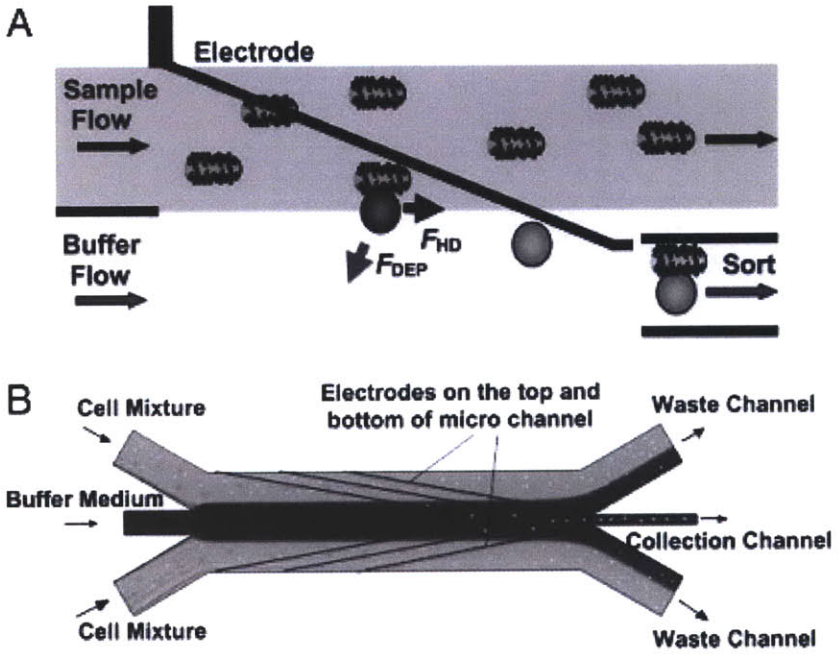

Figure 2.2. Continuous-flow dielectrophoresis-based cell sorting. Cells attached to a dielectrophoretically-responsive label are directed to the center of the stream, while unattached cells follow the direction of fluid flow. From (55). Copyright PNAS, 2006. Permission for reuse not needed (noncommercial and educational use).

After labeling the cells with magnetic beads, batch processing involves flowing this batch of cells past a strong magnetic field. Cells that are not attached to magnetic beads flow through, while cells attached to beads stay on the column. This method is called Magnetic-activated cell sorting (MACS), which is a trademark of Miltenyi Biotec. A large-scale example of batch processing is the placement of magnets next to a column filled with ferromagnetic material, such as steel wool coated with plastic to prevent cell damage (56). Smaller-scale examples of batch processing involve magnets placed next to a microfluidic channel (57, 58) and local magnetic fields created by an orthogonal array of electrical wires (59).

Advantages to MACS include the possibility of collecting large numbers of cells at one point in time (sorting in parallel) and relatively low cost. However, there are several drawbacks to the method, such as low sensitivity (difficulty capturing cells in subpopulations below 1% (56)), the tedious process of labeling cells with the magnetic beads, and the necessity of taking the beads off from the collected cells.

AFFINITY-BASED CELL SORTING

The last major method of biochemical cell analysis and sorting involves coating a large surface with the affinity molecule or protein. Then a mixture of cells is flowed past this coated surface. This method is relatively new compared to the other two methods, partly because of the expense of the affinity molecule and the recent advances in creating large surfaces that ensure contact between each cell and the surface for binding: one critical factor necessary for this method is for all cells in that mixture to touch a coated surface at least once to achieve efficient cell capture. Again, there are two approaches to this method: continuous-flow cell separation and batch processing.

Currently, continuous flow separation involves coating a surface with affinity molecules in parallel lines oblique to the fluid flow direction (60, 61). As cells flow past these lines, adherent cells are caught by the line and roll parallel to it, while non-adherent cells flow in the direction of the fluid (61). Although the necessary working mechanism of this method has been recently demonstrated, the main limitation that must be overcome is sensitivity. Currently, only a very small minority of the cells ever come in contact with the parallel lines of affinity molecules. Then the vast majority of the cell population with the desired surface trait is not collected.

Batch processing involves coating the entire surface of a channel with the recognition molecule and flowing a mixture of cells through this channel. This method was initially developed to exploit the adhesive cell rolling and transient tethering of white blood cells to artificial blood vessel walls (62), and

thus separating these white blood cells from red blood cells. In theory, because red blood cells do not interact with the recognition molecule, their velocity would be the same as that of the ambient fluid. However in practice, the separation resolution was poor due in part to the white blood cells not consistently adhering to the surface.

Antibody-coated surfaces have been developed to capture specific cells in a population (24, 63). In a preliminary study, a channel with different flow velocities was used to determine the sensitivity and strength of T and B lymphocyte capture with different fluid velocities (63). Later, a device similar to that used in the adhesive cell rolling study was coated with antibodies to epithelial cells and shown to be able to capture rare circulating tumor cells (24), Figure 2.3. Cells that the antibody recognizes are captured and immobilized on the channel wall, while other cells are simply carried away by the flowing liquid. The immobilized cells are later collected by flowing liquid at higher velocity through the channel, which detaches the cells from the adhesive walls. The device is able to process untreated human blood at a rate of 1 mL/hour and isolate cells with frequencies on the order of 10 to 1000 per mL of blood. While this method is sensitive and selective collecting very rare cells, it does not work well for cells of higher abundance due to clogging issues. Another study that examines batch cell collection uses different geometrical features around 400 nm in size that are etched into the surface of the channel (64). In this study, cancer cells tend to detach more readily in the presence of liquid movement.

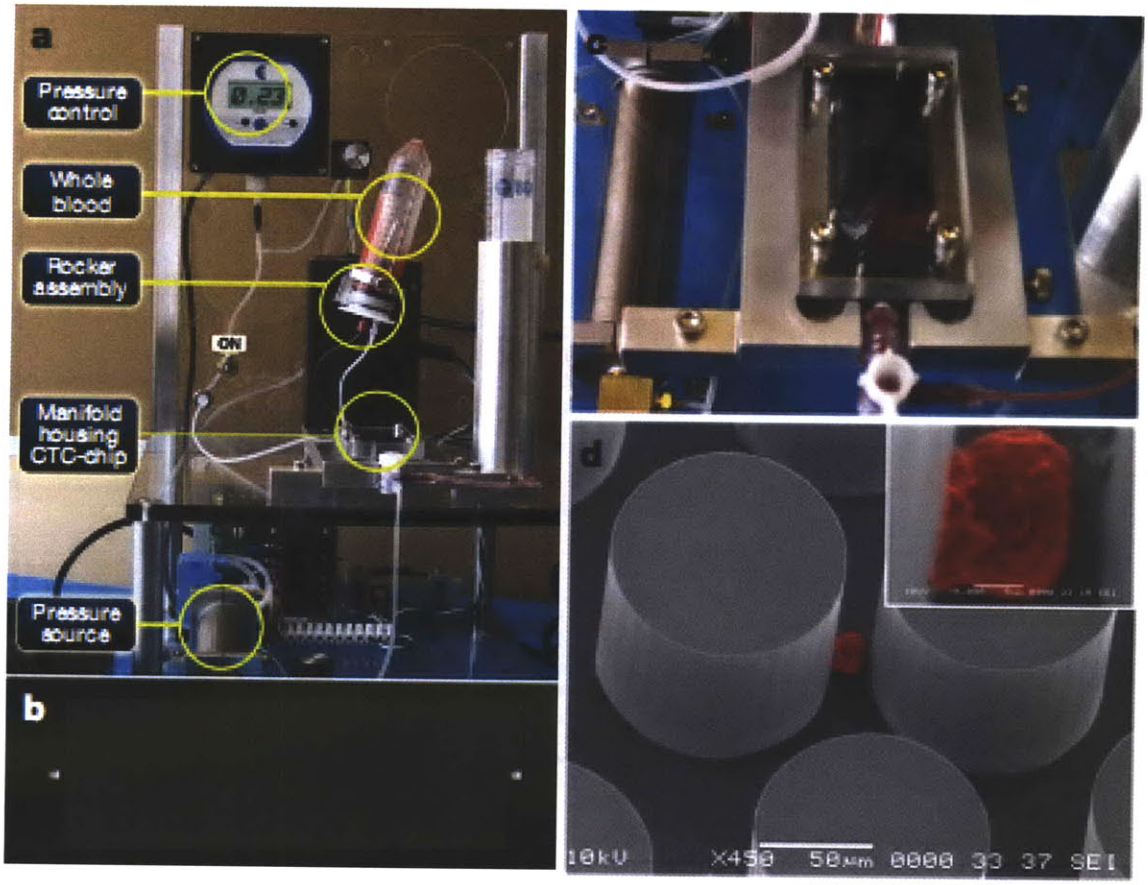

Figure 2.3. Affinity-based isolation of circulating tumor cells from whole blood. **A.** Workstation setup. **B.** Chip. **C.** Whole blood passing through chip. **D.** SEM of captured cell attached to micropost. From (24). Permission for reuse granted by Nature Publishing Group.

ELECTROMAGNETIC METHODS

Electromagnetic cell analysis and separation is based on inherent differences in electrical or magnetic properties between different populations of cells. Methods that use electromagnetic forces to separate cells that are fundamentally based on other cell properties are mentioned in other sections. Electromagnetic cell analysis and separation is accomplished using either an alternating current (AC) electromagnetic field, which includes light, or a stationary magnetic field.

The separation of cell populations based on their inherent electrical or magnetic properties has been demonstrated with cultured cell populations and artificial particles. However these methods are difficult to implement with actual clinical samples due to several reasons: the electrical and magnetic properties of the buffer needs to be carefully controlled to make the cells sensitive enough to the electromagnetic fields and electromagnetic properties tend not to differ significantly between similar cell types.

AC ELECTROMAGNETIC FIELD-DRIVEN TECHNIQUES

There are two methods to separate populations of cells using an AC electromagnetic field: dielectrophoresis and light. Dielectrophoretic forces are caused when a nonuniform electric field interacts with the induced electrical polarization, or dipole, of a cell. These forces tend to hold the cell in place and tend to be different in magnitude for cell populations of different electromagnetic properties, including membrane properties (permeability, capacitance, and conductivity), internal conductivity, and size. Typically, these forces hold cells of one population better than another population. When ambient fluid velocity is increased, the cells held with less force are washed away. The types of cell populations that have been separated include bacteria from peripheral blood (65), one cell population from another

cell population (66), and cultured cancer cells from normal cells (67, 68). Several drawbacks of this method of cell separation include sensitivity, as it is difficult to make every cell come close to at least one dielectrophoretic trap; equipment expense; and scale.

Light has been used to separate particles depending on their optical polarizability. Demonstration of this technique using interferometric patterns of light for separations based on size (protein microcapsules) and refractive index (separating polymer from silica spheres) has been accomplished (69), however cell separation has not yet been demonstrated.

DC Magnetic Field-Driven Techniques

The use of a constant magnetic field to separate cells based on their inherent magnetic properties has been proposed, although not demonstrated. In contrast to MACS, where cells are attached to magnetic beads, this method relies on the inherent magnetism of each cell in a population. An attempt to separate red blood cells from white blood cells has been published (70), based on the principle that white blood cells are diamagnetic and red blood cells can be either paramagnetic or diamagnetic. However, the results from the study only show the deflection of red blood cells from a magnetic field but no actual separation of cells.

MECHANICAL AND PHYSICAL METHODS

Cells can be separated based on differences in their mechanical and physical properties. These properties can be classified into three categories: density, size, and deformability. Separation by density has already been well established for several decades and is widely used. Separation by size has also been well-developed, while separation by deformability is not yet mature.

DENSITY-BASED SEPARATION

Separation of different populations of cells based on their density has already been well established. In most cases a density gradient is mixed with the cell population and centrifuged. A commonly used protocol involves the use of a polysaccharide gradient (ficoll), which isolates mono-nuclear white blood cells from red blood cells and platelets (71). The advantages of this method are that it is relatively inexpensive and straightforward to perform. However, the drawbacks are that the repeated washings required take on the order of hours and large volumes of cells are necessary.

SIZE-BASED SEPARATION

Size-based separation can be accomplished in batch form or continuously. Size-based separation of cells in batch form is typically accomplished with the use of a filter. Cells smaller than the pores in the filter flow through it, while cells larger than the filter pores are immobilized. This immobilization may also be useful from the perspective of time-lapse cell studies. One example of a filter used to accomplish size-based separation of cells is emulsion photo-polymerization of a gel in a microchannel subsection (72). In this study, the gel immobilized the white blood cells and red blood cells in 1 μl of whole blood, while the serum and platelets escaped.

Most other studies of batch microfluidic size-based cell separations involve microfabricated pores that form the filter. Two types of pores have been researched: individual holes smaller than the cells and dam-like structures, where the slit is smaller than the smallest dimension of the cell. Li et al. developed a simple process involving the use of printed circuit boards as masters to create micron-sized pores to hold cells in place (73). Gifford et al. created V-shaped structures to immobilize and measure the volumes of red blood cells (74). Dam-like structures have also been used for size-based cell separation and concentration. Zhu et al. separated 2 bacteria species by using a single wier that was intermediate in size to the two species (75). Chen et al. attempted to separate cultured tumor cells from peripheral blood based on their size differences using two dam-structures (76). All of these methods mentioned suffer from the problem of device clogging after a sufficient number of cells occlude the pores. One method to circumvent this clogging problem is to have fluid flow oblique to the dam structure. Yang et al. created a cell-holding device by flowing fluid at an angle to the dam structure(77). In all of these situations, constant fluid flow is required to hold the cells in place.

More recently, continuous-flow methods of size-based cell separation have been developed by several groups. Hawkes et al. used an ultrasound standing wave to transfer yeast cells from one medium into another (78). Crowley et al. created a device to separate plasma from whole blood by using capillary-driven flow to pull fluid at an angle to small pores (79). Perhaps the most innovative continuous-flow device developed is the bump array, which functions by using circular pillars to deterministically push larger particles one direction while letting smaller particles flow according to the fluid streamlines. Davis et al. used this method to separate red blood cells from white blood cells and plasma from blood cells (80), Figure 2.4. The throughput of this device was relatively fast, at 1 μl/min.

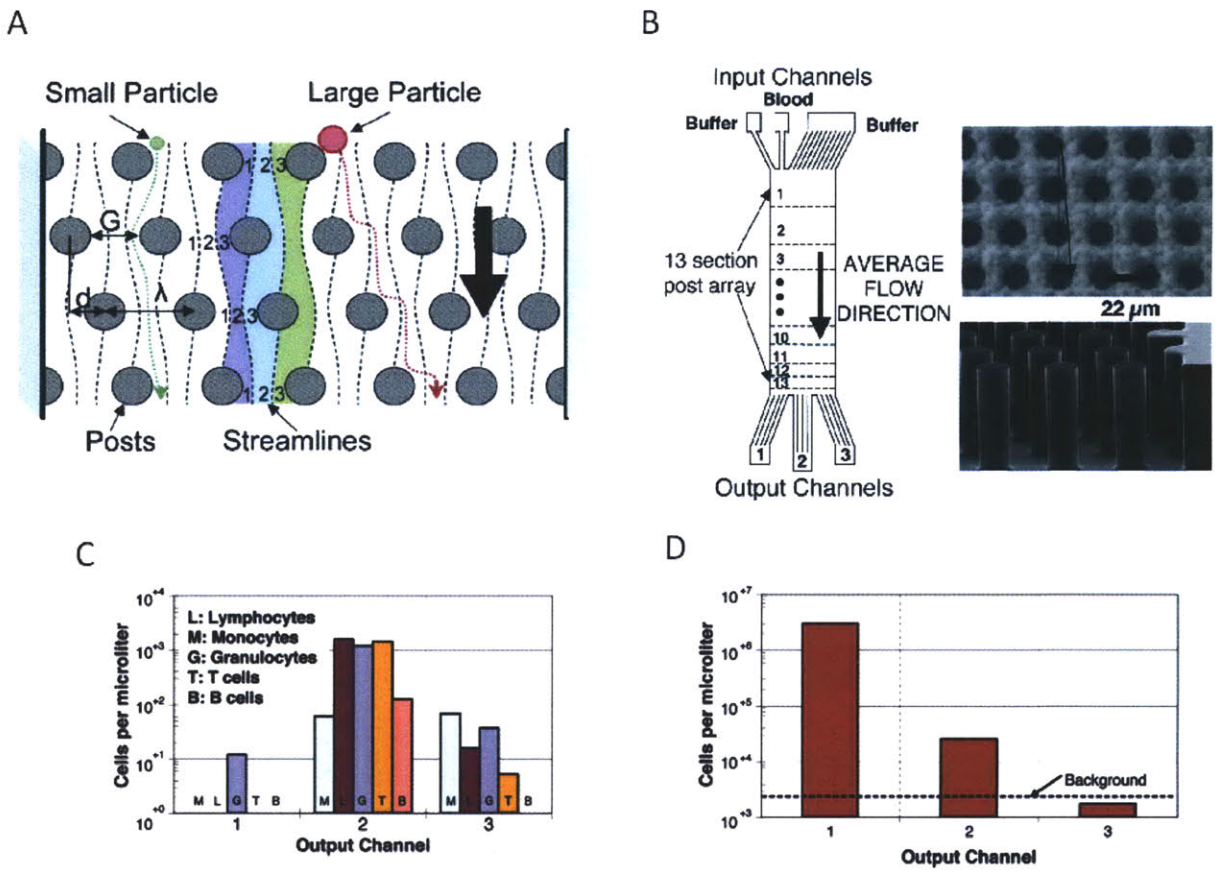

Figure 2.4. Continuous-flow size-based cell separation. A. Schematic illustrating separation mechanism. **B.** Device structure. **C.** WBC concentrations at the output channels. **D.** RBC concentrations at the output channels. From (80). Copyright PNAS, 2006. Permission for reuse not needed (noncommercial and educational use).

CELL DEFORMABILITY-BASED MEASUREMENT AND SEPARATION

Cell deformability may be more difficult to characterize than density or size, and for this reason it may be less explored than the other two mechanical characteristics. Deformability, at least for RBCs, can be decomposed into three components: the internal viscosity, the surface area-to-volume ratio, and membrane viscoelasticity (28). For RBCs, the membrane surface area cannot expand. For WBCs, there is

excess membrane surface area at isotonic conditions, and for neutrophils this excess surface area is 2.6x that in isotonic conditions. There are two methods to assess the deformability of a cell: stretching and compressing the cell. Stretching the cell typically requires the attachment of beads to two points on the cell and pulling on the beads to stretch the cell. This method has been used to study hereditary cytoskeletal anomalies by artificially creating those anomalies in red blood cell samples (81) and proteins that the *P. falciparum* parasite exports to the RBC membrane(82), Figure 2.5. This method primarily examines properties of the cell membrane.

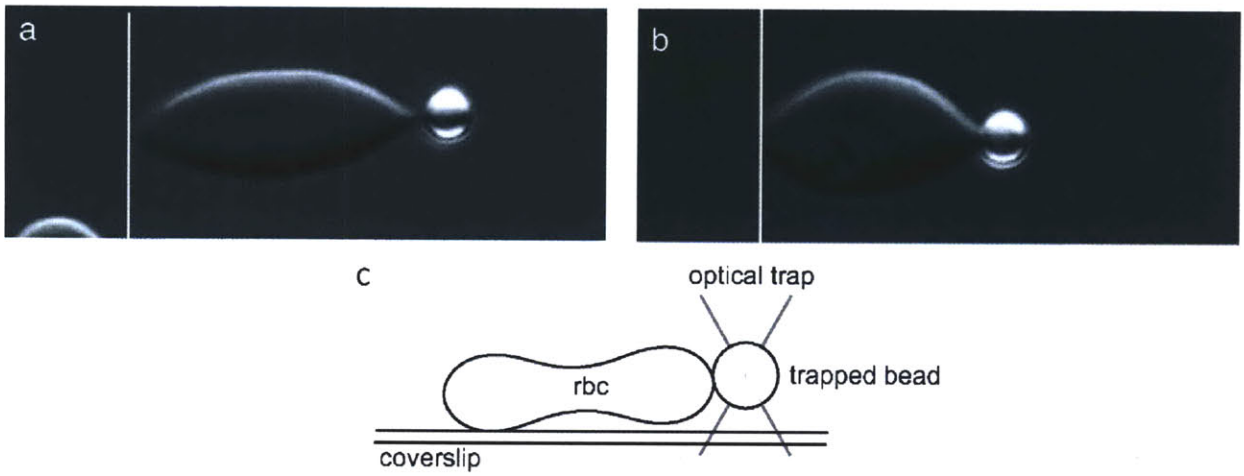

Figure 2.5. RBCs stretched using optical tweezers. A. Healthy RBC stretched using 100-pN force. B. *P. falciparum* malaria-infected RBC stretched using the same force. C. Schematic side-view of optical tweezers stretching a RBC. From (82). Copyright PNAS, 2007. Permission for reuse not needed (noncommercial and educational use).

Compressing the cell can be accomplished in two ways: pushing on the cell at a single point and pushing on the cell at multiple points at the same time. Pushing on a cell at a single point is typically accomplished by using an atomic force microscope (AFM). These studies can be grouped into two main categories: analysis of adherent cells and nonadherent cells. Adherent cells are typically epithelial cells.

In these studies, it is generally found that cancer cells are more deformable than normal cells. This property enables them to easily exit the bloodstream at a remote location and start a cancerous colony there. Lekka et al. studied cultured human bladder cell lines and found that normal cells have a Young's modulus of about one order of magnitude higher than cancerous ones (83). Also, Cross et al. studied lung, pancreas, and liver cell samples obtained from the pleural fluids of patients and found that in general cell stiffness of metastatic cancer cells is more than 70% softer than that of benign cells (13).

In contrast to studies involving adherent epithelial cells, studies of leukemia cells, which are typically nonadherent, find that cancer cells are in general *more* stiff than normal cells. This increased stiffness often causes leukostasis, clogging in the vasculature. Performing AFM on white blood cells immobilized in wells, Rosenbluth et al. found that acute myeloid leukemia cells are 6 times stiffer than normal human neutrophils (11). Also, Lam et al. found that chemotherapy drugs increase the cell stiffness of white blood cells, which increases the risk of vascular complications (12). Lastly, Chronis and Lee created heat-activated microtweezers to grip single HeLa cells in solution (84). Although cells can be captured, measurement of cell deformability using such a design may be difficult. In all of these studies, sample preparation is usually laborious and data acquisition must be done serially. Furthermore, equipment expense and technical skill in operating the machine is a major hindrance to this method being applied more universally.

Instead of compressing a cell at a single point, a class of cell analysis and separation devices compresses a cell at multiple points simultaneously. This class can be split into two categories: optical compression and pressure-driven movement through pores. Optical cell compression has primarily been explored by Guck and colleagues. In their setup, a square capillary is positioned orthogonal to a gap in an optical fiber carrying focused laser light (85-87), Figure 2.6. As cells pass by this focused laser light, each cell is deformed. The throughput of this method is on the order of 100 cells/hour, and analysis of each cell takes on the order of 10 seconds (87). Several drawbacks of this method include the low

throughput, inability to measure the absolute deformability of each cell (as opposed to the relative deformability compared to other cells), device manufacturing complexity (requiring integration of an optical fiber into a chip), and high cost for a coherent illumination source.

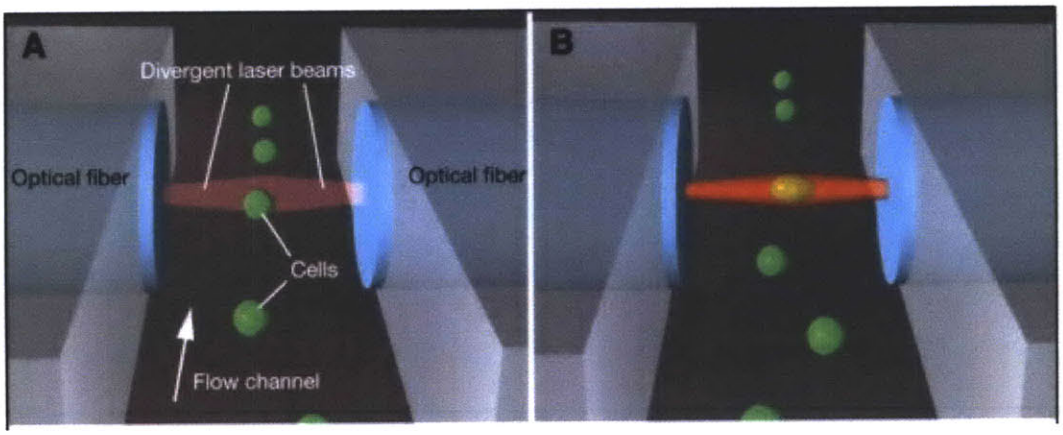

Figure 2.6. Optical trapping and stretching of cells. Two counterpropagating divergent laser beams trap individual cells flowing through a microfluidic channel. From (86). Permission for reuse granted by Biophysical Journal.

Perhaps the most widely used method to study the elastic and rheoviscous properties of individual cells is accomplished by micropipette aspiration, which was developed in the early 1970s (88, 89), Figure 2.7. Micropipette aspiration involves tracking the leading edge of a cell as it is sucked into a small glass tube, which can be accomplished to an accuracy of around 25 nm (90). The main cell deformability parameter measured by micropipette aspiration is the surface tension of the cell membrane. However, it is difficult for theoretical models to resolve the differences in cell mechanical properties generated by AFM and micropipette aspiration (91). Studies using micropipette aspiration have shown that cultured cancerous rat fibroblast cells are more deformable than cultured non-cancerous ones (92), red blood cells become more rigid over a period of 24 hours as ATP decreases and

calcium increases (93), and increasing the hemoglobin concentration of sickle cells increases extensional rigidity (10). Drawbacks to micropipette aspiration studies include the inherent serial nature of studying each cell, throughput, and labor intensiveness.

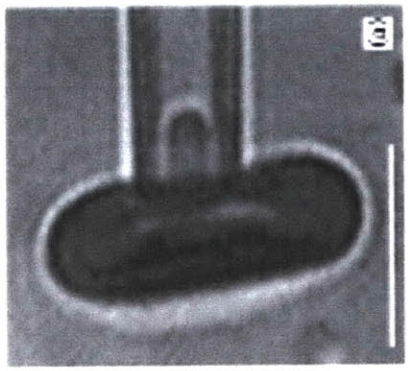

Figure 2.7. Micropipette aspiration of a red blood cell. Length bar is 5 μm. From (94). Permission for reuse granted by Elsevier.

Microfabricated devices enable the creation of custom structures similar to micropipettes, so that parallel and repeated measurements can be made on the same cell. In contrast to the glass micropipettes used in micropipette aspiration, microfabricated structures can be reproduced to an accuracy of nanometers. There are three configurations of microfabricated pores for the purpose of studying cell deformability: a single pore, pores in parallel, and parallel arrays of pores in series. Studies involving a single pore have been used to study the deformability of malaria-infected red blood cells (95), Figure 2.8. Malaria-infected red blood cells were determined to be less deformable than uninfected red blood cells and recovered their original shapes slower after passing through the constriction. Also, squeezing malaria-infected cells through small constrictions forced the malaria parasite to exit the cell, a phenomenon termed pitting. In another study, two channels in parallel were used to determine rapid variations in pressure needed to push red blood cells that were artificially made more rigid through one

of the channels (96). A colored fluid was flowed through the second channel, and the transition between the two fluids was used to determine the pressure drop across the first channel. Studies involving a single pore are often limited by both sensitivity and specificity of detection, due partly to stochastic measurement noise and the cells' natural variation in size and other properties. Also, the clogging of the single pore renders the device useless.

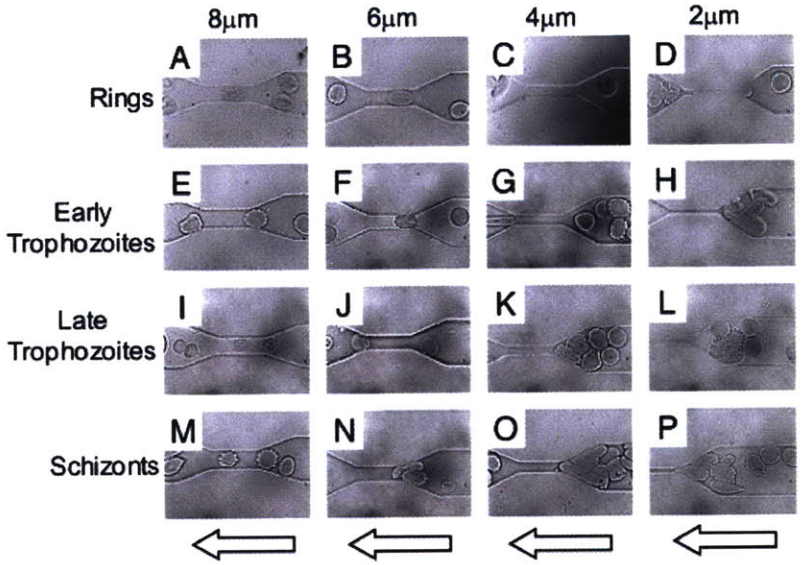

Figure 2.8. Size of microfabricated pore vs. stage of malaria-infection. Ring-stage infected RBCs were able to pass through all constrictions, however trophozoites and schizonts were only able to pass through the largest chanels. From (95). Copyright PNAS, 2003. Permission for reuse not needed (noncommercial and educational use).

Parallel arrays of pores overcome some of the challenges faced with using a single pore, such as throughput and clogging. Tracey and coworkers have investigated the relationship between cell length and velocity for iron-deficiency anemic patients' red blood cells (97), normal red blood cells (98), and red blood cells from a thalassemia patient (99). Tsukada et al. performed similar tests on erythrocytes from a patient with diabetes mellitus and found that erythrocytes from diabetic patients were stiffer than

those from normal patients. Lastly, Abkarian et al. used parallel channels to determine how the formation of stacks of several red blood cells can reduce the apparent viscosity in small capillaries (100). While parallel arrays of pores increase sample throughput, the same challenges faced by single pores involving measurement sensitivity are encountered.

Parallel arrays of pores in series allow high-throughput repeated measurements of cells deforming and relaxing. Additionally, this method of cell analysis bypasses clogging issues and enhances sensitivity by repeated measurements on each cell. However few groups use this platform for studying cell deformability. Brody et al. created such a device and found that mobility, and hence deformability, in such a device is inversely correlated with the intracellular calcium concentration and that the rigidity of a cell may change as it passes through such an array (7), Figure 2.9. Based on the same device, Carlson et al. found that lymphocytes migrate farther than granulocytes in repeated constrictions based on adhesion and avoidance of one cell population from the other (101). Using a similar device, Mohamed et al. attempted to separate cultured neuroblastoma cells from whole blood (102) and fetal cells from maternal blood (103).

To our knowledge, all of the microfabricated devices used to study cell deformability involve pores that resemble the circular opening of pipettes used in aspiration experiments. Namely, the pores have rectangular entrances with rectangular cross sections of aspect ratios less than 2:1. We believe the ability to create pores of arbitrary geometry is an area that has not been studied and may lead to greater understanding of cells' biophysical properties.

Often in studies involving microfabricated pores, cells are immobilized at the entrance of the pores and obstruct fluid flow. Gifford et al. exploited this effect and created a device that is able to easily measure the surface area and volumes of thousands of cells in around 10 minutes (74), Figure 2.10.

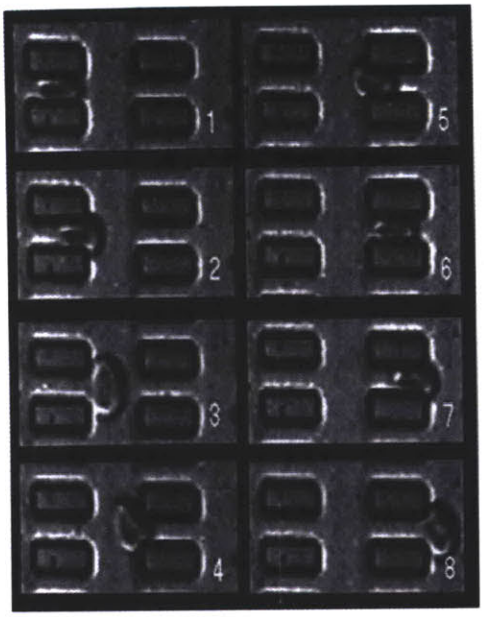

Figure 2.9. RBCs flowing through 4 μm-wide channels. Frames are spaced 0.2 s apart. From (7). Permission for reuse granted by Elsevier.

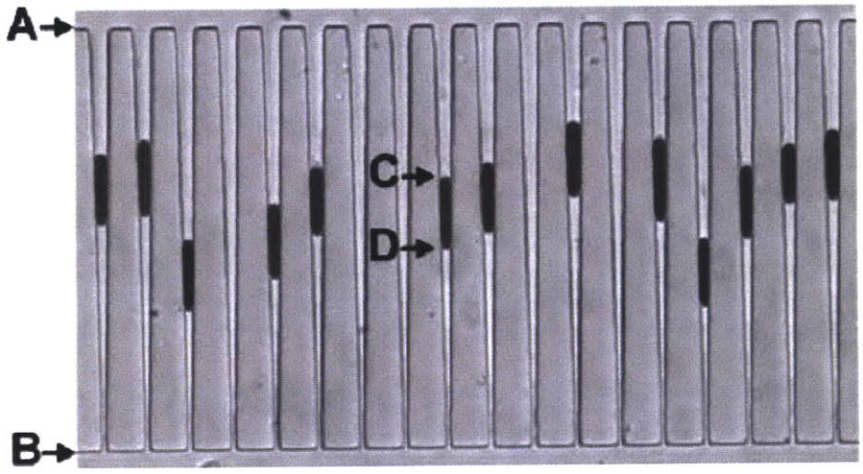

Figure 2.10. RBCs squeezed in wedge-shaped microchannels. The microchannels are 80 μm long and 3.4 μm deep. The channel width at the entrance is 3.44 μm and the width at the exit is 0.95 μm. From (74). Permission for reuse granted by Elsevier.

Chapter 3

MATERIALS AND METHODS

In this chapter, we describe all materials and methods used in our experiments. We start by explaining details regarding the manufacture of the device. We then discuss biological sample preparation. We then end the chapter by describing data analysis and modeling.

MASK DESIGN

We designed our masks using CleWin Layout Editor Version 3.09. The design of the mask is probably the most important aspect of the entire project, and we followed several principles in carrying out the design. Most of these principles are based on the fact that it is virtually impossible to create a perfect device on the first try, so accommodations must be made. These principles can be categorized

into estimating dimensions, provisioning for misalignment of multiple layers, designing reservoirs, and compensating for fluidic resistance.

It is difficult to know exactly what device dimensions will work best, but an estimate can be made regarding dimensions that span that optimal value. For example, a RBC is approximately 8 μm wide and 2 μm thick, and it deforms substantially during capillary transit. A quick estimate regarding the diameter of capillaries that the cell can easily transit is then $\sqrt{8 \cdot 2} = 4$ μm. We then create 3-5 device designs around this size, evenly spaced apart (e.g. 2 μm, 3 μm, 4 μm, and 5 μm). During the etching processing described later, we typically create 3-5 wafers with each wafer etched to a different depth, which is evenly spaced. An advantage in microfluidic devices is that it is possible to incorporate many possible designs on a single chip. Furthermore, it is possible to include several channels in parallel (in the electrical sense) to reduce the number of times it is necessary to set up an experiment and better control experiment conditions. An example this idea is shown in Figure 3.1.

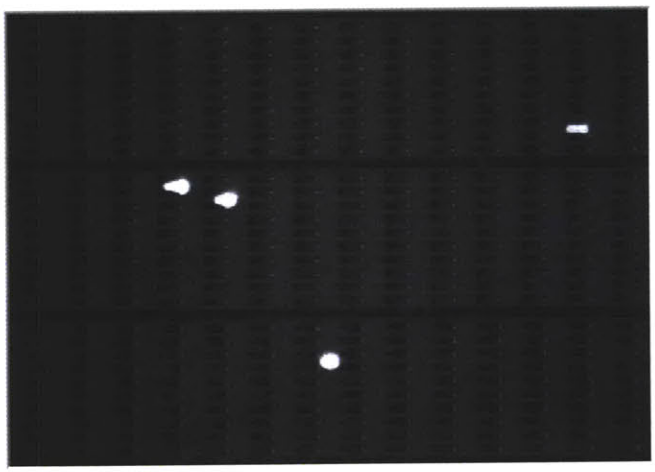

Figure 3.1. Three parallel channels incorporating different constriction geometries. The top channel has octagonal pillars, the middle channel has converging triangles, and the lower channel has diverging

triangles. During one experiment run, three sets of data can be simultaneously acquired. RBCs are dyed with CellTracker Orange, and the gaps between the pillars are 3 μm at the minimum point.

For the polyurethane devices, we typically etch the silicon wafer twice, to two different depths. Etching the wafer twice requires the second etch mask to be aligned to the results of the first etch. Because it is almost impossible to align the two exposures with perfect precision, we allow a tolerance such that an alignment offset of that tolerance is acceptable and will result in a working device. If the device is made using contact photolithography with a minimum feature size of 10 μm, we allow a tolerance of 30 μm horizontally and vertically. If the device is made using the Nikon wafer stepper in the ICL, which can produce a minimum feature size of 500 nm, we allow a tolerance of 2 μm in each dimension.

Inevitably when running experiments, debris such as dust or agglutinated cells will enter the device. To prevent this event from interfering with the operating region of the device and stopping the experiment, it is necessary to place filters upstream of the operating region. In our designs, we include 2 mm by 2 mm-square reservoirs in the mask design. In these reservoirs, we place 10 μm-diameter pillars spaced 10 μm apart. Later in the fabrication process, a 1.5 mm-diameter hole will be punched in this reservoir for insertion of tubing. Because the filter region is somewhat larger than the punched hole, a few of the pillars will be located between the liquid entrance point and the operating region, thus filtering out debris. An illustration of the filtration design is provided in Figure 3.2.

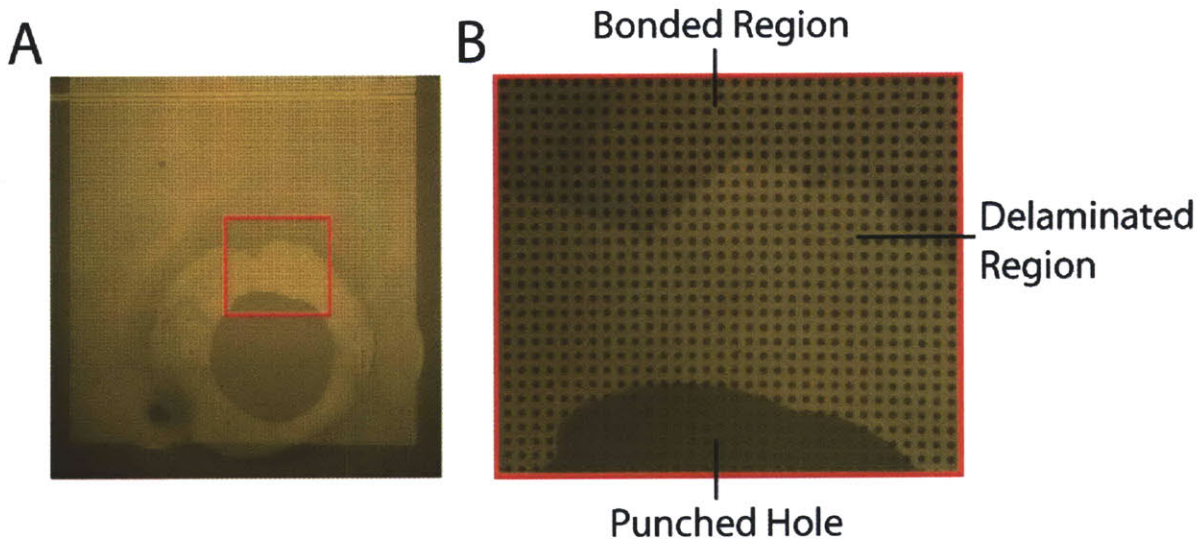

Figure 3.2. Filtration Pillars. **A.** The reservoir is a 2 mm by 2 mm square. The punched hole is 1.5 mm in diameter. **B.** The diameter of the bored PDMS cylinder encompasses the delaminated region.

In the design of devices where there is a large rectangular area connected on all four sides by fluidic access channels, it is necessary to correctly match the fluidic resistance of these access channels to the central region so that the fluidic streamlines are straight in the central region (104). An illustration of the device design is provided in Figure 5.8.

PMDS Microfluidic Device Fabrication

Steps for fabricating a silicon mold for PDMS microfluidic devices

1. Coat a 6" silicon wafer with 1 μm-thick photoresist using the coater6 (SSI-150) in MIT MTL's ICL.
2. Pattern the wafer using the istepper (Nikon NSR2005i9 5x reduction step-and-repeat projection stepper) in MIT MTL's ICL.
3. After developing the photoresist using the coater6 (SSI-150), check that the patterns are accurate.
4. Etch into the patterned silicon wafer using the STS2 (ST Systems Multiplex ICP tool) in MIT MTL's TRL. The specific recipe that we use is panscall, with an etch time of 16 minutes for a depth of 4.0 μm.
5. Remove the photoresist by ashing the wafer using the asher (Matrix 105 Asher) in MIT MTL's ICL.
6. Measure the depth of the etching by using the P10 (Tencor profilometer) in the MIT MTL's ICL.

Steps for creating a PDMS device

1. Silanize the wafer by exposing it to Trichloro (1H, 1H, 2H, 2H-perfluorooctyl) silane (Sigma-Aldrich) for 1 hour. We place 100 μl of the silane in a small aluminum cup and put this cup along with the wafer in a plastic vacuum jar. We draw vacuum for 5 minutes, and then hermetically seal the jar for 1 hour. This silanization step prevents the PDMS during casting to adhere irreversibly to the surface of the silicon wafer. Be careful: silanes are dangerous and should be handled only in a fume hood. To check that this process is completed successfully, we drip 1 droplet of de-ionized water onto the surface of the wafer and examine the contact angle. We would like the surface to be hydrophobic, with a contact angle less than 90°.

2. Prepare the PDMS (Slygard 184 Silicone Elastomer (Dow Corning)) for casting by mixing 10 parts of elastomer base to 1 part of curing agent and churn this mixture until the result is homogeneous.
3. Degas this mixture in a vacuum jar for 1 hour.
4. Create a 1 cm-high wall around the silicon wafer from aluminum foil.
5. Pour the PDMS mixture onto the wafer and put it in the 65° oven overnight.
6. After the PDMS has been cured, peel the PDMS off from the silicon wafer.
7. Cut this sheet of PDMS using an X-acto knife.
8. Punch access holes in the PDMS device using a Miltex biopsy punch of 1.5 mm diameter. Remove the bored holes.
9. Expose both a clean glass slide and this PDMS piece to oxygen plasma in a Harrick plasma cleaner/sterilizer. Specifically, we draw vacuum for 2 minutes, and expose the pieces to plasma for 1 minute. This step makes both surfaces hydrophilic and ready to form covalent bonds to each other.
10. After taking the glass slide and the PMDS piece out of the oxygen plasma chamber, carefully put the pieces in contact with each other. Check that the pieces have bonded by looking at the device under a microscope.
11. Wrap the device in aluminum foil and put it in the 65° oven overnight.

POLYURETHANE MICROFLUIDIC DEVICE FABRICATION

It is commonly known that although PDMS devices are easy to create, the flexibility of the material causes it to bend easily. Situations for which PDMS is not suitable include those in which high pressures are used (105) (greater than 1 Atm often cause bulging of channels) or those in which the ratio of width to height of a channel far surpasses 10. Although for these situations it is possible to create devices from silicon and glass, silicon-glass devices require substantially longer fabrication processing time (for drilling access holes, anodic bonding of glass to the wafer, and creating a chip holder to connect fluid lines when running experiments) and cost much more (cleaning and reusing the chips is possible, but these steps require substantially more time). For these reasons, we rely on photo-curable polyurethane to create some of our devices.

The specific photo-curable polyurethane we use is a thiolene based UV-adhesive, Norland Optical Adhesive NOA 81. The Young's modulus of this material is 1.4 GPa, which compares favorably to the relatively low Young's modulus of PDMS (360-870 kPa). We have found that it is possible to create channels using NOA 81 with a width to height ratio of 160 without collapsing, Figure 3.3. Additionally, NOA 81 is transparent and offers better resistance to solvents than PDMS. Compared to silicon-glass devices, prototyping using NOA 81 is much easier and faster with the creation of disposable chips of a large number of different designs (i.e. gap depths and angles) outside of a clean room. Similar approaches using UV-curable resins have already been reported, with microfluidic structures patterned by photolithography (106, 107) or molding techniques (108).

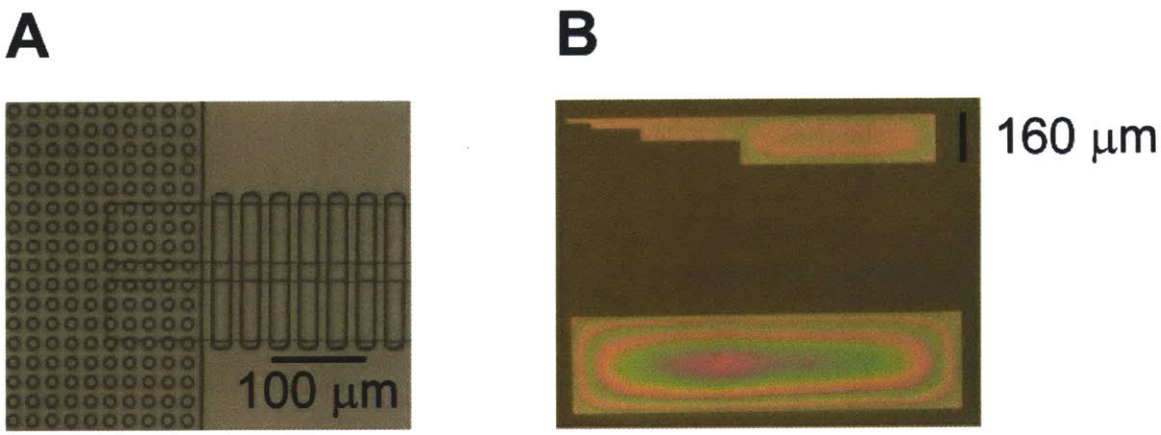

Figure 3.3. A. Picture from top of actual device near entrance **B.** Test structures indicating 2 μm deep features with aspect ratio of up to 2/320 did not collapse.

Because the devices we create using NOA 81 are typically very large (2 cm by 2 cm) and do not require feature sizes smaller than 10 μm, we use contact photolithography to create the devices. In contrast to the PDMS device manufacturing process, two castings are required to make polyurethane devices.

Steps for fabricating silicon mold for polyurethane microfluidic devices

1. Coat the 6" silicon wafer using the coater6 in the ICL.
2. Expose the wafers using the EV1 in the TRL.
3. Develop the wafers.
4. Etch the wafers using the STS2 in the TRL.
5. Remove the photoresist.
6. Coat the wafers with photoresist again. Because the etch depth of the first layer is around 1-3 μm, we coat the wafer with the thick resist, to a depth of 8-10 μm.
7. Repeat steps 2-5.

To create the PMDS mold, we follow steps 1-7 in "Steps for creating a PDMS device." After making the PDMS mold, we follow the steps below to make the actual NOA 81 device. These steps are illustrated in Figure 3.4.

Steps for creating a polyurethane device.

1. Punch holes in PDMS backing with a biopsy punch. The biopsy punch that was used in our process was a Miltex biopsy punch 1.5 mm in diameter. Be sure that there are adequate numbers of filtration pillars between the punched hole and the critical region of the device by spacing the punched holes sufficiently far from the connecting fluidic channels. After punching the hole, withdraw the biopsy punch. If the bored cylinder is removed from the punched hole, replace it by using the ejection button of the biopsy punch.
2. Use Scotch tape to remove dust and debris from the surface of the PDMS slab.
3. Expose surface of glass to humidified air and then wipe with KimWipe to remove dust and debris from the surface of the glass slide.
4. Put both PDMS and glass slide in the Harrick plasma cleaner/sterilizer for 2 minutes vacuum and 1 minute plasma exposure. Take the two parts out from the oxygen plasma.
5. Deposit 1 drop of NOA 81 on the patterned PDMS mold and apply pressure to the glass slide on the drop. Be careful to eliminate air bubbles from the NOA 81.
6. Deposit 1 drop of NOA 81 on the flat PDMS cover mold and push the PDMS backing onto the mold.
7. Put the two pieces on a transparent plastic tray and expose the two pieces to light from the Spectroline Ultraviolet Transilluminator for 80 seconds. The exposure time will be different for different transilluminators and as the transilluminator ages. This exposure should not be so

short as to result in NOA 81 that is uncured, but also not so long as to make the NOA 81 unable to bond to another NOA 81 surface.

8. Peel both pieces of the device from the PDMS molds. Because one side contacting the NOA 81 has been exposed to oxygen plasma, the NOA 81 will adhere to this side. Because NOA 81 does not cure in the presence of oxygen, post-UV NOA 81 contacting plasma-unexposed PDMS will not adhere.
9. Create reservoirs by removing the bored PDMS cylinders. This can be done by carefully pushing pins against the NOA 81 on top of the bored PDMS cylinders.
10. Delaminate the glass slide from the PDMS mold.
11. Bond the two pieces of the device together by carefully aligning the punched reservoirs to the patterned reservoir region. Then carefully apply pressure to the two pieces to bond the device.
12. Expose the bonded device to the Spectroline Ultraviolet Transilluminator for 10 minutes.
13. Wrap the device in aluminum foil and put it in the 65° oven overnight.

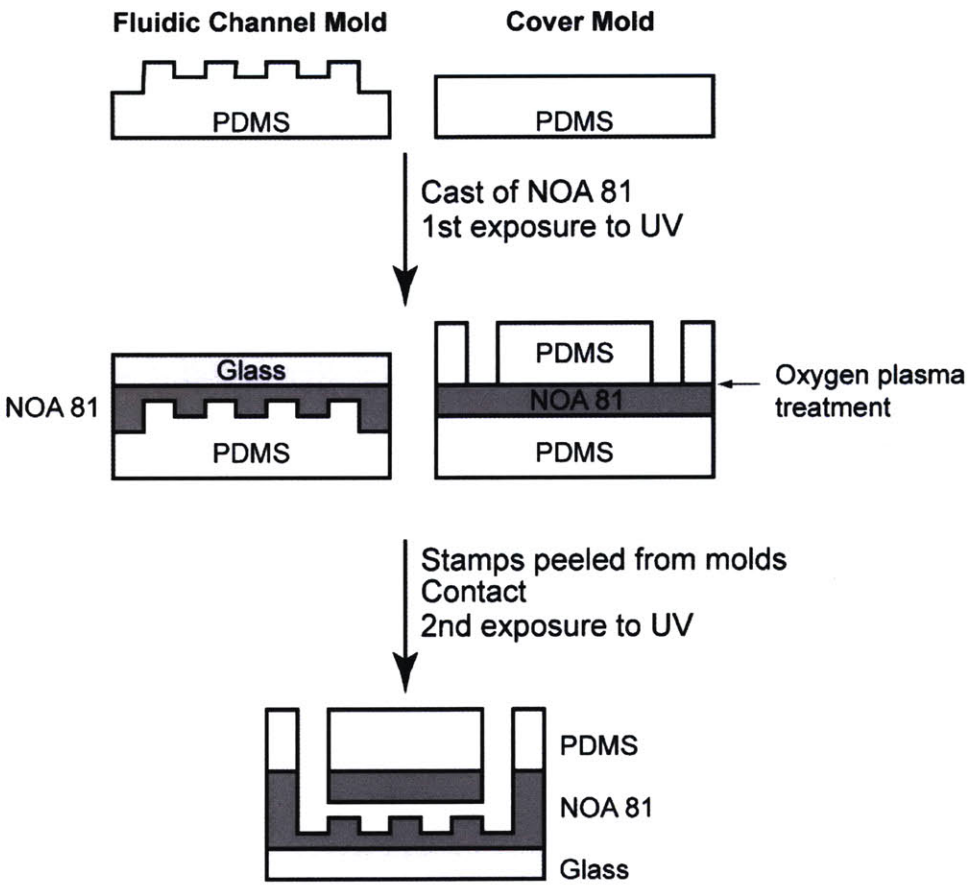

Figure 3.4. Fabrication details of polyurethane (NOA 81) devices cast from PDMS molds. This method of fabrication results in devices that are more rigid than devices with fluid channels made of only PDMS.

PARASITE CULTURE

P. falciparum was cultured in leukocyte-free human RBCs (Research Blood Components, Brighton, MA) under an atmosphere of 5% O_2, 5% CO_2 and 95% N_2, at 5% hematocrit in RPMI culture medium 1640 (Gibco Life Technologies) supplemented with 25 mM HEPES (Sigma), 200 mM hypoxanthyne (Sigma), 0.20% $NaHCO_3$ (Sigma) and 0.25% Albumax II (Gibco Life Technologies). Parasites

were synchronized by treatment with 5% sorbitol at least 12 hours before sample collection. The strain FUP-GFP, expressing a GFPmut2-neo fusion protein, was constructed by transfecting *P. falciparum* strain FUP with the plasmid pFGNr (Malaria Research and Reference Reagent Resource Center). Parasites expressing GFPm2:neo were selected with 350 mg/L G-418. Transfection was performed by the spontaneous DNA uptake method (109).

Biological Sample Preparation

PBS was mixed with 0.2 % w/v Pluronic F-108 (BASF, Mount Olive, NJ) and 1 % w/v Bovine Serum Albumin (BSA) (Sigma-Aldrich, St. Louis, MO) to prevent RBC adhesion to the device walls. This solution drawn into a syringe and then a 100 nm pore filter was attached to the syringe. The solution was then expelled and collected; clumps of undissolved BSA and other contaminants were thus removed.

For the fluorescent bead experiments, 200 nm FluoSpheres europium luminescent microspheres (Molecular Probes, Eugene, OR) diluted to a final concentration of 1.25×10^{-5} percent solids were used.

In experiments involving blood, 1 µl of whole blood (~50% hematocrit) was diluted in 100 µl of the PBS-pluronic-BSA solution for all of the experiments. In experiments involving parasites that express GFP, no further treatment was performed. These cells appear as shadows with a small fluorescent circle inside, as shown in Figure 1B.

In experiments involving healthy RBCs, 1 µl of whole blood (Research Blood Components, Brighton, MA), 1 µl of 50 µg/ml of Cell Tracker Orange (Invitrogen, Carlsbad, CA), and 98 µl of PBS were mixed with the indicated concentration of glutaraldehyde and allowed to sit for 30 minutes. The sample was then washed 3 times with the PBS-Pluronic-BSA solution.

In experiments involving reticulocytes, 1 µl of whole blood, 89 µl of the PBS-Pluronic-BSA solution, and 10 µl of 1 x 10^{-6} M thiazole orange were mixed and allowed to sit for 20 minutes before starting experiments. In our videos, reticulocytes appear as uniformly fluorescent cells under the GFP filter set, while mature RBCs appear as shadows.

In experiments involving late stage *P. falciparum*-infected RBCs that were not transfected to express GFP, cells were diluted in PBS containing 5 µg/ml Hoechst dye, 1% BSA w/v, and 2 g/L Pluronic F108 before injection into the device.

The PBS-Pluronic-BSA solution was pumped through the device for 30 minutes to coat the device walls with Pluronic and BSA. The RBC-PBS-Pluronic-BSA suspension was then injected into the device. Differences in pressure between the two reservoirs were generated hydrostatically by a difference in water column height. Liquid columns were connected by Tygon flexible tubing (ID 0.02 inches, OD 0.06 inches) to M925 LLTW probe needles to 60-ml plastic syringes lacking plungers to minimize surface tension effects.

A Hamamatsu Model C4742-80-12AG CCD camera (Hamamatsu Photonics, Japan), connected to an inverted epi-fluorescent Olympus IX71 microscope (Olympus, Center Valley, PA) was used for imaging. A CoolLED PE excitation system provided illumination. IPLab (Scanalytics, Rockville, MD) was used for video acquisition, resulting in an .avi file.

Cell Tracking Software

A custom-written MATLAB program tracked the RBCs and generated data used for velocity histograms. This program first estimates the median intensity of each pixel of the video by taking 10 evenly spaced frames of the video and finding the median. This frame will be the key frame to which all

frames are compared. For each frame of the video, the difference in intensity of each pixel is calculated between that frame and the key frame. Pixels greater in intensity or less in intensity than a given threshold are identified. Connected regions of identified pixels greater than a minimum size are then identified. The average intensity of each region is also calculated.

After identifying the RBCs in a particular frame, the program attempts to match each cell in the current frame to an existing cell within a certain distance from the previous frame. If this matching is not possible, this cell is identified as a new cell. The end result of this program is a video with RBCs identified by number (and/or intensity, infection state, size), Figure 3.5 and 3.6, and a spreadsheet of each RBC's velocity. We then review the output videos to check that cells were identified correctly.

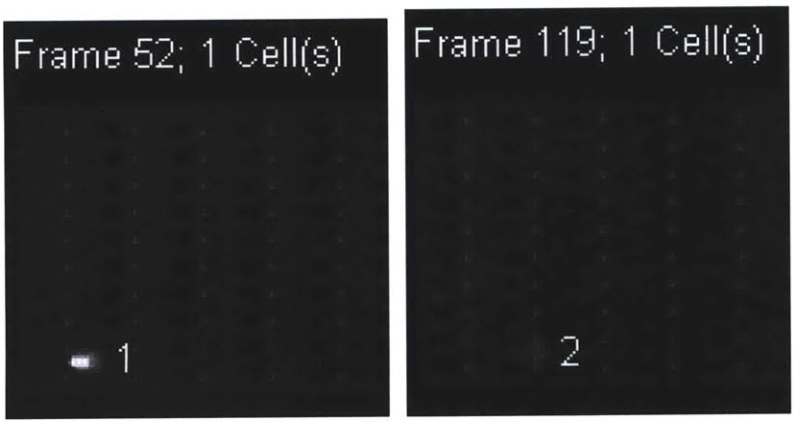

Figure 3.5. A late ring-stage infected RBC is identified in Frame 52. This cell has a brightly fluorescent parasite inside a faintly fluorescent RBC background. A healthy RBC is identified in Frame 119. The entire cell is faintly fluorescent.

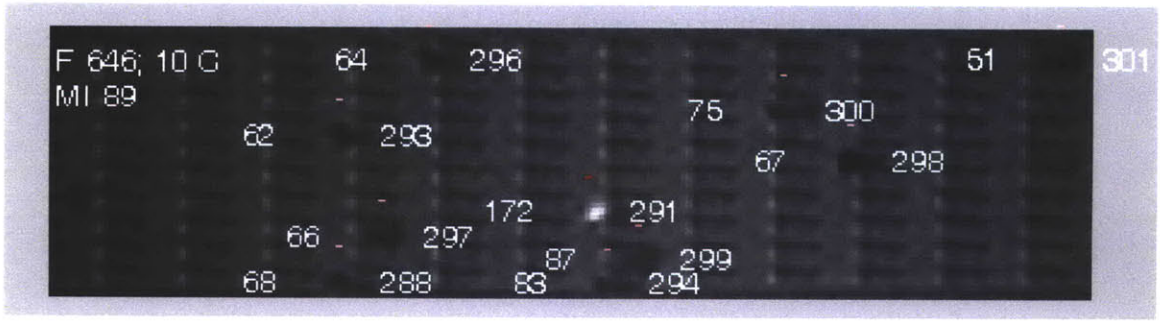

Figure 3.6. A more advanced version of the cell-tracking software. Shadows were identified as uninfected cells, and a bright dot surrounded by a dark region was identified as an infected cell. To the right of each cell is the cell identification number. On top of each cell is its identified infection status, red signifying infected and pink signifying uninfected. To the left of each cell is the instantaneous cell fluorescence intensity level. At the top left of the screen, F indicates the frame number, C is the number of cells on the screen, and MI is the mean intensity of the frame.

Simulation Setup

The Dissipative particle dynamics (DPD) (110) method was employed in simulations. In DPD, the fluid, solid walls, and RBC membrane are represented by collections of particles. The particles interact with each other through soft pair-wise forces: conservative, dissipative, and random force. The latter two form the DPD thermostat and are linked through the fluctuation-dissipation theorem. The viscosity of the DPD fluid can be varied by changing the functional form and magnitude of these forces (111). The solid walls were assembled from randomly distributed DPD particles whose positions were fixed during the simulations. In addition, bounce-back reflections were used to achieve no-slip conditions and prevent fluid particles from penetrating the walls (112). A portion of the microfluidic device with dimensions 200 by 120 by 4.2 microns containing 5 rows of pillars (10 pillars in each row) was modeled. The fluid region was bounded by four walls while periodic boundary conditions were used in the flow

direction. The RBC was simulated using 5000 DPD particles connected with links (113). The model took into account bending, in-plane shear energy, and membrane viscosity. The effect of membrane viscosity was modeled by adding frictional resistance to each link. The total area and volume were controlled through additional constraints. Parameters of the healthy cell model were derived from RBC spectrin network properties (113-115). In addition, membrane fluctuation measurements and optical tweezers experiments were used to define simulation parameters. Specifically, we required that the amplitude of thermal fluctuations of the membrane at rest to be within the range of experimental observations (116). We also required that the characteristic relaxation time of the RBC model in simulations to be equal to the experimentally measured value of 0.18 seconds. For *P. falciparum* infected cells, the membrane shear modulus and viscosity were increased 2.5 times (82). The malaria parasite was modeled as a rigid sphere, 2 microns in diameter. The RBC model was immersed into the DPD fluid. The membrane particles interacted with internal and external fluid particles through the DPD forces. The viscosity of the internal fluid was 9 times higher than external fluid viscosity. The flow was sustained by applying a body force to the DPD particles. By changing the direction of the body force, the motion of the cell through channels with converging and diverging pores was simulated using the same channel geometry.

Chapter 4

A MICROFABRICATED DEFORMABILITY-BASED FLOW CYTOMETER WITH APPLICATION TO MALARIA

Malaria resulting from *Plasmodium falciparum* infection is a major cause of human suffering and mortality. Red blood cell (RBC) deformability plays a major role in the pathogenesis of malaria. Here we introduce an automated microfabricated "deformability cytometer" that measures dynamic mechanical responses of 10^3–10^4 individual RBCs in a cell population. Fluorescence measurements of each RBC are simultaneously acquired, resulting in a population-based correlation between biochemical properties,

---

A substantial portion of this chapter is included in the following journal submission:
Bow H, Pivkin I, Diez-Silva M, Goldfless S, Dao M, Niles J, Suresh S, Han J (2010) A microfabricated deformability-based flow cytometer with application to malaria

such as cell surface markers and dynamic mechanical deformability. This device is especially applicable to heterogeneous cell populations. We demonstrate its ability to mechanically characterize a small number of *P. falciparum*-infected (ring stage) RBCs in a large population of healthy RBCs. Furthermore, we are able to infer quantitative mechanical properties of individual RBCs from the observed dynamic behavior through a dissipative particle dynamics (DPD) model. These methods collectively provide a systematic approach to characterize the biomechanical properties of cells in a high-throughput manner.

INTRODUCTION

RBC deformability may be pathologically altered due to inherited genetic disorders (e.g. sickle cell anemia and hereditary spherocytosis), and both non-infectious (5) and infectious (6) diseases. Decreased human RBC deformability is both a cause of and biomarker for disease states (1). Malaria, a disease threatening approximately 2.2 billion people globally, and causing about 250 million clinical episodes and 1 million deaths annually (117), is an important example of an infectious disease process that drastically decreases RBC deformability. The most virulent human malarial parasite, *Plasmodium falciparum*, invades and develops within RBCs, and transitions through morphologically-distinct ring, trophozoite and schizont stages during the 48-hour maturation period within the RBC (33). While ring stage parasite-infected RBCs are less deformable than uninfected RBCs by only several-fold, late (trophozoite and schizont) stage parasite-infected RBCs are stiffer by a factor of up to 50 or more (6, 118).

Altered RBC deformability has important implications for disease pathophysiology. In traversing a blood capillary, the biconcave disc-shaped RBC must deform dramatically, as its unconstrained diameter exceeds that of a capillary. The reticuloendothelial system (RES) plays an important role in

eliminating parasite-infected RBCs from the circulation, and achieves this in part by sensing increases in RBC membrane rigidity (119). While the RES can efficiently deplete rigid late stage parasite infected RBCs from the circulation, the less rigid ring-stage-parasite infected RBCs are inefficiently removed (119). Thus, ring but not late stage parasite infected RBCs can be found in the peripheral circulation and measured for diagnostic purposes. Additionally, increased stiffness of late stage parasite infected RBCs, together with their enhanced adherence to endothelial cells, leads to their sequestration in the microvasculature of various organs. This is believed to be a key event precipitating potentially fatal malaria complications such as cerebral malaria (120). As such, characterizing parasite infected RBC deformability in a quantitatively rigorous manner will be important for better understanding the basic mechanisms underlying host clearance of parasite-infected RBCs and overall malaria pathophysiology. To this end, robust laboratory methods for quantitatively analyzing cell deformability in high throughput over heterogeneous cell populations and at low cost are desirable. Moreover, solutions that are readily translated into low-cost field diagnostic devices have the potential to further enable more efficient identification and treatment of individuals infected with *P. falciparum*.

Existing high-throughput methods for analyzing and quantifying cell deformability typically overlook cell population heterogeneity, and quantitative single-cell measurements are generally labor and skill-intensive. Furthermore, these methods are not readily translated into low-cost field diagnostic devices. While methods for studying cell biochemical characteristics (e.g. fluorescence-activated cell sorting (FACS)) are common, there is a paucity of techniques for investigating dynamic mechanical properties of cells. Commonly used methods for studying RBC deformability include filtration (121) and laser diffraction ellipsometry (122), which both measure bulk properties of a cell population. Therefore, these methods are not applicable in situations where the target cells constitute a small fraction of the

entire cell population, as would routinely be the case for minimally processed laboratory or clinical samples containing *P. falciparum*-infected RBCs.

Examining cells individually is an important strategy for characterizing inherently heterogeneous cell populations. Micropipette aspiration is one such method, and it has been applied to quantitatively study infected RBC deformability (123). However, it is laborious and limited in its throughput (124). More recent techniques include atomic force microscopy (125), optical stretching (126), and optical tweezers (82). Still, these methods are labor-intensive, expensive, and time-consuming. Furthermore, the relevance of these essentially static mechanical responses to what the RBC experiences in the circulation of a living organism may be limited.

Improvements in microfabrication techniques have enabled the creation of pores comparable in size to the smallest human capillaries (7). Studies using these devices are similar in nature to those involving micropipette aspiration (95, 96). However, less time and effort are required due to the well-controlled dimensions of the pores and the ability to simultaneously examine many cells. Furthermore, studies using microfabricated pores arguably simulate more closely the movement of individual RBCs through capillaries *in vivo*. Along these lines, a microfabricated device similar to a single micropipette aspirator has been created to examine the rigidity of *P. falciparum* infected RBCs (95). However, this single micropore design significantly limits overall throughput, and cell-cell interactions resulting in clogging at the pore inlet complicate obtaining quantitative and statistically significant data for cell populations.

Here we introduce an automated, microfabricated 'deformability cytometer' that measures dynamic mechanical responses of about 10^3-10^4 individual RBCs in a population. Fluorescence measurements on each RBC are simultaneously acquired, resulting in a population-based correlation

between biochemical properties (e.g. cell surface markers) and dynamic mechanical deformability. Significantly extending past work (7, 95), we propose a novel method relying on low Reynolds number fluid mechanics to evaluate the effect of entrance architecture on the sensitivity of cell deformability measurements. Custom software was written to automate video processing and facilitate easy analysis of thousands of RBCs, which is rarely accomplished in microfluidic systems. This higher throughput enabled us to measure statistically significant differences in deformability between two cell populations. Lastly, a Dissipative Particle Dynamics (DPD) model developed by Dr. Igor Pivkin in the research group of Professor Subra Suresh was built to translate the experimental measurements into quantitative data describing the mechanical properties of individual RBCs. This is the first study to systematically design and implement a microfluidic device capable of measuring cell deformability in high throughput and is sufficiently simple and inexpensive such that it can potentially be tailored for use with many different cell types and used in field diagnostic applications.

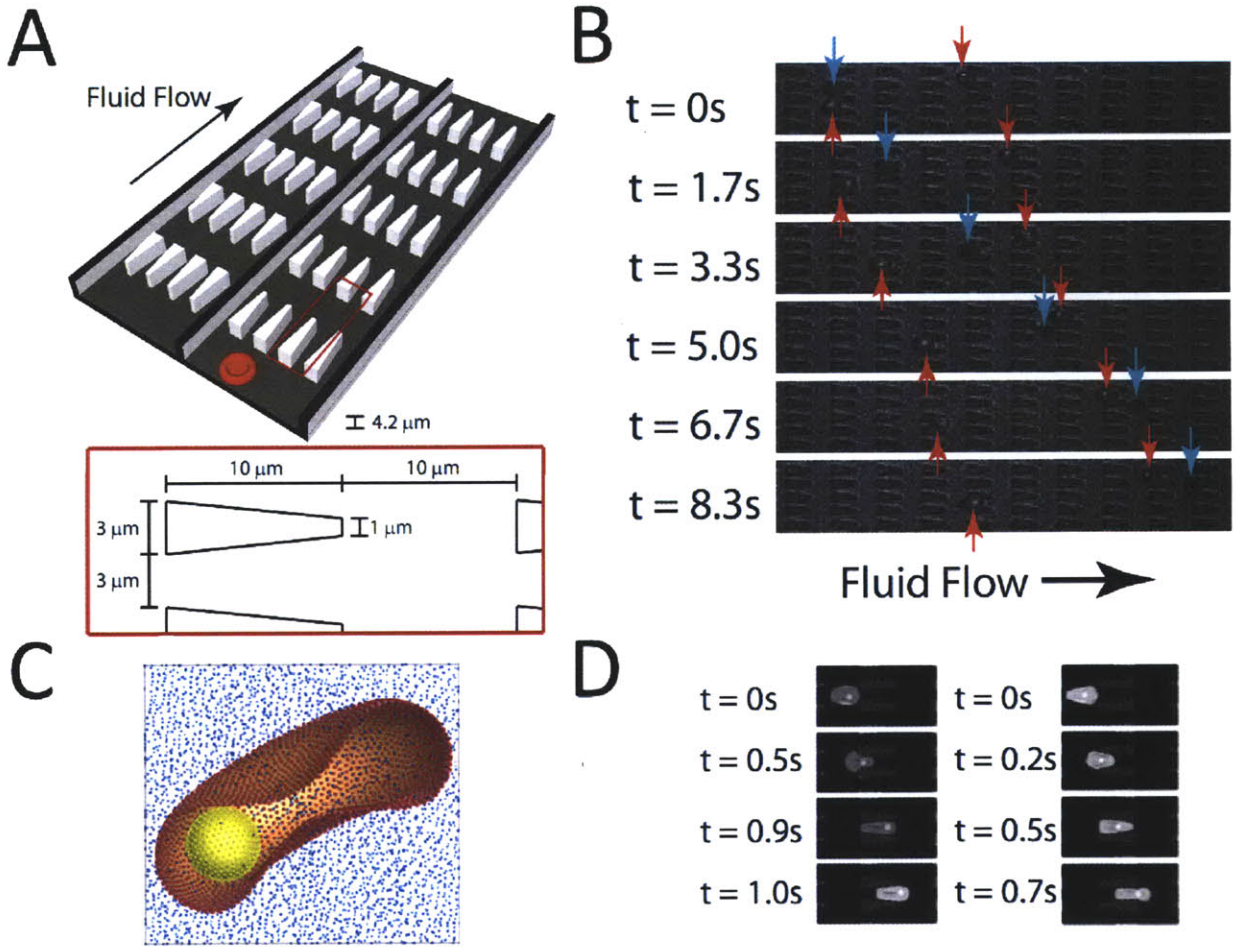

Figure 4.1. A. Illustration of device design; each channel of the actual device is 10 pores wide and 200 pores long. **B.** Experimental images of ring-stage *P. falciparum*-infected (red arrows) and uninfected (blue arrows) RBCs in the channels at a pressure gradient of 0.24 Pa/μm. The small fluorescent dot inside the infected cell is the GFP-transfected parasite. At 8.3 s, it is clear that the uninfected cell moved about twice as far as each infected cell. **C.** The computational RBC model consists of 5000 particles connected with links. The *P. falciparum* parasite is modeled as a rigid sphere inside the cell. **D.** DPD simulation images of *P. falciparum* -infected RBCs traveling in channels of converging (left) and diverging (right) pore geometry at 0.48 Pa/μm.

RESULTS

Our device design involves periodically spaced, triangle-shaped pillars. The gaps between these pillars result in well-controlled constrictions for RBCs to pass. The height of the device was set to 4.2 μm to force RBCs to assume a flat orientation before entering each constriction. This height, in addition to filters at the reservoirs, prevents white blood cells from entering the device, permitting diluted whole blood to be used directly. In our experiments, the concentration of RBCs is sufficiently low such that there is minimal interaction between cells and that transit times are independent. The constrictions in parallel across the width of the channel allow higher throughput, and the constrictions in series along the length of the channel enable repeated measurements of the same cell, increasing precision. Figure 4.1A and B illustrate the device design and demonstrate infected and uninfected RBCs moving at different velocities.

In past studies involving microfabricated pores, there has not been a determined effort to examine the influence of the pore shape on the ability of a cell to enter. For example, some studies use 90-degree angles for the walls of the pores (7), while others use angled or curved entrances (95, 96). In addition, most previous studies rely on the passage of many cells through a single pore, rendering the device susceptible to clogging and other confounding factors during the critical trapping and escape process at the bottleneck. These differing shapes naturally leads to the question of whether the geometry of constriction affects the amount of force required for cell herniation and traversal for openings of the same eventual cross-sectional area. Given the complicated nature of a cell's deformation process through the pore, we believe it may be possible to determine an optimized geometry ideally suited for "deformability selection."

To address these questions, we built a device to compare pairs of pore entrance geometries (Figure 4.1A). In this device are two channels in parallel with pores of different rates of constriction. According to low Reynolds number laminar flow, the forward and backward flow velocities and resistances will be identical (127). When we introduce low concentrations of cells, we are able to simultaneously observe control and experiment in the same microscope field of view. The difference in velocity of cells moving in the two channels indicates the role that entrance effects play in cell deformation through the pores with different entrance geometries, as confounding effects caused by temperature (82), cell age (128), buffer conditions (89), pressure, and device variability are obviated.

CREEPING FLOW

For a Newtonian fluid of constant density and viscosity, the Navier-Stokes equation describes fluid motion, and the continuity equation describes conservation of mass.

$$\rho \frac{Dv}{Dt} = -\nabla \wp + \mu \nabla^2 v$$

$$\nabla \cdot v = 0$$

In these equations, ρ is the total mass density, D/Dt is the material derivative, v is the mass-average velocity, $\wp$ is the dynamic pressure, μ is the viscosity, and g is gravitational acceleration.

To make the equations dimensionless, we make the following substitutions:

$$\tilde{r} = \frac{r}{L}, \tilde{v} = \frac{v}{U}, \tilde{t} = \frac{t}{\tau}, \tilde{\wp} = \frac{\wp}{\Pi}, \tilde{\nabla} = L\nabla, \tilde{\nabla}^2 = L^2\nabla^2$$

Where L is the characteristic length, U is the characteristic velocity, τ is the characteristic time, and Π is the characteristic pressure. Then the Navier-Stokes and continuity equations become

$$Re\left(\frac{1}{Sr}\frac{\partial\tilde{v}}{\partial\tilde{t}}+\tilde{v}\cdot\tilde{\nabla}\tilde{v}\right)=-\left(\frac{\Pi L}{\mu U}\right)\tilde{\nabla}\tilde{\wp}+\tilde{\nabla}^2\tilde{v}$$

$$\tilde{\nabla}\cdot\tilde{v}=0$$

Where

$$Re\equiv\frac{UL\rho}{\mu}$$

And

$$Sr\equiv\frac{\tau U}{L}$$

When the Reynolds number approaches 0, the Navier-Stokes equations becomes

$$\nabla\wp=\mu\nabla^2 v$$

This equation is referred to as the Stokes equation and describes creeping flow. Essentially, the nonlinear inertial term in the Navier-Stokes equation is eliminated. Because both the Stokes and continuity differential equations are linear, several properties uniquely apply to creeping flow. Among the properties that are important in the context of our experiments are that drag on a body and its mirror image is equal and that streamlines in both situations are identical. These properties can be shown by the fact that if v and $\wp$ are solutions to the Stokes and continuity equations, $-v$ and $-\wp$ will also be solutions. More generally, the fluidic resistance and velocities in two parallel obstacle-filled channels with one channel the exact reverse of the other will be identical.

In the context of our experiments, the Reynolds number can be calculated using the following order-of-magnitude numbers: $U \sim 100\ \mu m/s$, $L \sim 10\ \mu m$, $\rho \sim 1 g/cm^3$, and $\mu \sim 10^{-3}$ Pa·s. Using these numbers, $Re \sim 10^{-3}$, which satisfies $Re << 1$ for creeping flow.

VERIFICATION OF INDISTINGUISHABLE FLUID VELOCITIES IN TWO CHANNELS

To verify indistinguishable fluidic resistance in, and flow rate through, the two parallel channels, we introduced 200 nm non-deformable polystyrene beads into the fluid to track velocity. In the range of pressures and fluid velocities that are relevant both physiologically and in our experiments, we found that there were no statistically significant differences in bead velocity through the channels, Figure 4.2. The spread in bead velocities is mostly attributable to non-constant fluid velocities across a cross section of the channel, due to the viscous nature of the fluid.

DPD simulations confirmed this result. The difference in fluid flow velocity was found to be less than 0.3%, confirming that the fluidic resistance does not depend on the orientation of the obstacles. Streamlines were also examined to confirm almost complete reversibility of the flow.

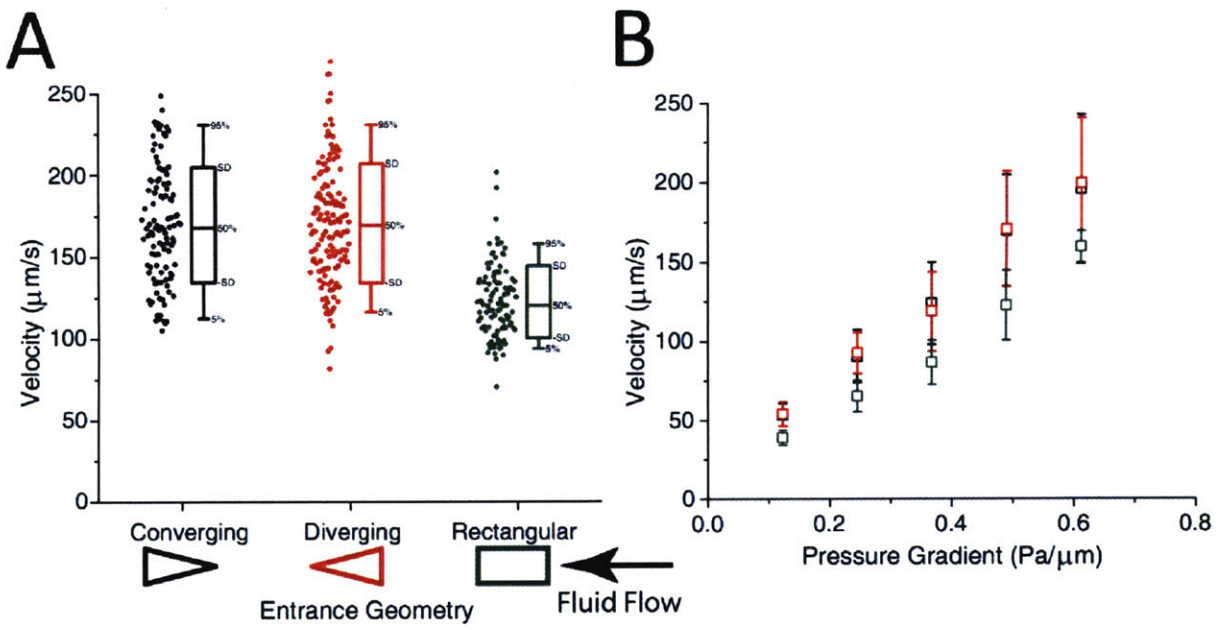

Figure 4.2. A. Velocity of individual 200-nm-diameter beads at a pressure difference of 0.49 Pa/μm. There is no statistically significant difference in the velocity of beads travelling through the converging and diverging geometries. The beads travelling through the channel with rectangular obstacles move slower on average. **B.** Velocity vs. Pressure for the different obstacle geometries.

Effect of Fluid Velocity and Obstacle Orientation on Velocity of RBCs

We performed all of the experiments using RBCs diluted to approximately 1% hematocrit. At high hematocrit, cell-cell interactions would dominate in the channels, as fluidic resistances and velocities would be affected by nearby cells. However, at very low hematocrit, experiments would take an unreasonably long time to run. We found that at ~1% hematocrit, cell-cell interactions were negligible and approximately 1000 cells could be analyzed in 10 minutes.

At all of the pressure gradients, RBCs exhibited faster velocity in the channel with converging entrance geometries, Figure 4.3. On average, RBCs traveled 25.5 % slower in the channels with diverging geometries.

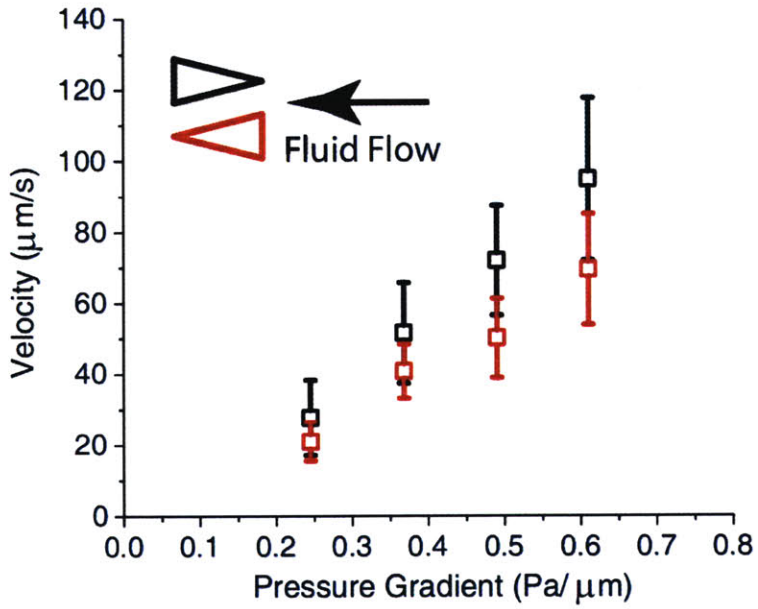

Figure 4.3. Velocity vs. pressure for RBCs moving through the two pore geometries. Error bars indicate standard deviation for each measurement.

Previous work focusing on the influence of entrance geometry on transit time has been mainly computational (129) and theoretical (130). However do not believe any experiments specifically addressing this topic have been performed. Here we first review Shirai's derivation of transit time and then discuss its significance to our experimental results.

The following derivation is based on that published by Shirai, Fujita, and Hayase (130) . When the cell is first constrained by the constriction, the axial component F_T of the reaction force balances the pressure-based cell driving force. ΔP is the driving pressure, and ΔP_{crit} is the minimum suction pressure

of a micropipette to aspirate the cell. R_{cell} is the radius of the cell. Other parameters are given graphically in Figure 4.4.

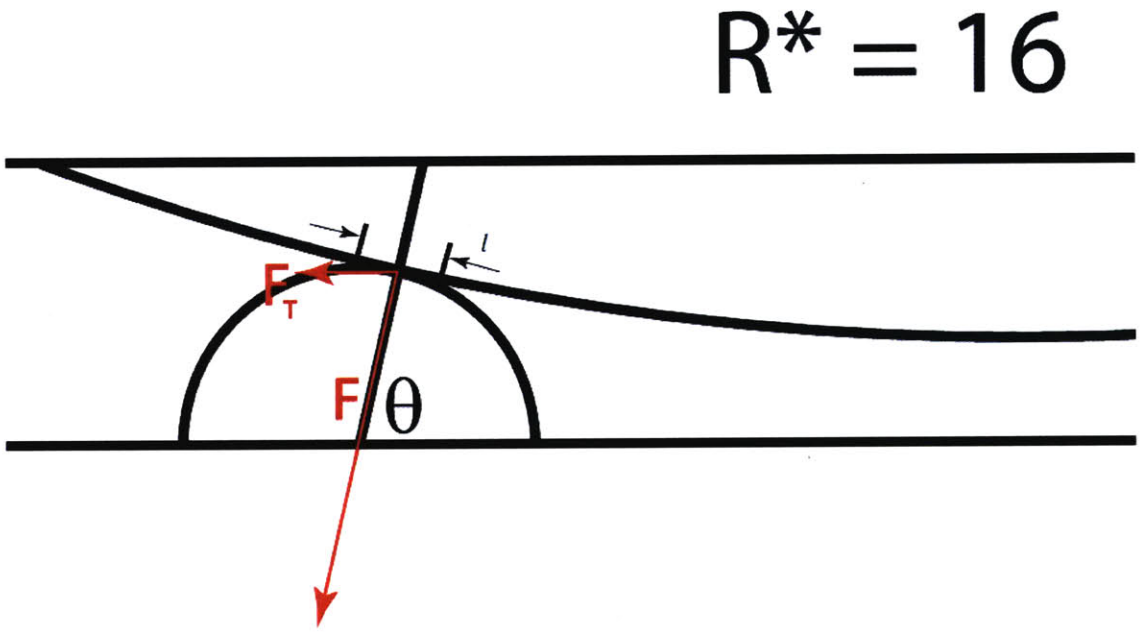

Figure 4.4. The model presented in Shirai, Fujita, and Hayase (130). R* is the normalized radius of curvature of the constriction, relative to the radius of the cell.

Then F_T is given by the following equation.

$$F_T = \pi(R_{Cell}sin\theta)^2(\Delta P - \Delta P_{crit})$$

The net reaction force is then

$$F = \pi(R_{Cell})^2 sin\theta tan\theta(\Delta P - \Delta P_{crit})$$

If the length of the contact area is l, the contact area A is then

$$A = 2\pi l R_{Cell} sin\theta$$

The reaction force per unit area τ' is then

$$\tau' = \frac{R_{Cell}}{2l} tan\theta(\Delta P - \Delta P_{crit})$$

When the shear modulus is negligible compared to the viscosity, the transit time of the cell t_0 is then

$$t_0 \propto \frac{1}{\tau'}$$

$$t_0 \propto \frac{1}{tan\theta}$$

where

$$tan\theta = \frac{R_{con} + R_{min}}{\sqrt{(R_{cell} - R_{min})(2R_{con} + R_{cell} + R_{min})}}$$

Assuming $R_{con} >> R_{min}$ and $R_{con} >> R_{cell}$,

$$t_0 \propto \frac{1}{\sqrt{R_{con}}}$$

Intuitively, the transit time for more sudden constrictions is longer, because the force from the wall acting on the cell is stopping the cell rather than compressing it.

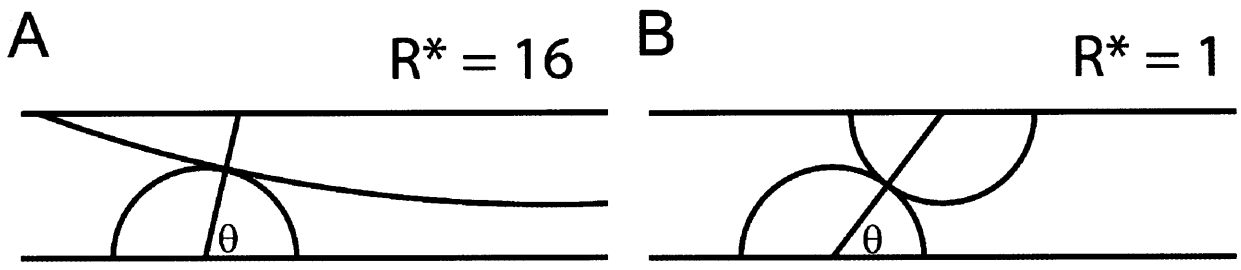

Figure 4.5. Two examples of cells encountering constrictions with the same minimum pore area but different rates of constriction. According to the theory presented, the cell encountering constriction A will exhibit transit time 4 times smaller than that of the cell encountering constriction B.

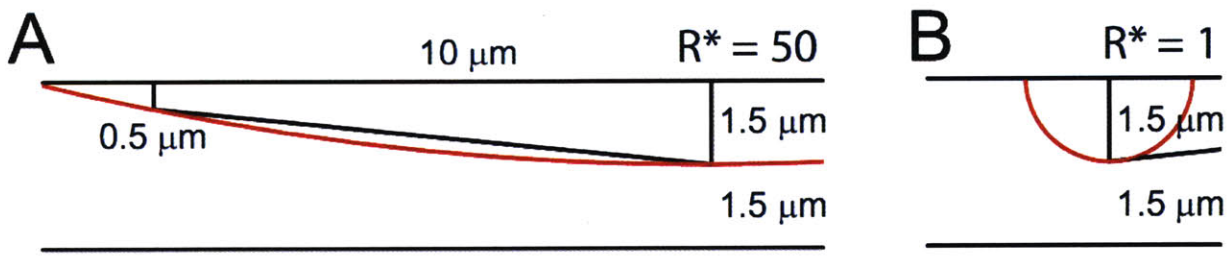

Figure 4.6. Approximations of the radius of curvature of the constrictions in our microfabricated devices. The black outlines represent the actual architecture of the entrance geometries used in our experiments. The red outlines represent arc-approximations to the actual geometries. For the converging geometry, we obtain a R* of 50 by matching two points of the trapezoid.

According to the approximations made in Figure 4.6, it would take approximately 7 times, or 600%, longer to enter the entrance geometry in Figure 4.6 B than it would for the entrance geometry in Figure 4.6 A. However in our experiments, it only takes 34% longer to enter the entrance geometry in Figure 4.6 B. Qualitatively the results are consistent, but quantitatively they are an order of magnitude different. Some reasons for this discrepancy are the approximations we used in creating the constriction radius of curvature, differences in the cytosol viscosity of the WBC compared to the WBC, the importance of membrane shear modulus for the RBC, circular symmetry in the model and the rectangular shapes of our experimental constrictions, and differences in shapes between WBCs and RBCs. Regardless of the quantitative differences in our calculations, our approach for examining the effects of entrance geometry on transit time is valid for neutrophils. Additional experiments with neutrophils are necessary to experimentally test the specific hypotheses posed in both the computation and theoretical models.

Effect of RBC Stiffness on Velocity through Different Constriction Geometries.

Treatment with increasing concentrations of glutaraldehyde for a limited period of time results in cells of increased stiffness (131). At concentrations of glutaraldehyde less than 0.002% and treatment for 30 minutes, more than 95% of the RBCs moved through the device. As we increased the glutaraldehyde concentration in the treatment solution, RBCs became progressively stiffer. As shown in Figure 4.7, there is an inverse correlation between the degree of artificial stiffening and the velocity of the RBCs through the channels. At a glutaraldehyde concentration greater than 0.003%, the majority of RBCs became immobilized toward the entrance of the device. These experiments demonstrate that decreased deformability alone can cause RBCs to travel with slower velocity in this device, as cell shape and size are preserved during glutaraldehyde treatment(131).

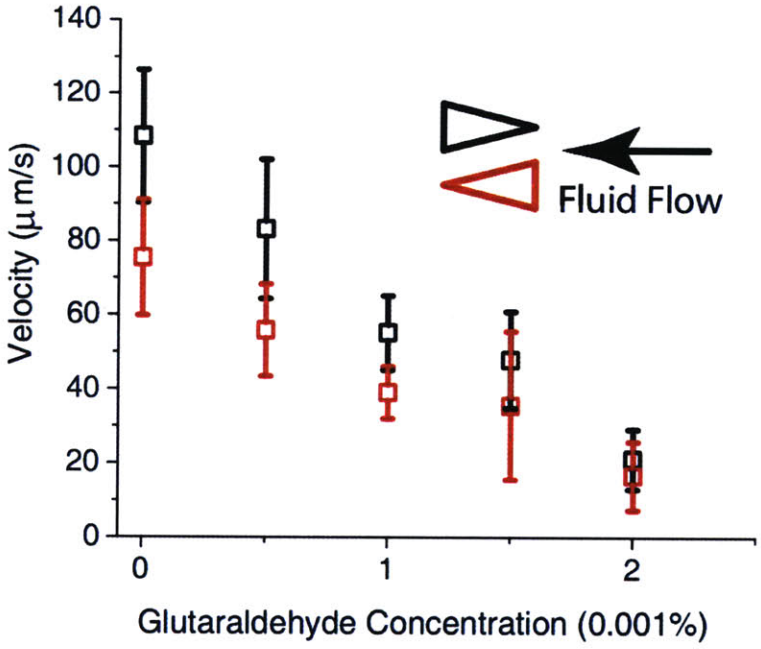

Figure 4.7. Velocity vs. glutaraldehyde concentration. RBCs were treated with the indicated concentration of glutaraldehyde for 30 minutes in PBS and then washed 3 times. The pressure difference/length was approximately 0.61 Pa/μm.

DEFORMABILITY OF LATE RING-STAGE *P. FALCIPARUM*-INFECTED RBCS

We performed this set of experiments using late ring-stage *P.falciparum*-infected RBCs that were transfected with a gene encoding green fluorescent protein (GFP) (Figure 4.8). It is believed that treatment with cell dyes influences the deformability of the cells (132). By using cells that express GFP, we overcome this concern. Our image analysis program tracked a shadow without a bright dot inside as an uninfected RBC and a shadow with a bright dot inside as an infected RBC. Around 1000 RBCs were tracked for each pressure gradient. The parasitemia in this set of experiments was around 1–2%. In all of these experiments, we observed negligible pitting, expulsion of the parasite from the RBC.

We determined that optimal pressure gradients for device operation are around 0.24 and 0.37 Pa/μm. For both the converging and diverging geometries, at pressure gradients of 0.24 and 0.37 Pa/μm, infected RBCs exhibited lower average velocities than uninfected RBCs. A p-value less than 0.01 at these pressure gradients leads us to conclude that the mean velocities for the infected and uninfected cells are different with statistical significance. These results are consistent with those involving micropipette aspiration (123). In those experiments, ring-stage infected RBCs required around 1.5–2 times the pressure and around 1.5 times the time to enter single pipette pores of around 3–3.5 μm. At higher pressures, mean velocities of infected and healthy RBCs moving through the device converged. At a pressure gradient of 0.48 Pa/μm, healthy and infected RBCs moved through the converging geometry at approximately the same velocity (about 50 μm/s).

In Figure 4.8D, we show that the diverging geometry is better able to accentuate differences in deformability between ring-stage infected cells and uninfected cells. The median velocity of infected

cells in the diverging geometry is 44% of that of the uninfected cells, compared to 80% in the converging geometry.

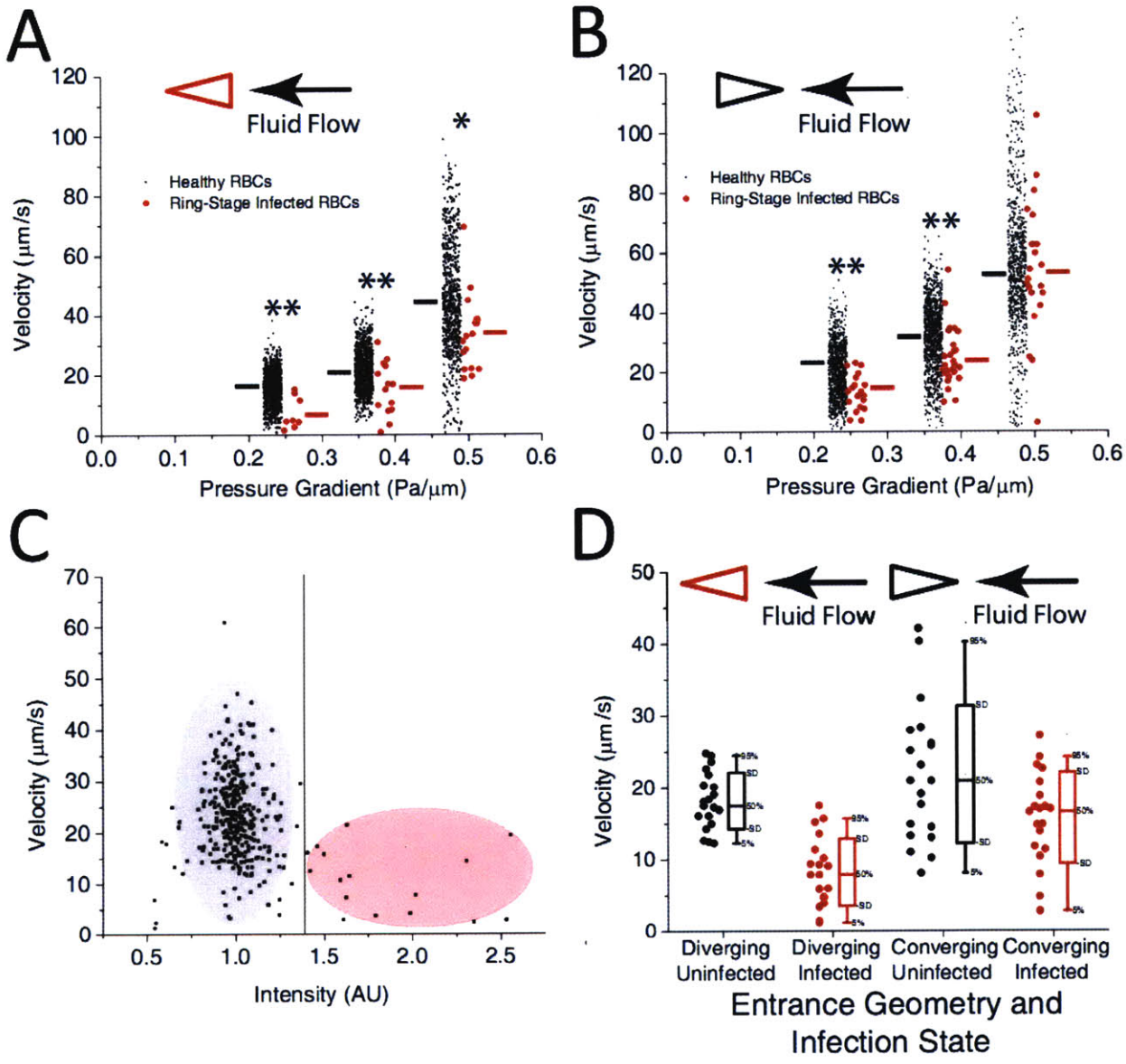

Figure 4.8. A. Velocity vs. pressure gradient for late ring-stage *P. falciparum*-infected RBCs. Approximately 1,000 RBCs were tracked for each geometry at each pressure gradient over a distance of 200 μm (10 constrictions). ** Indicates a *P*-value < 0.005 and * indicates a *P*-value < 0.05. Mean velocities are indicated by horizontal lines. **B.** An experiment run simultaneously using the same

population of RBCs in the converging pore geometry. **C.** FACS-like plot of velocity vs. intensity for ring-stage *P. falciparum* infected RBCs at a pressure gradient of 0.24 Pa/μm travelling in the converging geometry. Points to the right of the vertical line represent velocities of infected RBCs, while those to the left represent velocities of uninfected RBCs. The velocities of 381 RBCs were tracked. **D.** Velocity vs. infection state for RBCs infected with late ring-stage parasites at a pressure gradient of 0.24 Pa/μm. For each infected cell that was tracked, the next uninfected cell was tracked. Twenty cells were tracked for each measurement.

Deformability of RBCs Infected with Wild-Type and RESA Knock-Out Late Ring-Stage Parasites

RBCs infected with WT parasites exhibited a slower velocity compared to uninfected cells from the same culture, which is consistent with results presented in the previous section. The average velocity of WT infected cells is 58% that of uninfected cells in the same run, Figure 4.9.

RBCs infected with Resa-KO parasites also exhibited a slower velocity compared to uninfected cells from the same culture. The average velocity of KO infected cells is 78% that of uninfected cells in the same run. Although the KO-infected cells travel slower than the uninfected RBCs, the percentage difference in velocity is not as great compared to WT cells. The mean velocity of the uninfected cells in the WT sample was 23.3 μm/s and that for uninfected cells in the KO sample was 23.6 μm/s. The difference in average velocities is not statistically significant, supporting the validity of our claims. From these results, we may conclude that there exist factors in addition to RESA that cause malaria-infected RBCs to be stiffer than uninfected cells.

From 16 hours post-invasion, knob-like protrusions (~100 in diameter) appear at the surface of infected RBCs (33). These knobs are caused by the deposition and self-assembly of the KAHRP protein.

Because these proteins are deposited toward the end of the ring-stage and are known to significantly compromise the deformability of the infected RBCs, they may be the factor in addition to RESA that causes even the RESA-KO ring-stage cells to travel more slowly compared to healthy RBCs.

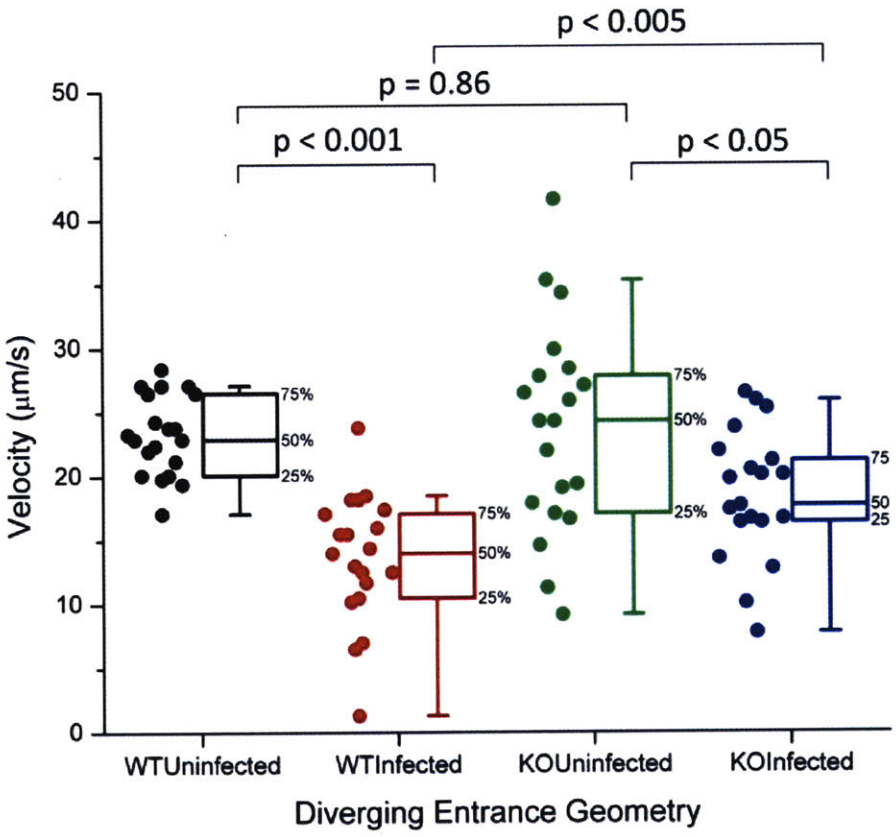

Figure 4.9. Deformability of Red Blood Cells infected with Wild-Type and Resa-Knock-Out Late Ring-Stage Parasites. Cells were stained with thiazole orange. For every infected cell that was identified and tracked for 200 μm, the next cell appearing in the field of view was also tracked.

DEFORMABILITY OF RETICULOCYTES CONTAINED IN WHOLE BLOOD

Reticulocytes are immature RBCs and typically account for around 1% of RBCs in whole blood. In contrast to mature RBCs, reticulocytes contain residual amounts of RNA. In our experiments, we diluted whole blood in phosphate-buffered saline (PBS) containing thiazole orange, a nucleic acid stain for reticulocytes. Then, the diluted blood was used directly in our device, without any further pre-treatment. A snapshot of a reticulocyte in our device is presented in Figure 4.10. White blood cells are removed at the inlet region of the device due to the 4.2 μm device height and filtration pillars and therefore do not interfere with the operation of the device.

Reticulocytes are believed to be larger than mature RBCs, on average having 44 μm^2 more surface area and 29 fL greater volume than mature RBCs (133). Additionally, reticulocytes are believed to be more rigid than mature RBCs. Reticulocytes take a substantially longer time to enter a single pore (134), and much higher pressure is necessary to bend the reticulocyte membrane and to force it to enter a pipette (132). The membrane shear elastic modulus of reticulocytes is almost double that of mature RBCs (135). In our experiments, reticulocytes exhibited velocity on average 67% that of mature RBCs in the diverging geometry, and 61% that of mature RBCs in the converging geometry (Figure 4.11).

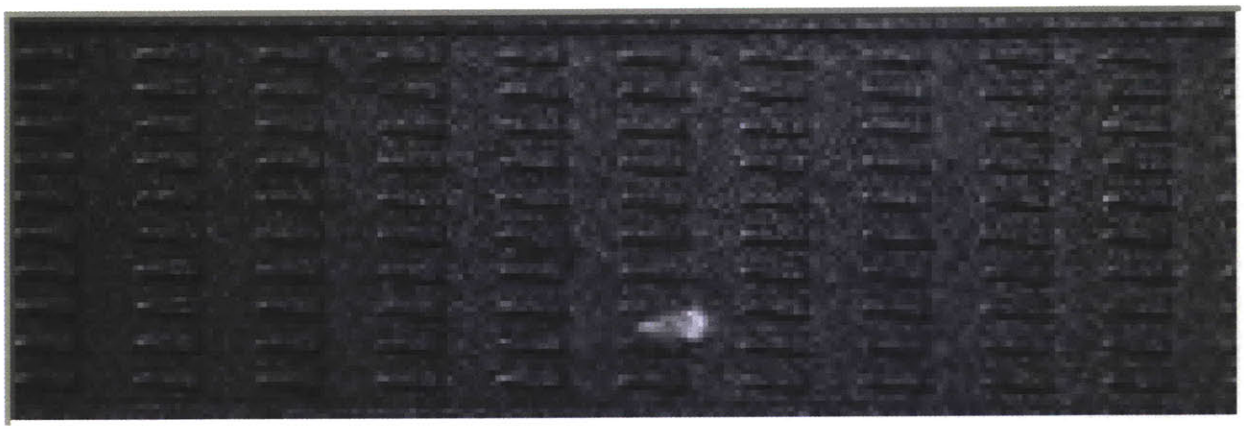

Figure 4.10. Reticulocyte and mature RBCs moving through the diverging geometry at a pressure gradient of 0.49 Pa/μm. The residual RNA inside the reticulocyte is stained, so the entire cell appears fluorescent; the mature RBCs appear as shadows.

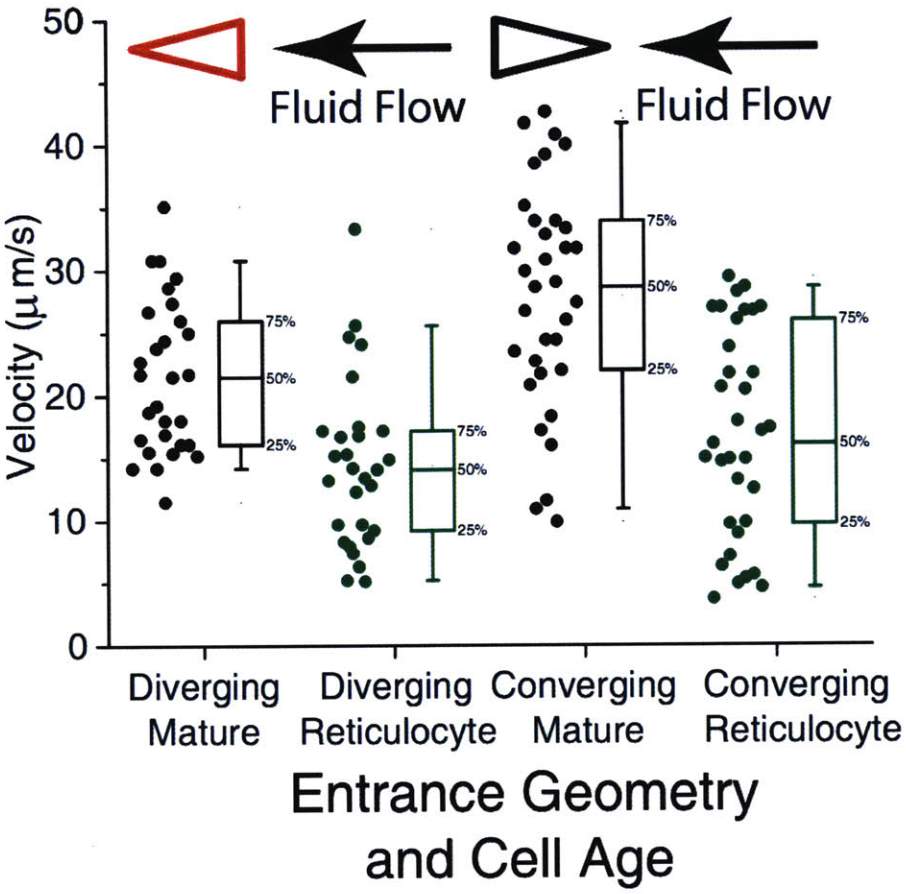

Figure 4.11. Velocity vs. cell maturation state. All experiments were run simultaneously, at a pressure gradient of 0.24 Pa/μm. Whole blood RBCs was stained for nucleic acid content with thiazole orange. Cells homogeneously fluorescesing under the GFP filter set were identified as reticulocytes. For every reticulocyte that was identified and tracked for 200 μm, the next cell appearing in the field of view was also tracked.

DISSIPATIVE PARTICLE DYNAMICS (DPD) SIMULATION OF CELL DEFORMATION THROUGH DIFFERENT CONSTRICTION GEOMETRIES

We performed three-dimensional simulations of healthy and malaria-infected cells using the DPD method. Infected cells were modeled with increased shear modulus and membrane viscosity values obtained from quantitative experimental measurements performed by recourse to optical tweezers stretching of the parasitized RBCs (82). We modeled the parasite as a rigid sphere, 2 microns in diameter (136), placed inside the cell (Figure 4.1C). Snapshots from simulations showing passage of an infected RBC through channels with converging and diverging pore geometries are shown in Figure 4.1D. Simulations were able to capture the effects of pore geometry and changes of RBC properties arising from parasitization quite well. Quantitative comparison of simulation results with experimental data for healthy and infected cell velocity as a function of applied pressure gradient is shown in Supplementary Figure 4.12A and B.

The model presented in this section was developed by Dr. Igor Pivkin in the research group of Professor Subra Suresh. Calibration of this model was based on results provided by David Quinn in the same group.

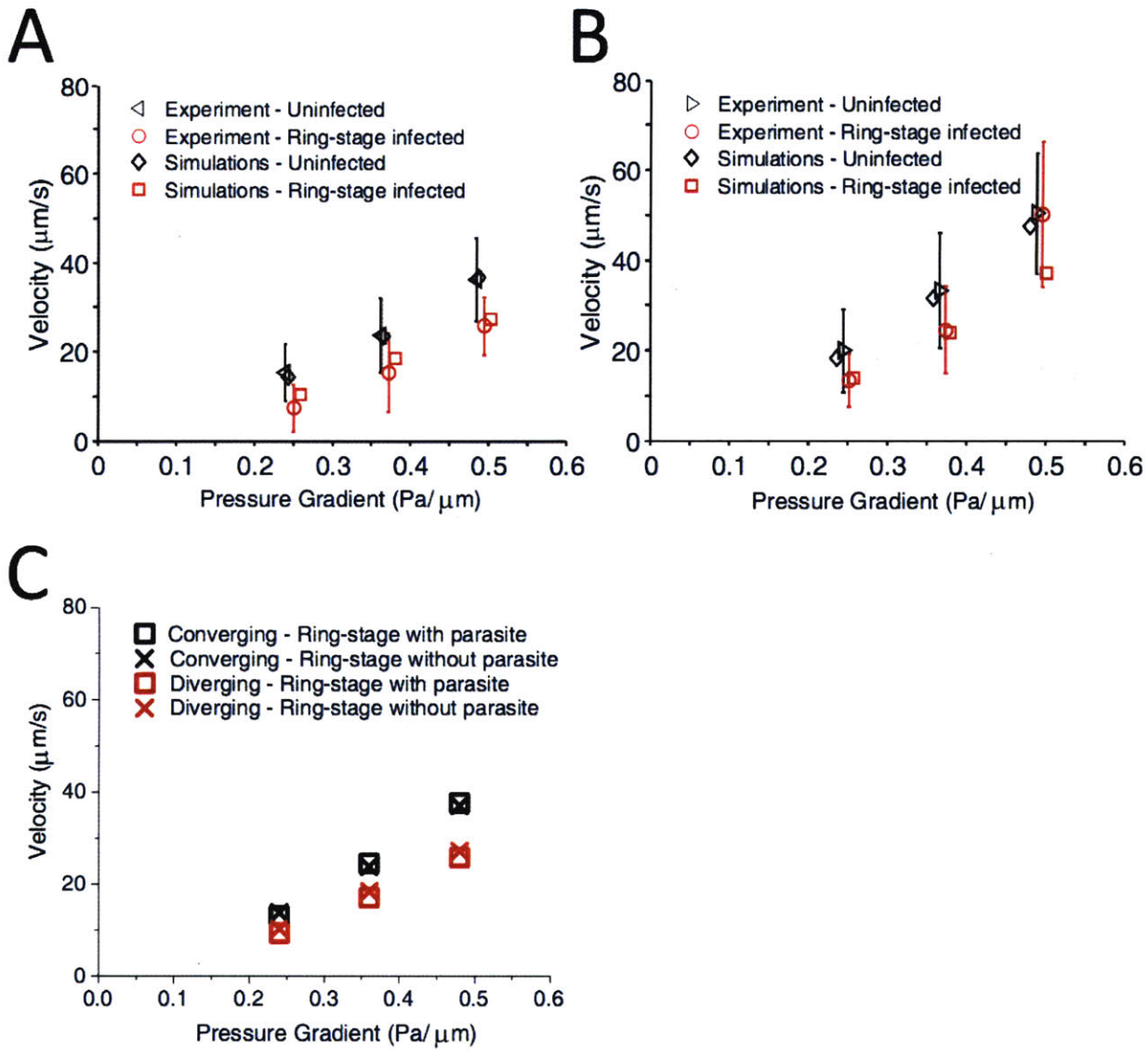

Figure 4.12. A. Velocity vs. pressure for healthy and ring-stage-infected RBCs in diverging pore geometry: comparison of simulation and experimental results. For experimental data, mean values are shown. The error bars correspond to one standard deviation. **B.** Velocity vs. pressure in converging pore geometry. **C.** Effect of intracellular parasite presence on the velocity of ring-stage infected cells. The parasite is modeled in simulations as a rigid sphere, 2 microns in diameter, placed inside the cell.

In order to evaluate contributions of individual mechanical properties of the cell to overall dynamic behavior, we performed additional simulations. The DPD model provides a unique opportunity to perform this analysis, since experimental evaluation of these contributions is laborious or impossible. We found that the flow behavior of infected RBCs in the device was not affected by the presence of the parasite inside the cell (Supplementary Figure 4.12C). Larger cells were found to travel with lower velocities; however, the velocity variation due to cell size was not significant (Figure 4.13A). Therefore, decrease of the traverse velocity of infected RBCs was mainly due to the increase of membrane shear modulus and/or membrane viscosity. Additional simulations were performed in which membrane shear modulus and membrane viscosity were varied independently of each other. The results showed that shear modulus was a dominant factor, while variation of membrane viscosity did not contribute significantly to the decrease of velocity of infected cells.

Increased membrane viscosity should increase the time it takes for a RBC to traverse an individual pore. However, it also slows down the recovery of RBC shape when the cell is traveling between pores, making it easier to enter the next pore. As a result, the particular design of our device lessens the dependence of the cell velocity on membrane viscosity (Figure 4.13B). Increased membrane shear modulus increases the transit time for an individual pore and also accelerates shape recovery, making it more difficult to enter the next pore. In Figure 4.13C we plot the variation of time it takes a cell to travel from one set of obstacles to the next at a pressure gradient of 0.24 Pa/μm as a function of membrane shear modulus. To a first approximation, the time increases linearly with shear modulus within the range considered in simulations. This simple dependence can be an advantage if the device is used to estimate the average shear modulus of a cell population based on the average velocity. For higher values of shear modulus, the transit time is likely to become a non-linear function; however,

stiffer cells (e.g. shear modulus greater than 30 μN/m, (82)) are presumably cleared by the spleen and therefore not typically present in free circulation.

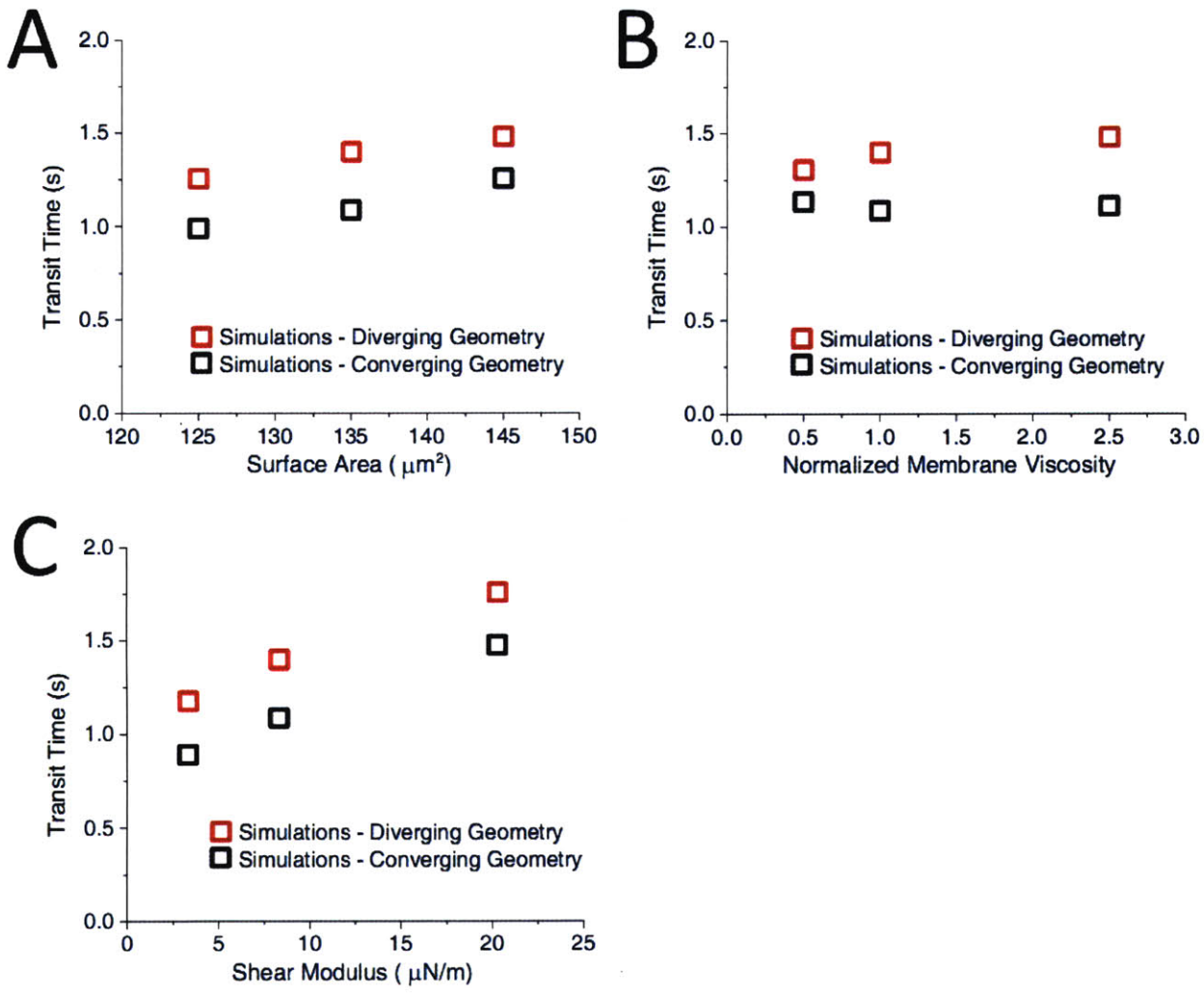

Figure 4.13. Dissipative particle dynamics (DPD) simulations. **A.** Effect of RBC size variation on transit time at a pressure gradient of 0.24 Pa/μm. Cells with surface area of 125, 135 and 145 μm^2 are modeled with corresponding volumes of 85, 94 and 103 μm^3. **B.** Effect of membrane viscosity variation on RBC transit time at a pressure gradient of 0.24 Pa/μm. The membrane viscosity is normalized by the healthy cell membrane viscosity value. **C.** RBC transit time vs. membrane shear modulus at 0.24 Pa/μm.

DISCUSSION

We have developed a versatile tool to measure cells' deformability in a quantitative, high-throughput manner. We have shown experimentally for the first time and by simulation that the entrance geometry of the constriction has a significant impact on RBC transit time, which has not been fully appreciated before. We have also shown experimentally that geometries with sharper corners are better able to discriminate differences in RBC deformability for a given pressure difference. Using this tool, we measured the dynamic deformability of ring-stage *P. falciparum*-infected RBCs quantitatively and statistically significantly. Using the advanced DPD modeling and simulation, it should be possible to further optimize the entrance geometries for better selectivity of infected versus uninfected RBCs.

Currently, there is some disagreement regarding what aspect of pore traversal causes the distribution in velocities. Brody et al. assert that pore entrance time is insignificant compared to kinetic friction between the RBC membrane and device walls for differences in RBC velocity (7). However, Secomb and Hsu claim that in theory, time taken for RBCs to enter pores would represent more than one half of the transit time for a single pore (137). In addition to the distribution in velocities, the effect of the entrance shape on traversal time has not been experimentally examined. Computer simulations have examined the entrance radius of curvature on the transit time of neutrophils and have concluded that a larger radius of curvature results in decreased transit time (129). However, to the best of our knowledge, no controlled experimental studies have been presented. In our experiments, we found that converging geometries resulted in RBCs exhibiting faster velocities on average when moving through the channels. We also found that an entrance geometry with a more abrupt transition from an open region to a pore is better at discerning differences in RBC deformability, as shown by our experiments with late ring-stage malaria-infected RBCs.

Whole blood is known to be a non-Newtonian fluid, with viscosity decreasing with shear rate. However, in the context of our experiments, this large-scale effect does not play a major role, since in our experiments the hematocrit was approximately 1%, while it is between 33% and 49% in whole blood. What is relevant in our experiments is the relaxation time of an individual RBC (approximately 0.2 seconds) (138). When an individual RBC does not have enough time to recover its original, undeformed shape before crossing from one constriction to the next, that RBC may assume a more favorable shape upon encountering the second constriction. This more favorable shape may then decrease the amount of time required for the RBC to deform and traverse the next pore than what would be predicted had the RBC assumed its original shape. Computer simulations by Shirai et al. of neutrophils passing through a succession of two cylindrically-symmetrical pores resulted in reduced transit time through the second pore under certain flow conditions (139). Groisman et al. applied this phenomenon in the context of polyacrylamide polymers to create microfluidic flux stabilizers (140). When the RBC relaxation time is substantially greater than the inter-pore travel time (e.g. at high pressure gradients), the ability of our device to discriminate differences in rigidity will be diminished.

We have clearly demonstrated the applicability of our deformability cytometer to malaria research, by identifying a smaller ring-stage infected RBC population out of a much larger number of healthy RBCs. In our device, we have not achieved complete separation between ring-stage *P. falciparum* infected RBCs and uninfected RBCs. This overlap in velocities is expected to be inherent in any mechanical method to examine the two populations of RBCs. The human spleen removes RBCs based on rigidity, among other factors. Because the spleen removes some of the older RBCs and not all of the ring-stage *P. falciparum*-infected RBCs, as demonstrated by Safeukui et al. (119), it can be inferred that the rigidities of ring-stage *P.falciparum* -infected RBCs and healthy RBCs must overlap to some extent. Also, the normal RBC population is inherently diverse, due to age and other factors (128). We

suspect that the large distribution of deformability for the healthy RBC population may come from this diversity. Since it is not likely that cell deformability alone (or cell surface marker information alone, obtained from fluorescent cytometry) can be used as a specific biomarker, it is crucial to combine multi-modal analysis of single cells for more precise cytometry, as we have demonstrated.

Common methods for assessing cell deformability involve bulk measurements (1). In the context of cultured or clinical malaria-infected RBCs, infected RBCs exist as a small minority in a large population of healthy RBCs. Therefore bulk measurements will not be able to offer the sensitivity required to measure the mechanical properties of only the infected RBCs. Furthermore, bulk measurements require relatively large volumes of precious cultured cells. Our device overcomes many of the limitations inherent in traditional single-cell measurements, such as low throughput and measurement artifacts that decrease physiological relevance. Additionally, diluted whole blood can be directly used in our device, without the need for centrifugation or other separation steps. It is straightforward to combine our device with other microfluidic methods to assess cell properties, such as the surface area-to-volume measurement parallel microchannels (74) and the oxygen perfusion-approach of Higgins et al. (141). In addition, the ability of our deformability cytometer to clearly distinguish reticulocytes in a large population of RBCs points to its potential for identifying the relatively less lethal *Plasmodium vivax* malaria (where the parasite predominantly invades reticulocytes) from *Plasmodium falciparum* malaria where the parasites can invade both the reticulocytes and more mature RBCs.

In *P. falciparum* malaria, only ring-stage infected RBCs are found in the circulation, while later-stage infected RBCs are either removed by the spleen (due to their increased stiffness) or adhere to the vascular endothelium (due to their cytoadherent properties). In fact, the subtle deformability increase of ring-stage infected RBCs and their ability to pass through the spleen are critical for *P. falciparum* survival in an infected host. One obvious and interesting application of this device would be screening for drug

compounds that increase ring-stage parasite infected RBC rigidity to improve splenic clearance, or decrease late-stage parasite infected RBC rigidity to prevent capillary blockage. We believe the microfluidic deformability-based flow cytometer will provide unprecedented opportunities in the areas of disease diagnostics and drug efficacy screening.

Chapter 5

CONTINUOUS-FLOW DEFORMABILITY-BASED SEPARATION

Change in cell stiffness is a characteristic of several blood cell diseases, such as sickle cell anemia (10), malaria (95), and leukemia (11). In humans, the spleen acts like a filter to remove these more rigid cells by pushing blood through slits between endothelial cells and removing cells that cannot pass. In this work, we create a microfluidic device that mimics the architecture of the spleen to achieve continuous-flow fractionation of cells based on their rigidity. We demonstrate successful operation of

---

This work presented in this chapter is based on the following publications:
Bow H, Abgrall P, & Han J (2008) Microfabricated slits in series: a simple platform to probe differences in cell deformability. *Proceedings of microTAS*, 1199-1201.
Bow H, *et al.* (2009) Continuous-flow deformability-based sorting of malaria-infected red blood cells. *Proceedings of microTAS*, 1219-1221.

this device by separating malaria-infected from normal, uninfected red blood cells (RBCs). Applications include disease diagnosis and sample preparation for downstream analysis.

INTRODUCTION: SPLEEN AS A MODEL BIOFILTER

One unique aspect of microfabrication technology is the ability to easily design and manufacture anisotropic structures. In contrast to traditional media, such as agarose gels and porous membranes, which are homogeneous and isotropic, anisotropic structures can preferentially force a subset of particles to go in one direction and the rest to go in another. The consequence of this anisotropy is the ability to continuously separate particles, as opposed to separating particles in batches. Advantages to continuous-flow separations include ease of collection of the fractionated subsets; speed, in that it is not necessary to wait until the slowest moving fraction passes the detection point before obtaining results; and lack of restrictions on minimal or maximum sample volume. Continuous-flow separation has been demonstrated using microfluidic devices for separating salt from water (142), proteins and sub-100 base pair DNA based on size and charge (143), bacterial chromosomes based on size(144), and blood cells based on size (80, 145). Here we create a microfluidic device that is able to separate red blood cells based on deformability.

Three factors influence RBC deformability: surface area to volume ratio, membrane viscoelasticity, and intracellular viscosity (28). Less deformable cells clog capillaries, causing hypoxia and tissue injury. The spleen, whose architecture has been compared to a wooden barrel with slits between the staves, typically removes these cells, Figure 5.1. All of the cells in blood are pushed through slits between endothelial cells; cells that are too rigid to pass are immobilized. Macrophages then phagocytose these cells, removing them from the circulation. In some situations, macrophages

phagocytose only a portion of the cell, allowing the rest of the cell to return to the circulation (e.g. warm autoimmune hemolytic anemia and pitting in malaria).

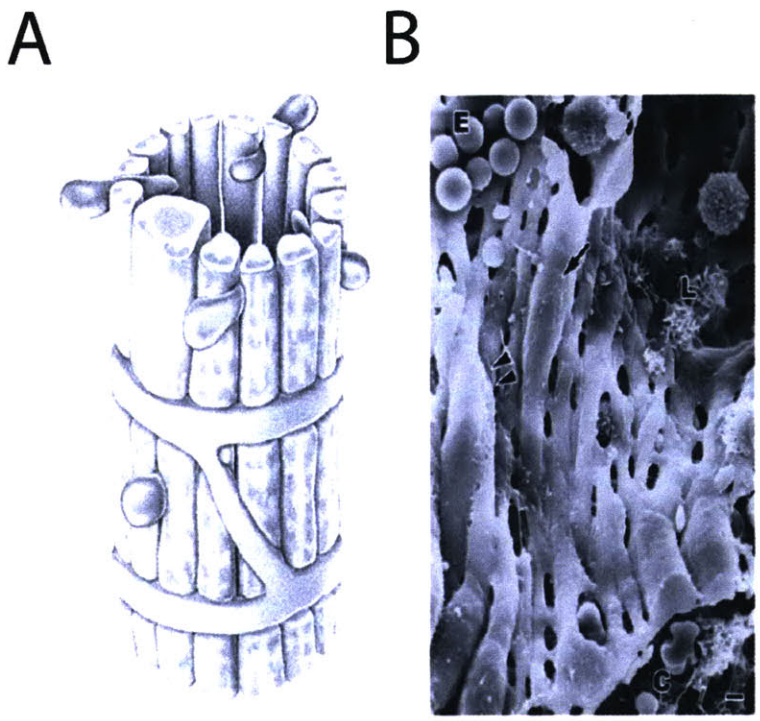

Figure 5.1. Spleen Architecture. **A.** Illustration of splenic slits. From (146). © Rockefeller University Press. Permission for reuse not necessary (non-commercial third party reuse). **B.** Scanning electron micrograph of spleen architecture. From (147). Permission for reuse granted by Springer.

Methods to separate cells have been surveyed in the background chapters of this thesis. Although many approaches to separating cells based on size have been presented, very few focus on the separation of cells of similar size but different deformability. These studies have mainly focused on the fabrication of square-like pores. For example, one study focused on the separation of fetal RBCs, which contain a nucleus, from the maternal circulation by using goose RBCs as a proxy (RBCs from avian and reptilian sources contain a nucleus) (103). However using these square pores, cells often get clogged at the frequent bifurcations of fluid flow, leading to loss of selectivity. Also, these studies often do not

focus specifically on deformability-based separation, and size is often a confounding factor (148). Other attempts have relied on optical stretching (85), which is time-consuming and high-cost.

Design of Deformability-Based Cell Separation Device

The gold standard for malaria detection is still the Giemsa staining method, which has a sensitivity of 50-100 parasites/μl. This microscope-based method is skill-intensive, mainly due to the existence of a large number of uninfected RBCs in the blood smear. In this situation, an efficient enrichment of target infected cells would be desirable to increase the diagnostic accuracy.

Here we present a device that is able to continuously enrich malaria-infected RBCs from a population of infected and uninfected RBCs based on deformability. We present a low-cost device that overcomes clogging-related issues, Figure 5.2. The device design is based on the idea that cells in blood must be able to pass through slits of a given width to remain in the circulation. We first present a device in which fluid flows perpendicular to periodically alternating slits and open areas. We demonstrate an inverse relationship between stiffness and velocity as RBCs are forced through the slits by a pressure gradient. We then introduce a device where fluid flows at an angle to periodically alternating shallow and deep regions. We first demonstrate this device's ability to separate artificially stiffened and untreated RBCs and then show that this device is able to separate malaria-infected RBCs and uninfected RBCs.

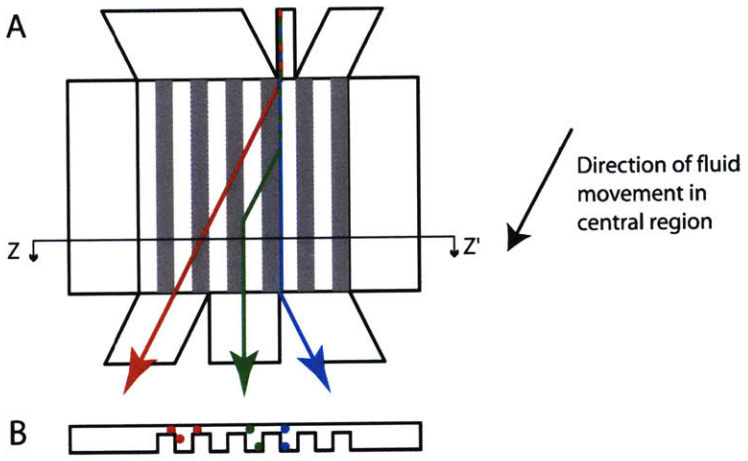

Figure 5.2. A. Top view of continuous-flow deformability-based separation device. The red line indicates the trajectory more deformable cells will take, as they are not hindered by the shallow regions. The blue line indicates the trajectory of rigid cells, which slide parallel to the constriction posed by the slit. **B.** Side-view of cross-section A-A'.

Results and Discussion

We first demonstrate RBCs of different deformability transit across slits at different velocities. We create a device shown in Figure 5.3 in which fluid flows perpendicular to a series of shallow and deep regions. RBCs are slightly larger than this slit size and must deform to traverse the slit. The period of the spacing is 30 μm in this device, and d_d is 4 μm. Similar to the experiments presented in the previous chapter, we artificially stiffen the RBCs by exposing them to various concentrations of glutaraldehyde.

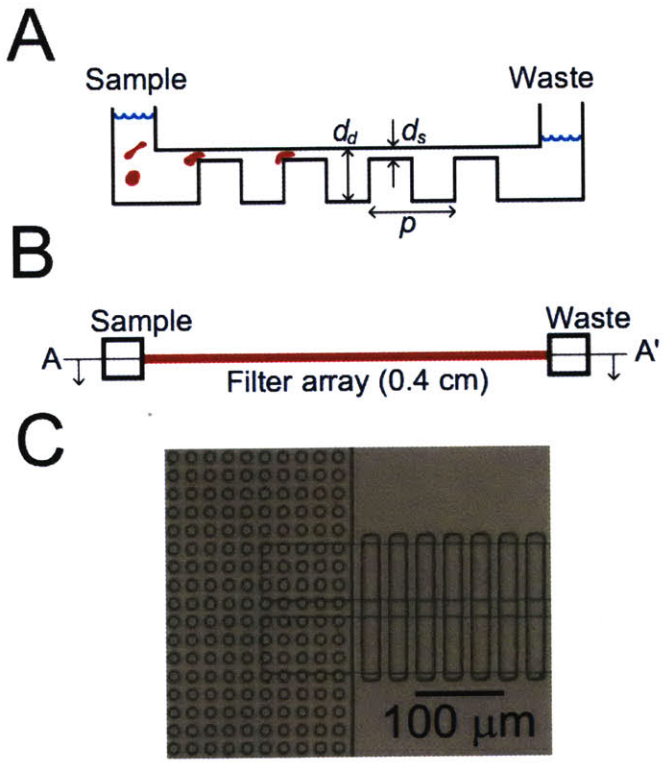

Figure 5.3. Illustration of 1-dimensional slits in series. **A.** Illustration of side-view of the device. The deep region depth of the device is d_d, the shallow region depth is d_s, and the period of the device is p. The fluid flow is caused by a hydrostatic pressure difference between the two reservoirs. **B.** Top-view of the device. **C.** Microscope image of the actual polyurethane device.

When the slit is too narrow, RBCs cannot pass through. This inability to pass through is mainly due to the surface area-to-volume constraint of the cell; the surface area is unable to expand for RBCs. Figure 5.4 presents a snapshot of this situation.

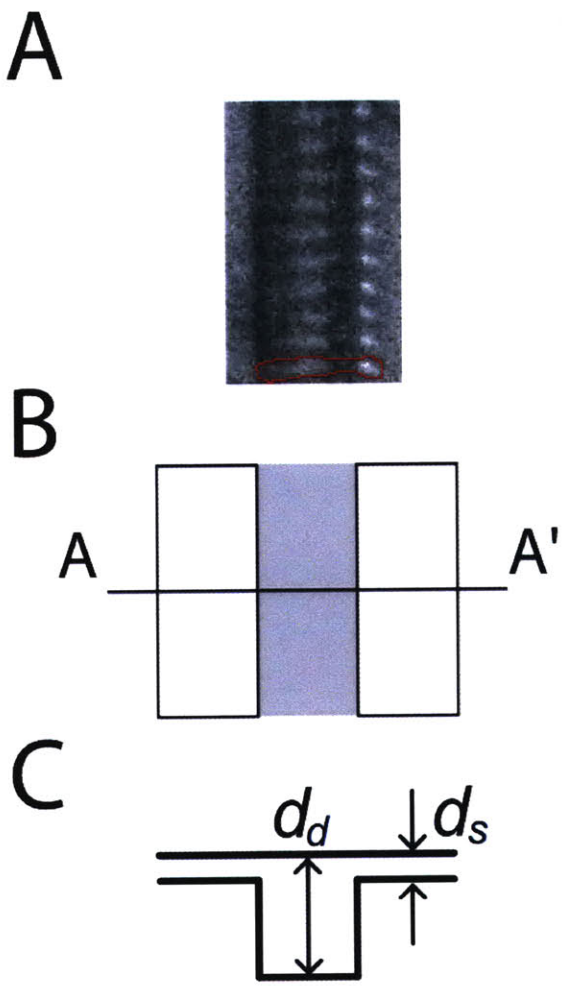

Figure 5.4. Untreated RBCs immobilized at the entrance of the slit. In this experiment d_s = 1 μm and the pressure gradient was 100 Pa/μm. **A.** RBCs aligned at the entrance of the slit. One of the cells is outlined in red. **B.** Top-view of part A. **C.** Side-view of part A and B; d_s = 1 μm and d_d = 4 μm.

Another situation when RBCS are unable to transit across a slit is when the RBCs are too stiff. When we treat the cells with glutaraldehyde at a higher concentration than 0.01% for 30 minutes, the cells are unable to pass through 2 μm slits. Figure 5.5 presents a snapshot of this situation.

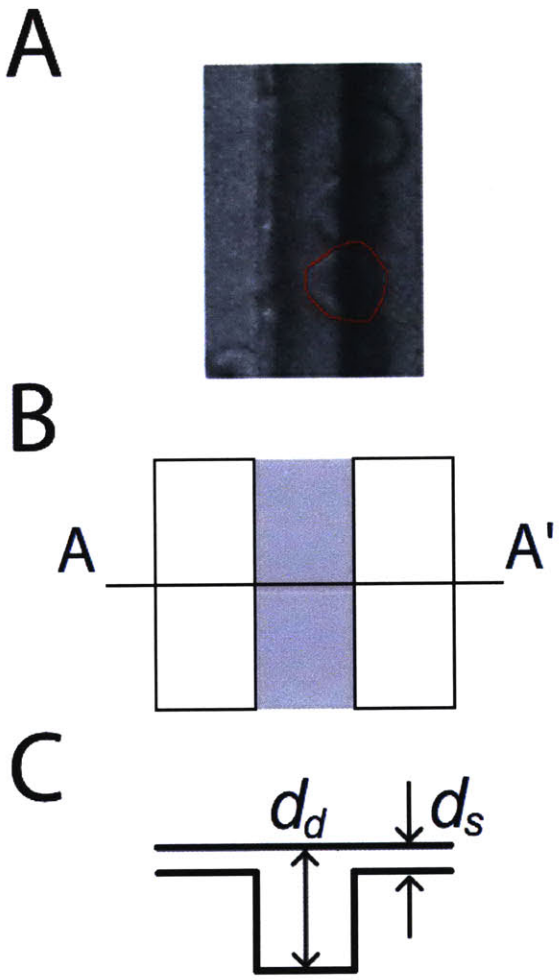

Figure 5.5. Artificially stiffened RBCs immobilized at the entrance of the slit. In this experiment d_s = 1 μm and the pressure gradient was 100 Pa/μm. RBCs were treated with 0.1% glutaraldehyde for 30 minutes. **A.** RBCs immobilized at the entrance of the slit. One of the cells is outlined in red. **B.** Top-view of part A. **C.** Side-view of part A and B; d_s = 2 μm and d_d = 4 μm.

When we treated RBCs with increasing concentrations of glutaraldehyde, we found that cells treated with higher concentrations of glutaraldehyde displayed slower velocity on average, Figure 5.6. Velocities of 0.001% GA-treated cells were within experimental error to untreated cells. The cells treated with 0.01% GA exhibited a velocity of 0 μm/s, as they were too rigid to pass through any of the slits. In this experimental situation, all of the cells were immobilized at the entrance of the device and caused massive clogging. This clogging is one disadvantage of devices in which fluid flows perpendicular to obstacles. At a concentration of 0.003 %, the cells were semi-rigid and showed decreased mobility compared to the untreated cells. Cell size was observed to be the same throughout the range of GA concentrations.

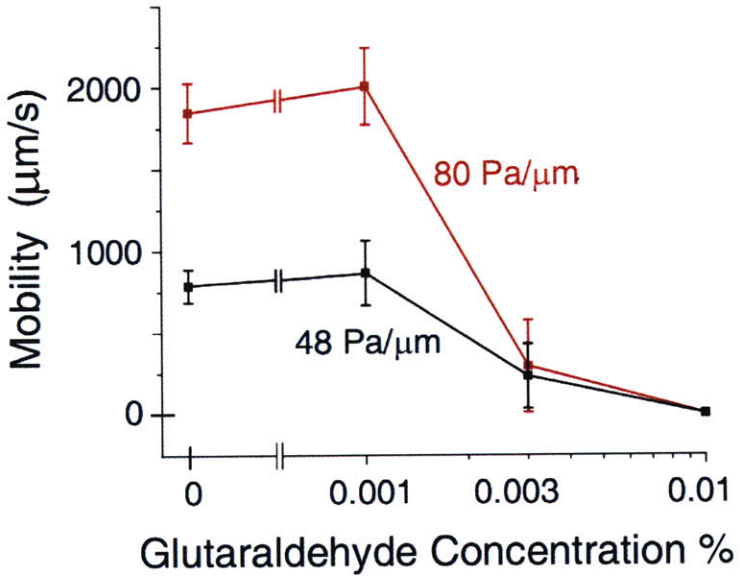

Figure 5.6. Mobility vs. glutaraldehyde concentration. Treatment with higher concentrations of glutaraldehyde results in stiffer cells, which display decreased mobility.

We first attempted to create a continuous-flow separation device with only one inlet and one outlet reservoir. The shallow region slits were positioned at an angle to the deep regions; the idea behind the design was that stiffer cells would encounter the slit and slide along it while more flexible cells would be unaffected by the presence of the slit. The device design is presented in Figure 5.7 panel A. Then if the direction of fluid flow were toward the top of the page, more rigid cells would be pushed to the sides of the channel, and less rigid cells would remain in the center of the channel.

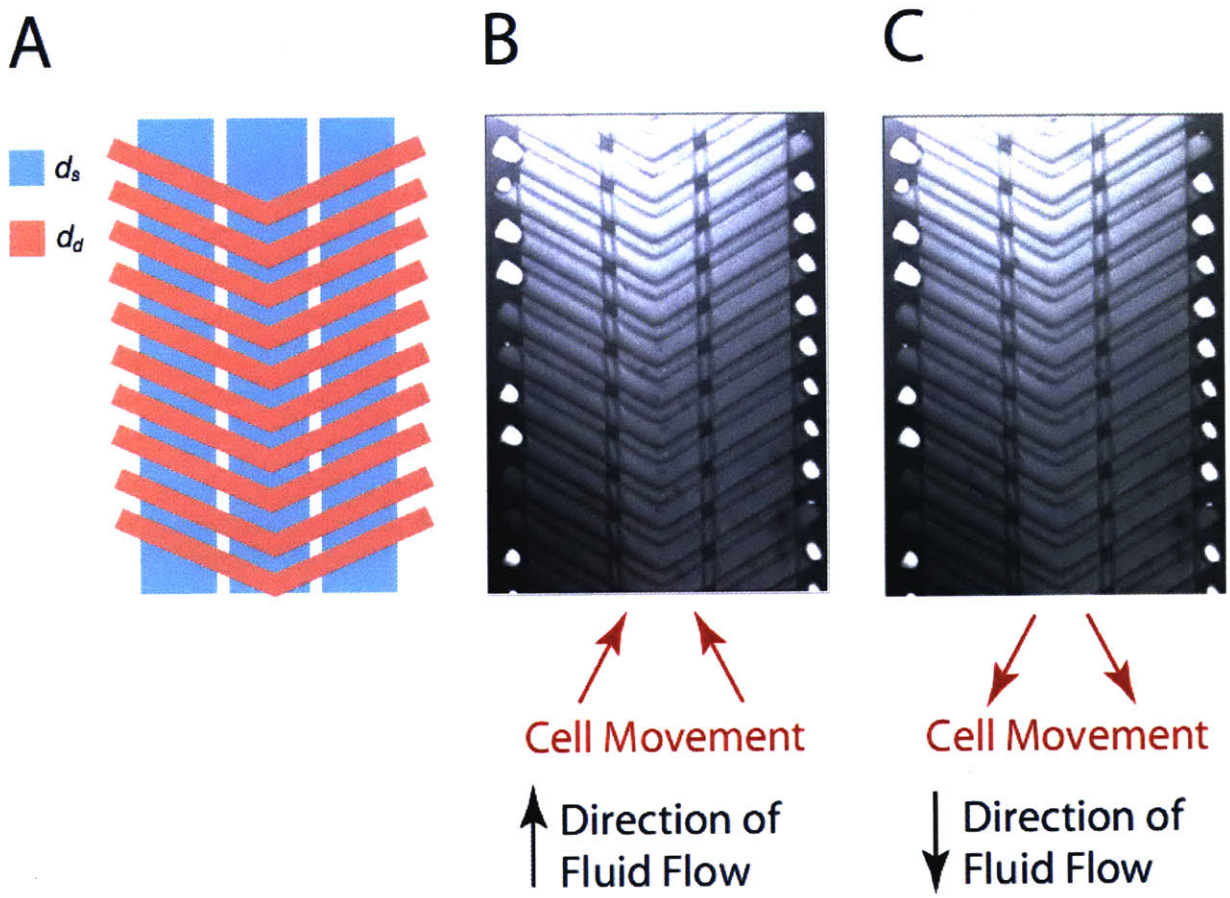

Figure 5.7. Herringbone device design. **A.** Illustration of the device design; shallow and deep regions are indicated. **B.** When fluid flows toward the top of the page, cells all converge toward the center of the channel, when they were uniformly distributed along the width of the channel at the entrance. **C.** When fluid flows toward the bottom of the page, cells converge toward the left and right edges of the channel.

The actual experimental result was contrary to our expectations. As explained in the figure caption, when fluid flows toward the top of the V-shaped deep regions, all of the cells converged toward the center of the channel. When we reversed the direction of fluid flow, all of the cells converged toward the left and right sides of the channel. This behavior is caused by the circulating fluid flow when both the left and right sides of the channel are closed. The presence of ridges in microchannels has been shown to be an effective cause of mixing (149). Other groups have also used herringbone-shaped deep regions to separate particles based on size (150, 151).

Based on our lack of results at achieving deformability-based separation in devices with closed side-channels, we concluded that it is necessary to keep the sides of the device open to prevent recirculating flow. We present the separation mechanism in Figure 5.8 A, and the details regarding device design in Figure 5.8 B. Essentially, less rigid cells will slide along the edges of the slits, while more rigid cells will travel in the direction of fluid flow. Because cells pass through multiple slits before escaping the device, the selectivity of the sorting would be increased. Also, clogging is potentially reduced due to the parallel filtration system design. At the end of the central region, less and more deformable cells will separate into separate streams that can be collected.

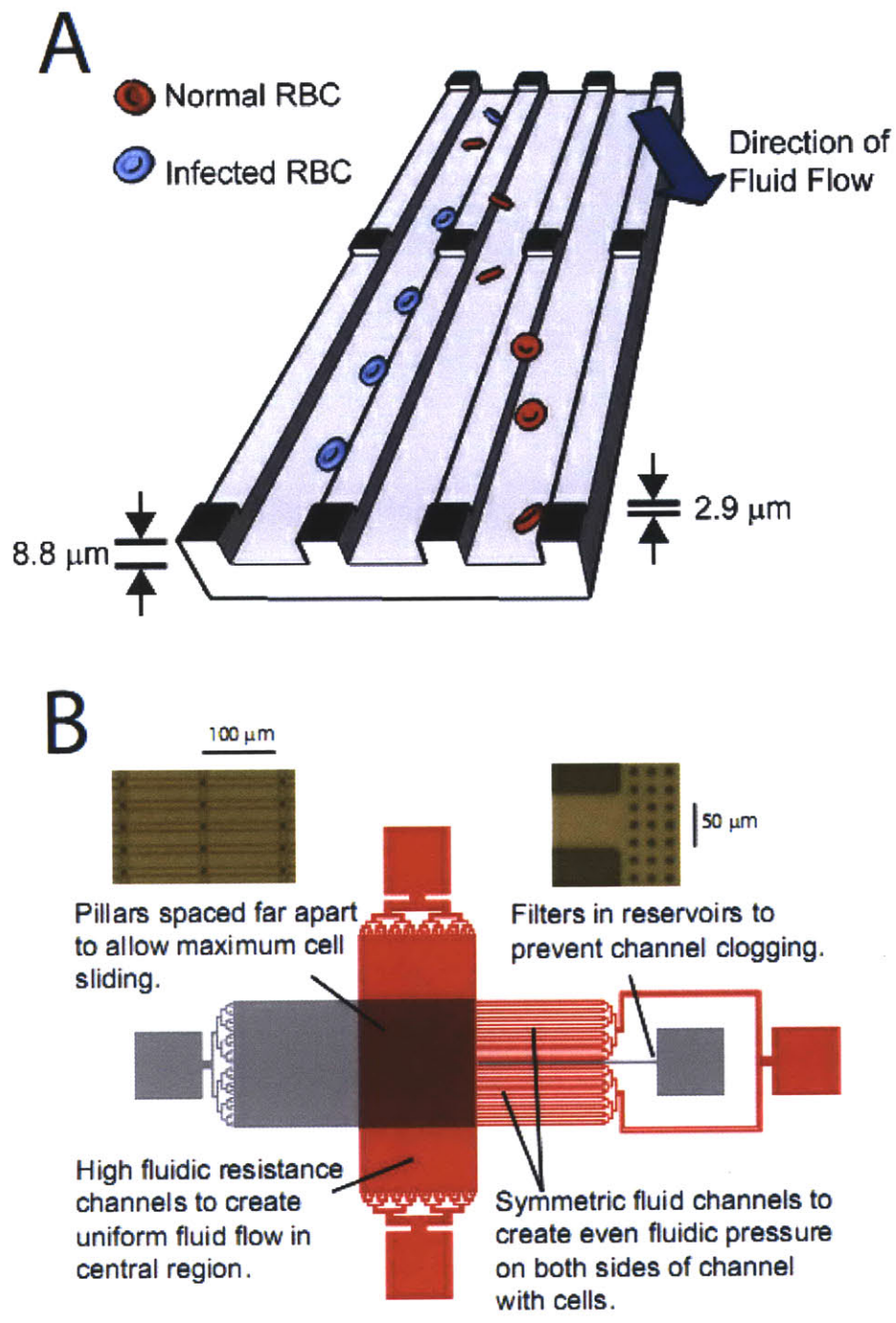

Figure 5.8. A. Illustration of device structure and operation. Fluid flows diagonally with respect to the slits. Infected RBCs slide along the edge of a slit, while normal RBCs follow the direction of fluid flow. **B.** Details regarding device architecture.

Within a normal, healthy RBC population, there will be a natural distribution of rigidity. RBCs circulate for around 120 days in humans and become more rigid during their lifetime. In our device, when we injected healthy RBCs, we saw that there was a distribution of angles that cells were deflected, Figure 5.9. The cause of this deflection may be that the surface area-to-volume constraints of some of the cells resulted in their inability to squeeze through slits of a particular width.

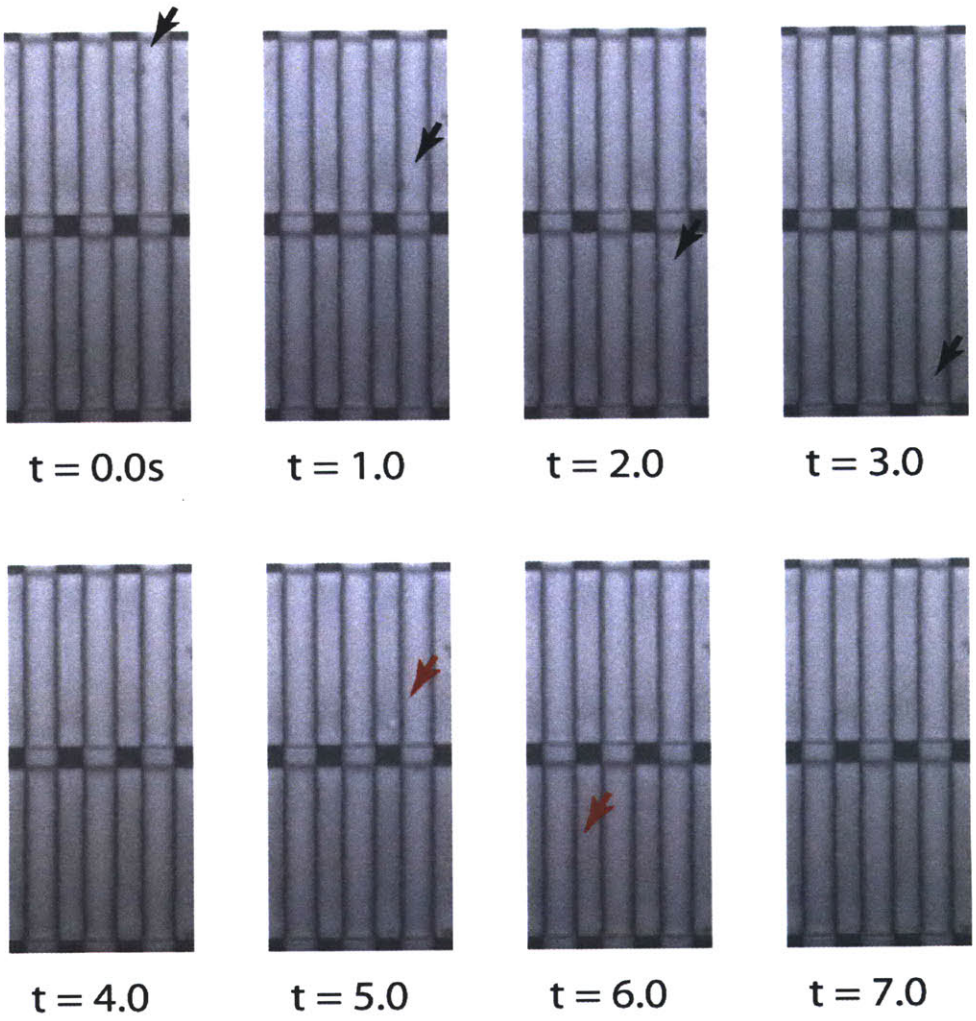

Figure 5.9. Two red blood cells deflected at different angles. From times 0.0 to 3.0s, the first red blood cells slides along the slit entrance. From 5.0 to 6.0s, the second red blood cell is able to enter the slit and travels at a different angle than the first red blood cell. Operating pressures in each of the reservoirs were maintained constant throughout these frames.

When we artificially stiffen RBCs using 0.003% glutaraldehyde, we see that cells deflect at different angles compared to untreated RBCs, Figure 5.10. Because cells are the same size and shape, the differences in deflection angle cannot be attributed to differences in surface area-to-volume ratio. The difference in rigidity is mainly attributed to increased membrane shear modulus and internal viscosity caused by the glutaraldehyde.

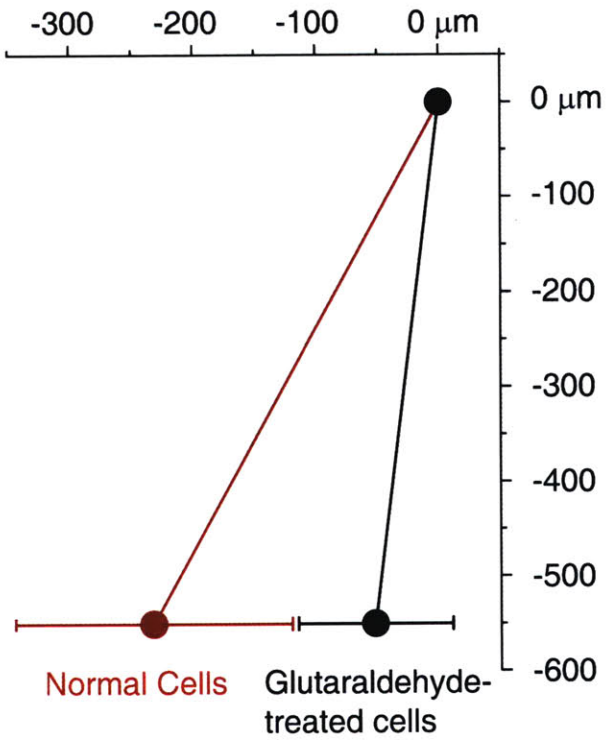

Figure 5.10. Mean and standard deviations of cell locations as they pass 550 μm. Glutaraldehyde-treated cells were immersed in a 0.003 % solution of glutaraldehyde in PBS for 30 minutes before being washed with PBS 3 times. Experiments were performed separately using two identical devices and the same pressures on respective reservoirs.

We separated schizont-stage malaria-infected RBCs from uninfected RBCs. Figure 5.11 A presents a snapshot from a video showing an infected cell sliding along the edge of a slit and uninfected cells following the direction of the fluid flow. Figure 5.11 B shows a three-second long sequence of superimposed video images. Distinct trajectories of normal and schizont RBCs are evident. The infected cell can be seen moving horizontally, while shadows of the uninfected cells can be seen moving diagonally.

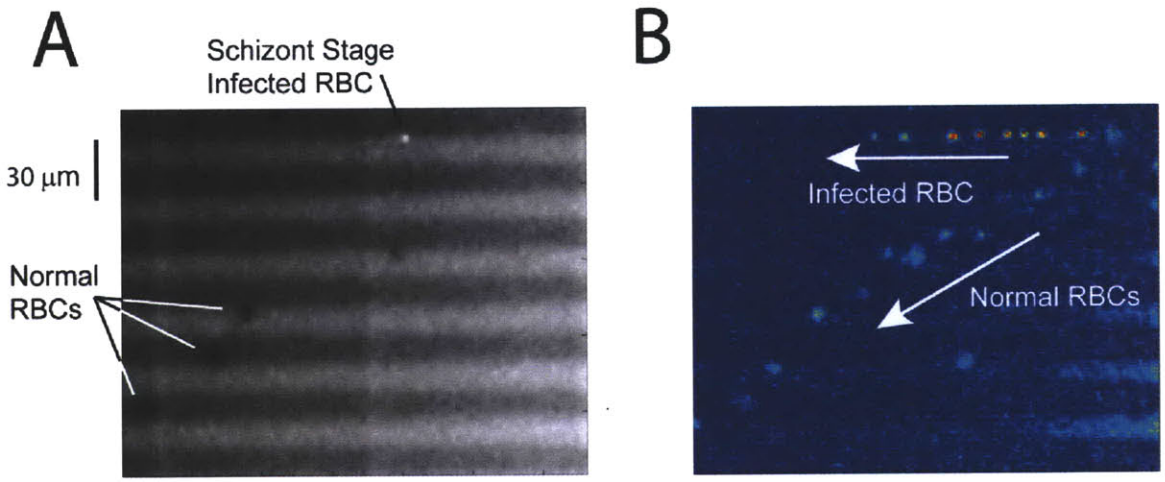

Figure 5.11. A. Still frame from movie. Malaria infected RBCs stained with Hoechst dye fluoresce under UV illumination, while uninfected cells appear as shadows. **B.** Superimposed and merged images of same movie. The infected cell can be seen moving horizontally, while the normal cells move diagonally.

We present quantitative results of separation in Figure 5.12. In this figure, we show that we are able to separate 4-infected cells out of 164 cells.

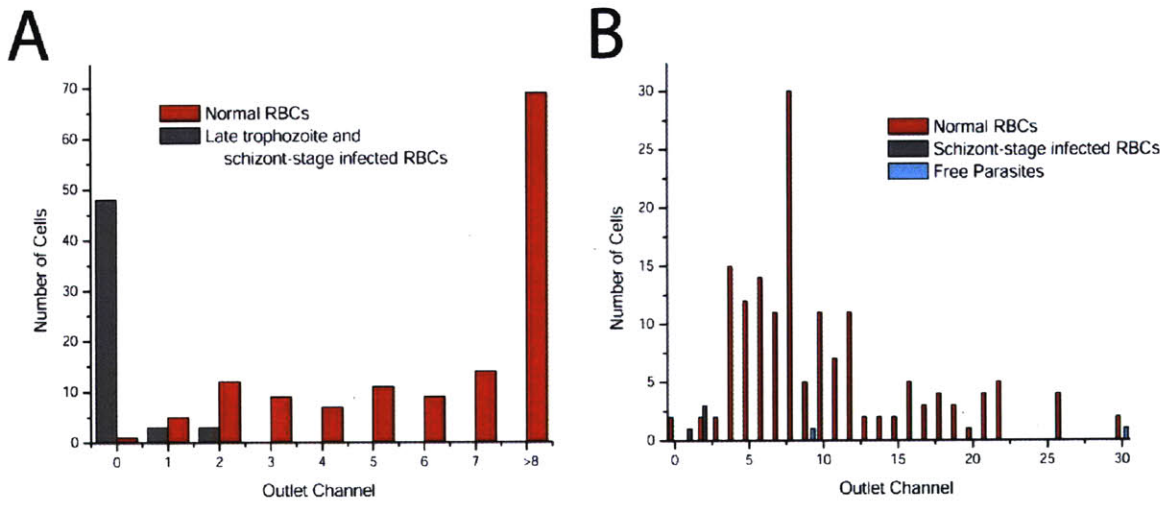

Figure 5.12. A. Histogram showing separation between enriched infected RBCs and normal RBCs. **B.** Demonstration of device selectivity. The device was able to isolate 4 schizont-stage infected RBCs from a population of 164 cells.

Lastly, we separated ring-stage malaria-infected RBCs from uninfected RBCs. We systematically tested slits of various widths, ranging from 2.1 μm to 2.9 μm. Slits too narrow resulted in essentially none of the cells being able to traverse the slit, while slits too wide resulted in nearly all of the cells being able to traverse the slit. We found that a slit width of 2.2 μm worked best for separating ring-stage infected RBCs from uninfected RBCs, Figure 5.13. W e also show a superimposed image a video taken during an experiment using a 2.2 μm shallow region device separating ring-stage malaria-infected RBCs from uninfected RBCs, Figure 5.14.

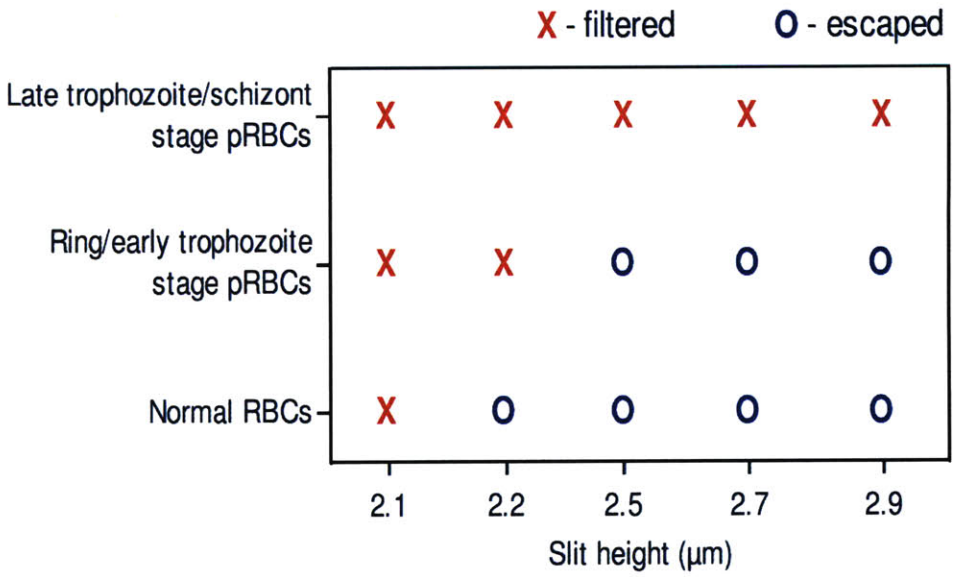

Figure 5.13. Chart showing the filtering ability of devices with various slit heights. Slits too narrow are so restrictive that no cell passes through, while slits too wide are not sensitive and allow nearly every cell to pass through. From (152).

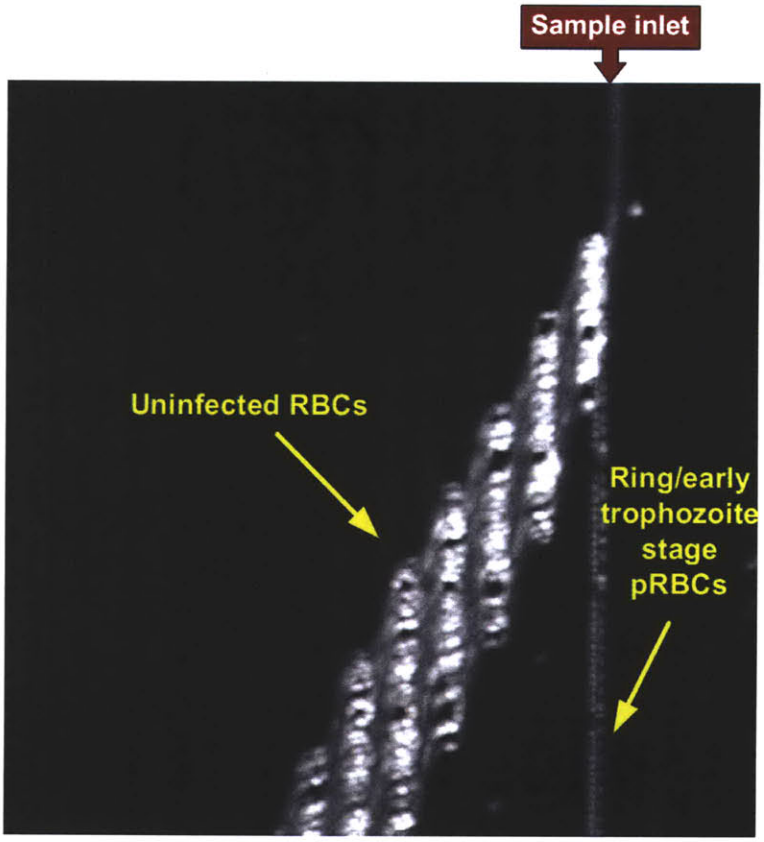

Figure 5.14. Superimposed image of separation between ring-stage malaria-infected and uninfected RBCs in a 2.2 μm shallow-region device. Uninfected RBCs move along the flow direction and the stiffer ring and early trophozoite stage infected RBCs roll along the edge of the slit. From (152).

CONCLUSION

In this chapter, we first demonstrated that RBCs of increased rigidity transit through slits at a lower velocity compared to healthy RBCs. We then showed that when fluid flows at an angle to a slit, more rigid cells will slide along the edge of the slit, while less rigid cells will follow the direction of fluid flow. We then demonstrated the ability of this device to continuously separate schizont stage malaria-infected RBCs from healthy RBCs.

Applications of continuous-flow deformability-based separation include sample preparation for biochemical and cell culture assays. Deformability-based cell sorting could also prove to be useful for situations when cell surface markers are not clearly identified for FACS. Further experimental and modeling work is necessary to optimize the separation resolution and throughput.

Chapter 6

CONCLUSION AND OUTLOOK

THESIS CONTRIBUTIONS

In this thesis, we have made several contributions to the area of dynamic measurements of RBC mechanical properties. In past work, there have been several theoretical and computational models presented that examine the effect of entrance geometry and cell deformability on the ability of a cell to enter a pore (129, 130, 137). However, experimental testing of these theories has not been accomplished. We presented an innovative approach to examining these effects experimentally.

In the area of microfluidic flow cytometry, it is rare for studies to measure the properties of thousands of cells with ease. In our work, we have developed a computer program that is able to extract

dynamic deformability measurements from experimental video, achieving high throughput and statistically significant results.

Three factors contribute to RBC deformability: membrane properties, surface area-to-volume ratio, and cytosolic viscosity. In many studies of RBC deformability, it is not clear which of these properties is the causative factor of experimental measurements. In our work, we have conducted a dissipative particle dynamics-based parametric study of the influence of each of these factors on the measured experimental observations and concluded that membrane shear modulus is the main factor responsible. Based on this conclusion, we are able to extract quantitative data regarding this parameter from our experiments.

Lastly, we have presented a continuous-flow deformability-based separation device. In contrast to past microfabricated cell-separation devices, in our study we focus specifically on deformability and eliminate other confounding factors such as size and cell-to-cell interactions. We demonstrate separation of schizont-stage malaria-infected RBCs from uninfected RBCs and ring-stage malaria-infected RBCs from uninfected RBCs. The design of this device is based on the architecture of the human spleen and minimizes clogging. With further optimization, these systems are expected to increase the detection sensitivity of malaria-infected RBCs by Giemsa-staining-based malaria diagnostics.

Ongoing Work

Past studies have indicated that temperature substantially affects cells' mechanical properties. Most previous studies have been performed at room temperature, as have the results presented in this thesis. We are currently repeating several of our experiments at physiologically relevant temperatures, such as normal body temperature and febrile temperature, which is important in the context of malaria.

These temperature changes have been shown to substantially affect the membrane shear modulus of ring-stage malaria-infected RBCs.

Many chemicals are known to influence the deformability of RBCs. For example, hydroxyurea is known to increase the production of fetal hemoglobin and thus reduce the severity of sickle cell anemia, and pentoxifylline also increases erythrocyte flexibility. One aspect of drug-related effects on RBC deformability is the effect of artemisinin on malaria-infected RBC deformability. In addition to the deformability of these cells, whether mechanical methods are sufficient for pitting of malaria-infected RBCs has also not been explored. Based on scanning electron microscope measurements of the dimensions of the endothelial slits of the spleen, which are normally closed and can be 200 nm to 500 nm wide and 2-3 um long (153), we plan to construct a device mimicking these dimensions. Also, the speed that blood moves through the endothelial slits of the spleen has been measured to be around 7 μm/s (154).

To continue to automate the experiment setup, we are planning to combine the current device with an autosampler, which can automatically inject liquids from various containers into the device at a fixed flow rate. In this way, a large number of well-controlled conditions can be screened without human intervention.

OUTLOOK

High throughput single-cell methods of measuring deformability are generally not available to biology laboratories and health clinics, unlike methods of measuring single-cell biochemical properties, such as FACS, and methods of measuring individual cell size, such as the coulter counter. Although methods exist to measure bulk deformability and are commonly used in biological laboratories, such as the rheoscope and membrane filtration, these methods do not yield precise deformability data. We

believe that if a high-throughput single-cell method of measuring cell deformability were readily available and standardized across laboratories, much more rapid diffusion of advances in cell mechanics would be possible.

A natural extension for our approach to studying cell deformability is to extend the approach to other cell types, in addition to cells in blood. A natural application of the device would be in the area of cancer research, where recent results have indicated that cancer cells are more deformable compared to normal cells (13). However, the heterogeneity in terms of size in these populations may be an obstacle to this goal.

For our deformability cytometer, we made the assumption that the cell size distribution would be relatively uniform, since cells that circulate in blood must be able to transit through the reticuloendothelial system of the spleen, which restricts cells in terms of size and deformability. Then measurements of cell deformability would not be confounded by differences in size or shape of the cells.

When we extend this approach to solid-organ cancer cells, the assumption of homogeneous size is not necessarily true. In populations of solid-organ cells that are grown in culture or come from biopsy samples, it is not uncommon to find cells in that population that are 1 to 2 orders of magnitude different in linear size. Perhaps by separating these cells based on size first, it may be possible to apply our approach to study their deformability.

Among the many benefits of microfluidics is the ability to study phenomena that take place on the order of seconds. In a study of neutrophils forced into microfluidic channels representative of lung capillaries, these neutrophils were observed to extend pseudopods on a timescale of 10-100s (155). Also in this study, a reduction in shear moduli was observed within seconds of neutrophil deformation and a recovery of shear moduli was observed within about a minute (156). Other dynamic mechanical

phenomena that may be explored in a microfluidic context include tissue leukocyte extravasation after p and l selectin-mediated cell rolling. During this extravasation process, chemoattractants prompt the leukocyte to create gaps between endothelial cells and exit the circulation. Currently, these studies are studied using the Boyden assay, but microfluidic devices may be able to provide more control over the liquid environment and generate more precise mechanical constraints.

Lastly, we note that many microfluidic studies of cellular deformability focus on the effect of various factors on the mechanical properties of the cells. For example, Rosenbluth et al. examined the effect of fMLP (an inflammatory mediator that stiffens WBCs), leukostasis, and drugs on neutrophil deformability (157); our study examines the effect of the RESA protein on deformability by knocking it out; and Brody et al. inferred the role of ATP on RBC deformability with the use of fluorescent dyes (7). Conversely, one could look at how what a cell experiences mechanically affects which genes are expressed, differentiation, or other mechanical properties. There are many experiments examining the effect mechanical perturbations have on cultured cells. Examples include how fluid shear stress induces haematopoietic cell differentiation (158) and how matrix stiffness affects mesenchymal stem cell differentiation (159). For non-cultured cells, studies have examined how WBCs respond to deformation by extendeding pseudopods (155) and respond to fluid shear by recoiling and stiffening (160). However there has been little study of signaling or altered gene expression after mechanical perturbation. We believe this area that may be worth exploring using available microfluidic tools.

BIBLIOGRAPHY

1. Mokken FC, Kedaria M, Henny CP, Hardeman M, & Gleb A (1992) The clinical importance of erythrocyte deformability, a hemorrheological parameter. *Ann. Hematol.,* **64,** 113-122.
2. Ingram V (1957) Gene Mutations in Human Hæmoglobin: the Chemical Difference Between Normal and Sickle Cell Hæmoglobin. *Nature,* **180,** 326-328.
3. Eber S, *et al.* (1996) Ankyrin−1 mutations are a major cause of dominant and recessive hereditary spherocytosis. *Nature Genetics,* **13,** 214-218.
4. Angekort B, Maurin N, & Boateng K (1979) Influence of pentoxifylline on erythrocyte deformability in peripheral occlusive arterial disease. *Current Medical Research and Opinion,* **6,** 255-258.
5. McMillan D, Utterback N, & La Puma J (1978) Reduced erythrocyte deformability in diabetes. *Diabetes,* **27,** 895-901.
6. Cranston H, *et al.* (1983) Plasmodium falciparum maturation abolishes physiologic red cell deformability. *Science,* **233,** 400-403.
7. Brody JP, Han Y, Austin RH, & Bitensky M (1995) Deformation and flow of red blood cells in a synthetic lattice: evidence for an active cytoskeleton. *Biophysical Journal,* **68,** 2224-2232.
8. Mao P & Han J (2005) Fabrication and characterization of 20 nm planar nanofluidic channels by glass–glass and glass–silicon bonding. *Lab Chip,* **5,** 837-844.
9. Lim CT (2006) Single cell mechanics study of the human disease malaria. *Journal of Biomechanical Science and Engineering,* **1**.
10. Evans E, Mohandas N, & Leung A (1983) Static and dynamic rigidities of normal and sickle erythrocytes: Major influence of cell hemoglobin concentration. *J. Clin. Invest,* **73,** 477-488.
11. Rosenbluth MJ, Lam WA, & Fletcher DA (2006) Force microscopy of nonadherent cells: a comparison of leukemia cell deformability. *Biophysical Journal,* **90,** 2994-3003.
12. Lam WA, Rosenbluth MJ, & Fletcher DA (2007) Chemotherapy exposure increases leukemia cell stiffness. *Blood,* **109,** 3505-3508.
13. Cross SE, Jin Y-S, Rao J, & Simzewski JK (2007) Nanomechanical analysis of cells from cancer patients. *Nature Nanotechnology*.
14. Kumar V, Abbas AK, & Fausto N (2004) *Robbins and Cotran Pathologic Basis of Disease* (Saunders).
15. Worthen GS, Schwab B, Elson E, & Downey GP (1989) Mechanics of stimulated neutrophils: cell stiffening induces retention in capillaries. *Science,* **245,** 183-186.
16. Young B, Lowe JS, Stevens A, & Heath JW (2006) *Wheater's Functional Histology* (Elsevier).
17. Myerowitz RL, Edwards PA, & Sartiano GP (1977) Carcinocythemia (carcinoma cell leukemia) due to metastatic carcinoma of the breast. *Cancer,* **40,** 3107-3111.

18. Seronie-Vivien S, *et al.* (2001) Carcinocythemia as the single extension of breast cancer: report of a case and review of the literature. *Annals of Oncology,* **12,** 1019-1022.
19. Kumar V, Abbas A, & Fausto N (2004) *Robbins and Cotran Pathologic Basis of Disease* (Saunders).
20. Cristofanilli M, *et al.* (2004) Circulating tumor cells, disease progression, and survival in metastatic breast cancer. *The New England Journal of Medicine,* **315,** 781-791.
21. Gaforio J-J, *et al.* (2003) Detection of breast cancer cells in the peripheral blood is positively correlated with estrogen-receptor status and predicts for poor diagnosis. *Int. J. Cancer,* **107,** 984-990.
22. Gross H-J, Verwer B, Houck D, Hoffman R, & Recktenwald D (1995) Model study detecting breast cancer cells in peripheral blood mononuclear cells at frequencies as low as 10^-7. *Proc. Natl. Acad. Sci.,* **92,** 537-541.
23. Racila E, *et al.* (1998) Detection and characterization of carcinoma cells in the blood. *Proc. Natl. Acad. Sci.,* **95,** 4589-4594.
24. Nagrath S, *et al.* (2007) Isolation of rare circulating tumor cells in cancer patients by microchip technology. *Nature,* **450,** 1235-1239.
25. Carey RW, Taft PD, Bennett JM, & Kaufman S (1975) Carcinocythemia (carcinoma cell leukemia) an acute leukemia-like picture due to metastatic carcinoma cells.
26. Gallivan MVE & Lokich JJ (1984) Carcinocythemia (carcinoma cell leukemia). *Cancer Research,* **53,** 1100-1102.
27. Fung Y (1993) *Biomechanics: mechanical properties of living tissues* (Springer).
28. Mohandas N, Clark MR, Jacobs MS, & Shohet SB (1980) Analysis of factors regulating erythrocyte deformability. *J. Clin. Invest,* **66,** 563-573.
29. Connor J, Pak C, & Schroit A (1994) Exposure of phosphatidylserine in the outer leaflet of human red blood cells. *Journal of Biological Chemistry,* **269,** 2399-2404.
30. Krafts K (University of Minnesota School of Medicine).
31. Snow R, Guerra C, Noor A, Myint H, & Hay S (2005) The global distribution of clinical episodes of Plasmodium falciparum malaria. *Nature,* **434,** 214-217.
32. Webb J (2009) *Humanity's Burden: A Global History of Malaria* (Cambridge University Press).
33. Maier A, Cooke B, Cowman A, & Tilley L (2009) Malaria parasite proteins that remodel the host erythrocyte. *Nature Reviews Microbiology,* **7,** 341-354.
34. Miller L, Baruch D, Marsh K, & Doumbo O (2002) The pathogenic basis of malaria. *Nature,* **415,** 673-679.
35. Chotivanich K, *et al.* (2000) The mechanisms of parasite clearance after antimalarial treatment of Plasmodium falciparum malaria. *Journal of Infectious Diseases,* **182,** 629-633.
36. Angus B, Chotivanich K, Udomsangpetch R, & White N (1997) In Vivo Removal of Malaria Parasites From Red Blood Cells Without Their Destruction in Acute Falciparum Malaria *Blood,* **90,** 2037-2040.
37. Schnitzer B, Sodeman T, Mead M, & Contacos P (1973) An ultrastructural study of the red pulp of the spleen in malaria. *Blood,* **41,** 207-217.

38. Newton P, *et al.* (2001) A comparison of the in vivo kinetics of Plasmodium falciparum ring-infected erythrocyte surface antigen-positive and -negative erythrocytes. *Blood,* **98,** 450-457.
39. Anoyona S, Schrier S, Gichuki C, & Waitumbi J (2006) Pitting of malaria parasites and spherocyte formation. *Malaria Journal,* **5**.
40. Schnitzer B, Sodeman T, Mead M, & Contacos P (1972) Pitting function of the spleen in malaria: ultrastructural observations. *Science,* **177,** 175-177.
41. Ibrahim S & van den Engh G (2003) High-speed cell sorting: fundamentals and recent advances. *Current Opinion,* **14,** 5-12.
42. Fu AY, Spence C, Scherer A, Arnold FH, & Quake SR (1999) A microfabricated fluorescence-activated cell sorter. *Nature Biotechnology,* **17,** 1109-1111.
43. Ashcoroft RG & Lopez PA (2000) Commercial high speed machines open new opportunities in high throughput flow cytometry. *Journal of Immunological Methods,* **243,** 13-24.
44. Krivacic RT, *et al.* (2004) A rare-cell detector for cancer. *Proc. Natl. Acad. Sci.,* **101,** 10501-10504.
45. Shah J (2007) *HST.505: Laboratory in Molecular & Celluar Sciences*.
46. Wang MM, *et al.* (2005) Microfluidic sorting of mammalian cells by optical force switching. *Nature Biotechnology,* **23,** 83-87.
47. Chen C, *et al.* (2003) Design and operation of a microfluidic sorter for Drosophila embryos. *Sensors and Acuators B,* **102,** 59-66.
48. Kruger J, *et al.* (2002) Development of a microfluidic device for flurescence activated cell sorting. *J. Micromech. Microeng.,* **12,** 486-494.
49. Voldman J, Gray ML, Toner M, & Schmidt MA (2002) A microfabrication-based dynamic array cytometer. *Analytical Chemistry,* **74,** 3984-3990.
50. Chiou PY, Ohta AT, & Wu MC (2005) Massively parallel manipulation of single cells and microparticles using optical images. *Nature,* **436,** 370-372.
51. Thiel A, Scheffold A, & Radbruch A (1998) Immunomagnetic cell sorting - pushing the limits. *Immunotechnology,* **4,** 89-96.
52. Berger M, Castelino J, Huang R, Shah M, & Austin RH (2001) Design of a microfabricated magnetic cell separator. *Electrophoresis,* **22,** 3883-3892.
53. Zborowski M, Sun L, Moore LR, Williams PS, & Chalmers JJ (1999) Continuous cell separation using novel magnetic quadrupole flow sorter. *Journal of Magnetism and Magnetic Materials,* **194,** 224-230.
54. Inglis DW, Riehn R, Austin RH, & Sturm JC (2004) Continuous microfluidic immunomagnetic cell separation. *Applied Physics Letters,* **85,** 5093-5095.
55. Hu X, *et al.* (2005) Marker-specific sorting of rare cells using dielectrophoresis. *Proc. Natl. Acad. Sci.,* **104,** 15757-15761.
56. Miltenyi S, Muller W, Weichel W, & Radbruch A (1990) High gradient magnetic cell separation with MACS. *Cytometry,* **11,** 231-238.
57. Furdui VI & Harrison DJ (2004) Immunomagnetic T cell capture from blood for PCR analysis using microfluidic systems. *Lab on a Chip*.

58. Grodzinski P, Yang JM, Liu RH, & Ward MD (2003) A modular microfluidic system for cell pre-concentration and genetic sample preparation. *Biomedical Microdevices,* **5,** 303-310.
59. Lee H, Purdon AM, & Westervelt RM (2004) Manipulation of biological cells using a microelectromagnet matrix. *Applied Physics Letters,* **85,** 1063-1065.
60. Nalayanda DD, Mahendran K, & Schmidtke DW (2007) Micropatterned surfaces for controlling cell adhesion and rolling under flow. *Biomedical Microdevices,* **9,** 207-214.
61. Karnik R, *et al.* (2008) Nanochemanical control of cell rolling in two dimensions through surface patterning of receptors. *Nano Letters.*
62. Chang W, Lee LP, & Liepmann D (2005) Biomimetic technique for adhesion-based collection and separation of cells in a microfulidic channel. *Lab on a Chip,* **5,** 64-73.
63. Murthy SK, Sin A, Tompkins RG, & Toner M (2004) Effect of flow and surface conditions on human lymphocyte isolation using microfluidic chambers. *Langmuir,* **20,** 11649-11655.
64. Kwon KW, *et al.* (2007) Label-free, microfluidic separation and enrichment of human breast cancer cells by adhesion difference. *Lab on a Chip,* **7,** 1461-1468.
65. Cheng J, *et al.* (1998) Preparation and hybridization analysis of DNA/RNA from E. coli on microfabricated bioelectronic chips. *Nature Biotechnology,* **16,** 541-546.
66. Huang Y, *et al.* (2002) Dielectrophoretic cell separation and gene expression profiling on microelectronic chip arrays. *Analytical Chemistry,* **74,** 3362-3371.
67. Cheng J, Sheldon EL, Wu MC, Heller MJ, & O'Connell J (1998) Isolation of cultured cervical carcinoma cells mixed with peripheral blood cells on a bioelectronic chip. *Analytical Chemistry,* **70,** 2321-2326.
68. Becker FF, *et al.* (1995) Separation of human breast cancer cells from blood by differential dielectric affinity. *Proc. Natl. Acad. Sci.,* **92,** 860-864.
69. MacDonald M, Spalding G, & Dholakia K (2003) Microfluidic sorting in an optical lattice. *Nature* **426,** 401-404.
70. Han K-H & Frazier AB (2004) Continuous magnetophoretic separation of blood cells in microdevice format. *Journal of Applied Physics,* **96,** 5797-5802.
71. Noble PB & H. CJ (1967) Separation of blood leukocytes by ficoll gradient. *Can. Vet. Jour.,* **8,** 110-111.
72. Moorthy J & Beebe DJ (2003) In situ fabricated porous filters for microsystems. *Lab on a Chip,* **3,** 62-66.
73. Li C-W, Cheung CN, Yang J, Tzang CH, & Yang M (2003) PDMS-based microfluidic device with multi-height structures fabricated by single-step photolithography using printed circuit board as masters. *The Analyst,* **128,** 1137-1142.
74. Gifford SC, *et al.* (2003) Parallel microchannel-based measurements of individual erythrocyte areas and volumes. *Biophysical Journal,* **84,** 623-633.
75. Zhu L, *et al.* (2004) Filter-based microfluidic device as a platform for immunofluirescent assay of microbial cells. *Lab on a Chip,* **4,** 337-341.
76. Chen Z, *et al.* (2005) Theoretical and experimental studies on filtering tumor cells from blood cell mixtures with dam structure in microfluidic devices. *Proceedings of the 2005 IEEE EMBS 27th annual conference,* **27,** 7497-7500.

77. Yang M, Li C-W, & Yang J (2002) Cell docking and on-chip monitoring of cellular reactions with a controlled concentration gradient on a microfluidic device. *Analytical Chemistry,* **74,** 3991-4001.
78. Hawkes J, J, Barber RW, Emerson DR, & Coakley WT (2004) Continuous cell washing and mixing driven by an ultrasound standing wave within a microfluidic channel. *Lab on a Chip*.
79. Crowley TA & Pizziconi V (2005) Isolation of plasma from whole blood using planar microfilters for lab-on-a-chip applications. *Lab on a Chip,* **5,** 922-929.
80. Davis JA, *et al.* (2006) Deterministic hydrodynamics: taking blood apart. *Proc. Natl. Acad. Sci.,* **103,** 14779-14784.
81. Sleep J, Wilson D, Simmons R, & Gratzer W (1999) Elasticity of the red cell membrane and its relation to hemolytic disorders: an optical tweezers study. *Biophysical Journal,* **77,** 3085-3095.
82. Mills JP, *et al.* (2007) Effect of plasmodial RESA protein on deformability of human red blood cells harboring Plasmodium falciparum. *PNAS,* **104,** 9213-9217.
83. Lekka M, *et al.* (1999) Elasticity of normal and cancerous human bladder cells studied by scanning force microscopy. *European Biophysics Journal,* **28,** 312-316.
84. Chronis N & Lee LP (2005) Electrothermally activated SU-8 microgripper for single cell manipulation in solution. *Journal of Microelectromechanical Systems,* **14,** 857-863.
85. Lincoln B, *et al.* (2004) Deformability-based flow cytometry. *Cytometry Part A,* **59A,** 203-209.
86. Guck J, *et al.* (2005) Optical deformability as an inherent cell marker for testing malignant transformation and metastatic competence. *Biophysical Journal,* **88,** 3689-3698.
87. Lincoln B, *et al.* (2007) Reconfigurable microfluidic integration of a dual-beam laser trap with biomedical applications. *Biomedical Microdevices,* **9,** 703-710.
88. Evans E (1973) New membrane concept applied to the analysis of fluid shear- and micropipette-deformed red blood cells. *Biophysical Journal,* **13,** 941-954.
89. Rand RP & Burton AC (1964) Mechanical properties of the red cell membrane. *Biophysical Journal,* **4,** 115-135.
90. Hochmuth RM (1999) Micropipette aspiration of living cells. *Journal of Biomechanics,* **33,** 15-22.
91. Zahalak G, McConnaughey W, & Elson E (1990) Determination of cellular mechanical properties by cell poking, with an application to leukocytes. *J Biomech Eng.,* **112,** 293-294.
92. Ward K, Li W, Zimmer S, & Davis T (1991) Viscoelastic properties of transformed cells: role in tumor cell progression and metastasis formation. *Biorheology,* **28,** 301-313.
93. Weed RI, LaCelle PL, & Merrill W (1969) Metabolic dependence of red cell deformability. *The Journal of Clinical Investigation,* **48,** 795-809.
94. Hochmuth R (2000) Micropipette aspiration of living cells. *Journal of Biomechanics,* **33,** 15-22.

95. Shelby JP, White J, Ganesan K, Rathod PK, & Chiu DT (2003) A microfluidic model for single-cell capillary obstruction by plasmodium falciparum-infected erythrocytes. *PNAS,* **100,** 14618-14622.
96. Abkarian M, Faivre M, & Stone H (2006) High-speed microfluidic differential manometer for cellular-scale hydrodynamics. *PNAS,* **103,** 538-542.
97. Tracey MC, Greenaway RS, Das A, Kaye PH, & Barnes AJ (1995) A silicon micromachined device for use in blood cell deformability studies. *IEEE Transactions on Biomedical Engineering,* **42,** 751-761.
98. Sutton N, Tracey MC, Johnston ID, Greenaway RS, & Rampling MW (1997) A novel instrument for studying the flow behavior of erythrocytes through microchannels simulating human blood capillaries. *Microvascular Research,* **53,** 272-281.
99. Tracey M, Sutton N, Johnston I, & Doetzel W (2000) A microfluidics-based instrument for cytomechanical studies of blood. *1st annual international IEEE-EMBS special topic conference on microtechnologies in medicine and biology.*
100. Abkarian M, Faivre M, Viallat A, & Stone HA Red blood cell dynamics, deformation and rheology via microfluidic experiments.
101. Carlson RH, Gabel CV, Chan SS, & Austin RH (1997) Self-sorting of white blood cells in a lattice. *Phys Rev Lett,* **79,** 2149-2152.
102. Mohamed H, *et al.* (2004) Development of a rare cell fractionation device: application for cancer detection. *IEEE Transactions on Nanobioscience,* **3,** 251-256.
103. Mohamed H, Turner JN, & Caggana M (2007) Biochip for separating fetal cells from maternal circulation. *Journal of Chromatography A,* **1162,** 187-192.
104. Huang L, *et al.* (2001) Generation of Large-area Tunable Uniform Electric Fields in Microfluidic Arrays for Rapid DNA Separation *Technical Digest of International Electron Devices Meeting,* 363-366.
105. Gervais T, El-Ali J, Gunther A, & Jensen KF (2006) Flow-induced deformation of shallow microfluidic channels. *Lab Chip,* **6,** 500-507.
106. Harrison C, Cabral J, Stafford CM, Karim A, & Amis EJ (2004) A rapid prototyping technique for the fabrication of solvent-resistant structures. *J Micromech Microeng,* **14,** 153-158.
107. Abgrall P, *et al.* (2006) A novel fabrication method of flexible and monolithic 3D microfluidic structures using lamination of SU-8 films. *J Micromech Microeng,* **16,** 113-121.
108. Kim SH, *et al.* (2007) Simple route to hydrophilic microfluidic chip fabrication using an ultraviolet (UV)-cured polymer. *Advanced Functional Materials,* **17,** 3493-3498.
109. Deitsch K, Driskill C, & Wellems T (2001) Transformation of malaria parasites by the spontaneous uptake and expression of DNA from human erythrocytes. *Nucleic Acids Res.* , **29,** 850-853.
110. Groot RD & Warren PB (1997) Dissipative particle dynamics: Bridging the gap between atomistic and mesoscopic simulation. *J Chem Phys,* **107,** 4423-4435.
111. Fan XJ, Phan-Thien N, Chen S, Wu XH, & Ng TY (2006) Simulating flow of DNA suspension using dissipative particle dynamics. *Phys Fluids,* **18,** 063102.

112. Pivkin IV & Karniadakis GE (2005) A new method to impose no-slip boundary conditions in dissipative particle dynamics. *Journal of Computational Physics,* **207,** 114-128.
113. Pivkin IV & Karniadakis GE (2008) Accurate coarse-grained modeling of red blood cells. *Phys Rev Lett,* **101,** 118105.
114. Discher DE, Boal DH, & Boey SK (1998) Simulations of the erythrocyte cytoskeleton at large deformation. II. Micropipette aspiration. *Biophysical Journal,* **75,** 1584-1597.
115. Li J, Dao M, Lim CT, & Suresh S (2005) Spectrin-level modeling of the cytoskeleton and optical tweezers stretching of the erythrocyte. *Biophysical Journal,* **88,** 3707-3719.
116. Park Y, *et al.* (2008) Refractive index maps and membrane dynamics of human red blood cells parasitized by Plasmodium falciparum. *PNAS,* **105,** 13730-13735.
117. WHO (2008) *World Malaria Report 2008*.
118. Suresh S, *et al.* (2005) Connections between single-cell biomechanics and human disease states: gastrointestinal cancer and malaria. *Acta Biomaterialia,* **1,** 16-30.
119. Safeukui I, *et al.* (2008) Retention of Plasmodium falciparum ring-infected erythrocytes in the slow, open microcirculation of the human spleen. *Blood,* **112,** 2520-2528.
120. van der Heyde J, Nolan J, Combes V, Gramaglia I, & Grau G (2006) A unified hypothesis for the genesis of cerebral malaria: sequestration, inflammation and hemostasis leading to microcirculatory dysfunction. *Trends in Parasitology,* **22,** 503-508.
121. Reid J, Barnes A, Lock P, Dormandy J, & Dormandy T (1976) A simple method for measuring erythrocyte deformability. *J. Clin. Pharmacol.,* **29,** 855-858.
122. Bessis M & Mohandas N (1977) A diffractometric method for the measurement of cellular deformability. *Blood Cells,* **1,** 307-313.
123. Nash G, O'Brien O, Gordon-Smith E, & Dormandy J (1989) Abnormalities in the mechanical properties of red blood cells caused by plasmodium falciparum. *Blood,* **74,** 855-861.
124. Chien S (1977) Principles and techniques for assessing erythrocyte deformability. *Blood Cells,* **3,** 71-99.
125. Lekka M, Fornal M, Pyka-Fosciak G, Lebed K, & Wizner B (2005) Erythrocyte stiffness probed using atomic force microscopy. *Biorheology,* **42,** 307-317.
126. Guck J, *et al.* (2001) The optical stretcher: a novel laser tool to micromanipulate cells. *Biophysical Journal,* **81,** 767-784.
127. Deen W (1998) *Analysis of Transport Phenomena* (Oxford University Press, New York).
128. Chien S (1987) Red cell deformability and its relevance to blood flow. *Ann. Rev. Physiol.* , **49,** 177-192.
129. Bathe M, Shirai A, Doerschuk C, & Kamm R (2002) Neutrophil transit times through pulmonary capillaries: the effects of capillary geometry and fMLP-stimulation. *Biophysical Journal,* **83,** 1917-1933.
130. Shirai A, Fujita R, & Hayase T (2002) Transit characteristics of a neutrophil passing through a circular constriction in a cylindrical capillary vessel (effect of mechanical properties of the cell and constriction geometry). *JSME International Journal,* **45,** 974-980.

131. Tong X & Caldwell KD (1995) Separation and characterization of red blood cells with different membrane deformability using steric field-flow fractionation. *Journal of Chromatography B,* **674,** 39-47.
132. Leblond P, LaCelle P, & Weed R (1971) Cellular deformability: a possible determinant of the normal release of maturing erythrocytes from the bone marrow. *Blood,* **37,** 40-46.
133. Gifford S, Derganc J, Shevkoplyas S, Yoshida T, & Bitensky M (2006) A detailed study of time-dependent changes in human red blood cells: from reticulocyte maturation to erythrocyte senescence. *British Journal of Haematology,* **135,** 395-404.
134. Waugh R (1991) Reticulocyte rigidity and passage through endothelial-like pores. *Blood,* **78,** 3037-3042.
135. Xie L, *et al.* (2006) Studies on the biomechanical properties of maturing reticulocytes. *Journal of Biomechanics,* **39,** 530-535.
136. Enderle T, *et al.* (1997) Membrane specific mapping and colocalization of malarial and host skeletal proteins in the Plasmodium falciparum infected erythrocyte by dual-color near-field scanning optical microscopy *PNAS,* **94,** 520-525.
137. Secomb T & Hsu R (1996) Analysis of red blood cell motion through cylindrical micropores: Effects of cell properties. *Biophysical Journal,* **71,** 1095-1101.
138. Hochmuth R, Worthy P, & Evans E (1979) Red cell extensional recovery and the determination of membrane viscosity. *Biophysical Journal,* **26,** 101-114.
139. Shirai A, Fujita R, & Hayase T (2003) Transit characteristics of a neutrophil passing through two moderate constrictions in a cylindrical capillary vessel (Effect of cell deformation on transit through the second constriction). *JSME International Journal,* **46,** 1198-1207.
140. Groisman A, Enzelberger M, & Quake S (2003) Microfluidic memory and control devices. *Science,* **300,** 955-958.
141. Higgins J, Eddington D, Bhatia S, & Mahadevan L (2007) Sickle cell vasoocclusion and rescue in a microfluidic device. *PNAS,* **104,** 20496-20500.
142. Kim S, Ko S, Kang K, & Han J (2010) Direct seawater desalination by ion concentration polarization. *Nature Nanotechnology,* **5,** 297-301.
143. Fu J, Schoch R, Stevens A, Tannenbaum S, & Han J (2007) A patterned anisotropic nanofluidic sieving structure for continuous-flow separation of DNA and proteins. *Nature Nanotechnology,* **2,** 121-128.
144. Huang L, Cox E, Austin R, & Strum J (2004) Continuous particle displacement through deterministic lateral displacement. *Science,* **304,** 987-990.
145. Takagi J, Yamada M, Yasuda M, & Seki M (2005) Continuous particle separation in a microchannel having asymmetrically arranged multiple branches. *Lab on a Chip,* **5,** 778-784.
146. Drenckhahn D & Wagner J (1986) Stress fibers in the splenic sinus endothelium in situ: molecular structure, relationship to the extracellular matrix, and contractility. *Journal of Cell Biology,* **102,** 1738-1747.
147. Uehara K & Uehara A (2008) Localization of claudin-5 and ZO-1 in rat spleen sinus endothelial cells. *Hostochemistry and Cell Biology,* **129,** 95-103.

148. VanDelinder V & Groisman A (2007) Perfusion in microfluidic cross-flow: separation of white blood cells from whole blood and exchange of medium in a continuous flow. *Anal. Chem.*, **79,** 2023-2030.
149. Stroock A, *et al.* (2002) Chaotic mixer for microchannels. *Science,* **25,** 647-651.
150. Choi S, Song S, Choi C, & Park J (2007) Continuous blood cell separation by hydrophoretic filtration. *Lab on a Chip,* **7,** 1532-1538.
151. Choi S, Song S, Choi C, & Park J (2008) Sheathless focusing of microbeads and blood cells based on hydrophoresis. *Small,* **4,** 634-641.
152. Bow H, *et al.* (2009) Continuous-flow deformability-based sorting of malaria-infected red blood cells. *Proceedings of microTAS,* 1219-1221.
153. Chen L & Weiss L (1973) The role of the sinus wall in the passage of erythrocytes through the spleen. *Blood,* **41,** 529-237.
154. Moghimi S (1995) Mechanisms of splenic clearance of blood cells and particles: towards development of new splenotropic agents. *Advanced Drug Delivery Reviews,* **17,** 103-115.
155. Yap B & Kamm R (2005) Mechanical deformation of neutrophils into narrow channels induces pseudopod projection and changes in biomechanical properties. *J. Appl. Physiol.,* **98,** 1930-1939.
156. Yap B & Kamm R (2005) Cytoskeletal remodeling and cellular activation during deformation of neutrophils into narrow channels. *J. Appl. Physiol.,* **99,** 2323-2330.
157. Rosenbluth M, Lam W, & Fletcher D (2008) Analyzing cell mechanics in hematologic diseases with microfluidic biophysical flow cytometry. *Lab on a Chip,* **8,** 1062-1070.
158. Adamo L, *et al.* (2009) Biomechanical forces promote embryonic haematopoiesis. *Nature,* **459,** 1131-1135.
159. Engler A, Sen S, Sweeney H, & Discher D (2006) Matrix elasticity directs stem cell lineage specification. *Cell,* **126,** 677-689.
160. Coughlin M, Sohn D, & Schmid-Schonbein G (2008) Recoil and stiffening by adherent leukocytes in response to fluid shear. *Biophysical Journal,* **94,** 1046-1051.